UNIVERSITY OF OTTAWA

DOCTOR OF PHILOSOPHY THESIS

InGaAsP-on-Insulator Photonic Platforms: Process Development, Nonlinear Losses, and Frequency Comb Modeling

Author:
Athulya THULASEEDHARAN

Supervisor:
Prof. Ksenia DOLGALEVA

A thesis submitted in partial fulfillment of the requirements for the Doctorate of Philosophy in Physics

Department of Physics
Faculty of Science
University of Ottawa

© Athulya Thulaseedharan, Ottawa, Canada, 2026

Declaration of Authorship

I, Athulya THULASEEDHARAN, declare that this thesis, titled "InGaAsP-on-Insulator Photonic Platforms: Process Development, Nonlinear Losses, and Frequency Comb Modeling", and the work presented in it are my own. I confirm that except where specific reference is made to the work of others, the contents of this dissertation are original and have not been submitted in whole or in part for consideration for any other degree or qualification in this, or any other university. This dissertation is my own work and contains nothing which is the outcome of work done in collaboration with others, except as specified in the text and Acknowledgements.

Athulya Thulaseedharan
July, 2026
Ottawa, Canada

Abstract

Nonlinear integrated photonics has emerged as a key technology for advanced optical communication systems, enabling functionalities such as all-optical signal processing, wavelength conversion, and frequency-comb generation. These capabilities depend on suitable material platforms that can support strong optical nonlinearity and efficient integration. Among the available material platforms, Indium Gallium Arsenide Phosphide (InGaAsP) offers a compelling combination of strong optical nonlinearity, high-speed optical response, and operation across the telecommunications wavelength bands. Furthermore, its ability to support both active and passive photonic functionalities makes it particularly suitable for monolithic photonic integration. However, optical performance in conventional C-band InGaAsP/InP structures remains inherently limited by nonlinear losses, dominated by two-photon absorption (TPA) and subsequent free-carrier effects (FCE).

To understand the impact of TPA and FCE-related losses in InGaAsP-based devices, in the first thesis project, we perform the lifetime measurement of TPA-generated free carriers prior to recombination. Pump–probe measurements conducted on fabricated InGaAsP/InP waveguides yielded free-carrier lifetimes of 0.24 ns and 0.46 ns upon exciting the fundamental TE and TM polarization of the waveguide, serving as a vital reference for future FC lifetime engineering.

Building on the obtained knowledge, the next thesis project investigates a novel InGaAsP-on-insulator (InGaAsP-OI) platform for nonlinear integrated photonics, focusing on its application to optical frequency-comb generation. We performed the first comprehensive theoretical analysis of InGaAsP-OI ring resonators while considering realistic nonlinear loss mechanisms—specifically TPA and FCE at the 1550 nm telecom C-band wavelength. Additionally, various strategies for tuning the free-carrier lifetime are evaluated alongside their

impact on resonator performance.

We next undertake steps towards III-V semiconductors-on-insulator photonic integration platform development. In particular, we explore two material systems, including InGaAsP-OI and aluminum gallium arsenide (AlGaAs)-OI, developing the steps for their fabrication. The next thesis project describes our effort in wafer bonding of a III-V semiconductor layer to SiO_2-on-silicon wafer and the consecutive III-V substrate-removal processes, outlining key technical challenges and experimental process development results.

Lastly, as a separate project, we developed a proximity-effect correction (PEC) scheme for artificial 2D nanostructures, termed metasurfaces. By relying on shape modification of individual structural elements of the metasurfaces and the electron-beam lithography parameter tuning, we achieved precise agreement between the target design and fabricated feature shapes and dimensions with a negligible measured resonance drift. The developed proximity effect correction method is applicable in university cleanroom facilities hosting low-voltage (low-kV) electron-beam lithography systems constrained by computational capacity.

Acknowledgement

First and foremost, I would like to express my sincere gratitude to my supervisor, Prof. Ksenia Dolgaleva, for giving me the opportunity to pursue my PhD under her guidance and supervision. I am deeply thankful for her invaluable technical discussions, constant encouragement, and collaborative spirit. The funding opportunities she identified and supported were indispensable in advancing my research and played a crucial role in making this work possible.

I would also like to thank Dr. Lais Fujii dos Santos, one of our outstanding postdoctoral researchers, for her supervision in the design and fabrication aspects of this work. I am truly grateful for her willingness to offer continual support through extensive training and insightful technical discussions. Her unwavering support during device fabrication—especially during periods when fabrication felt overwhelming and seemingly endless—was invaluable. She has been a remarkable mentor and source of inspiration, and her attentiveness and depth of engagement in discussions were among the greatest encouragements I received throughout this research. I gratefully acknowledge funding from the Natural Sciences and Engineering Research Council of Canada (NSERC) CREATE TrUST program, which enabled me to connect with photonics researchers and industries across Canada. I also thank the Faculty of Engineering at the University of Ottawa for the International Experience Bursary, which allowed me to represent uOttawa at the Semiconductor Summer School at National Cheng Kung University, Taiwan, in 2024. This was a highly rewarding experience that provided firsthand exposure to cutting-edge research and advanced semiconductor technologies of Taiwan Semiconductor industry.

I would like to thank Dr. Gabriel Flizikowski, another dedicated and insightful postdoctoral researcher in our group for assisting me in nonlinear-optical

characterization of waveguides and data analysis. Device fabrication was carried out at the uOttawa NanoFab and the University of Waterloo fabrication facility, and I sincerely thank Dr. Spyros Ntais, Howard Northfield, Deepthi Shekhar, Dr. Mathieu De La Fontaine, Dr. Jeramy Upum, Dr. Luis Mayoral Astorga, and Dr. Hyung Choi for their assistance, training, and support in nanofabrication and imaging at the uOttawa NanoFab and Lais for the conducting fabrication efforts at University of Waterloo.

I would also like to thank Prof. Connor Kupchak from the Department of Electronics at Carleton University and Dr. Tara Moradi for their collaboration and insightful discussions on the design of ring resonators. My sincere thanks go to Dr. Nathalie Vermeulen from the Faculty of Engineering at Vrije Universiteit Brussel (VUB), and Dr. Siddarth Shivkumar for the enriching discussions on pump–probe spectroscopy, and to Dr. Kashif Awan for his assistance with RIE-ICP recipe optimization.

I am grateful to Sina Aghili, Mohammadreza Mohammadpour, Ozan Oner, and Lora Ramunno for their collaboration on the metasurface project for nonlinear applications. I also thank my colleagues Garen Simpson, Fatemeh Mousavi Karimi, Mohammad Amin Hemmatian, and Rania Mahjoub, Soheil Zibod, Yaswant Vaddi for their encouragement and creative discussions over the years. I am also grateful to my friends Ashlin Jacob, Bhavana Sathesh, and Melika Afshar for their continued support throughout this journey.

Additionally, I acknowledge the use of artificial intelligence tools (such as ChatGPT and Gemini) to assist in scripting and debugging Python code used for graphical visualization and data plotting.

Last but not least, I would like to express my deepest gratitude to my mother, sisters, my husband Jay, and rest of my family for their love, blessings, patience, and unwavering support.

List of Publications

1. **A. Thulaseedharan**, L. Fujii dos Santos, T. Moradi, C. Kupchak, and K. Dolgaleva, "Impact of nonlinear losses on the performance of InGaAsP-on-insulator ring resonators," *Journal of the Optical Society of America B*, vol. 43, no. 2, pp. A146–A151, 2026.

2. **A. Thulaseedharan**, L. Fujii dos Santos, S. Aghili, M. R. Mohammadpour, O. W. Oner, and K. Dolgaleva, "Tuning proximity effect correction for plasmonic metasurfaces," *Journal of the Optical Society of America B*, vol. 43, no. 2, pp. A132–A136, 2026.

3. S. Aghili, M. R. Mohammadpour, **A. Thulaseedharan**, L. Fujii dos Santos, L. Ramunno, and K. Dolgaleva, "Bi-layered stack plasmonic metasurface for high-resolution near-field second-harmonic generation microscopy applications," *Journal of the Optical Society of America B*, vol. 43, no. 4, pp. 1024–1033, 2026.

4. E. Mobini, O. W. Oner, K. Vyas, **A. Thulaseedharan**, K. M. Awan, F. M. Karimi, G. A. S. Flizikowski, L. Fujii dos Santos, D. H. G. Espinosa, and K. Dolgaleva, "C-band nonlinear optical interactions in InGaAsP/InP passive waveguides," *Journal of Physics: Photonics*, vol. 8, no. 1, p. 015039, 2026. DOI: 10.1088/2515-7647/ae38ac.

5. M. R. Mohammadpour, S. Aghili, **A. Thulaseedharan**, L. Fujii dos Santos, P. Ghavami, A. Staudte, L. Ramunno, and K. Dolgaleva, "Random plasmonic metasurface for enhanced second harmonic generation," in *2026 Photonics North (PN)*, pp. 1–2, 2026. DOI: 10.1109/PN70808.2026.11657697.

6. S. Aghili, M. R. Mohammadpour, **A. Thulaseedharan**, R. Alaee, and K. Dolgaleva, "THz emission engineering using resonant III-V semiconductor metamaterials," in *2025 Photonics North (PN)*, pp. 1–2, 2025. DOI: 10.1109/PN66844.2025.11097085.

7. K. Dolgaleva, L. Fujii dos Santos, G. A. S. Flizikowski, O. W. Oner, **A. Thulaseedharan**, K. Vyas, R. Boyd, S. Vijayakumar, and D. H. G. Espinosa, "Overview of the nonlinear photonics platforms at the telecom C-band," in *Smart Photonic and Optoelectronic Integrated Circuits 2025*, vol. PC13370, p. PC133700D, SPIE, 2025. DOI: 10.1117/12.3041397.

8. **A. Thulaseedharan**, G. A. S. Flizikowski, K. M. Awan, N. Vermeulen, and K. Dolgaleva, "Free carrier lifetime measurement in InGaAsP-on-InP strip-loaded waveguides," *Manuscript in preparation*, 2026.

9. L. Fujii dos Santos, **A. Thulaseedharan**, K. Varga, R. Mahjoub, F. M. Karimi, G. Simpson, O. W. Oner, and K. Dolgaleva, "Advances in III-V semiconductors on insulator platforms for integrated photonics," *Manuscript in preparation*, 2026.

10. M. R. Mohammadpour, S. Aghili, L. Fujii dos Santos, **A. Thulaseedharan**, A. Aghigh, E. Norris, J. Thompson, F. Légaré, L. Ramunno, and K. Dolgaleva, "Orientation-resolved SHG imaging: The role of near-field interactions," *Manuscript in preparation*, 2026.

Contents

Declaration of Authorship ii

Abstract iii

Acknowledgement v

List of Publications vii

List of Abbreviations xix

1 Introduction 1

1.1 Waveguide Optics . . . 5
1.2 Material Technologies in Integrated Photonics . . . 11
1.2.1 Optical Properties and Advantages of $In_{1-x}Ga_xAs_{1-y}P_y$ . . . 13
1.2.2 III-V on Insulator Photonics . . . 17
1.3 Light Propagation in Optical Waveguides . . . 19
1.4 Nonlinear Optics . . . 22
1.4.1 Second-Harmonics Generation . . . 23
1.4.2 Kerr Effect . . . 24
1.4.3 Self Phase Modulation . . . 25
1.4.4 Four-Wave Mixing . . . 28
1.5 Microring Resonators and Frequency Comb Generation . . . 30
1.6 Development of III-V-OI Platforms . . . 34
1.6.1 Wafer bonding . . . 35
Direct Bonding . . . 37
Adhesive Bonding . . . 37
1.6.2 Substrate thinning or removal . . . 37
1.7 Fabrication of III-V Photonic Components . . . 38

1.7.1 Electron Beam Lithography 39
Principle of Operation 40
E-beam Resist 42
Proximity Effect Correction 45
Dose correction 45
Background exposure correction 45
1.7.2 Plasma Etching 47
1.8 Metasurface Fabrication and PEC 49
1.9 InGaAsP Nonlinear Optical Characterization: Pump-Probe Measurement 51
1.10 Thesis Outline and Contributions 52

2 Free-Carrier Lifetime Measurement **55**
2.1 Two Photon Absorption and Free Carrier Absorption 56
2.2 Free-Carrier Lifetime: Significance and State of the Art 57
2.3 Fabrication of Strip Loaded waveguides 58
2.4 Free-carrier Lifetime Measurement 64

3 Impact of Nonlinear losses in InGaAsP-OI ring resonators **73**
3.1 Comb Modeling 74
3.2 Ring Design 77
3.3 Results and Discussion 79

4 Development of III-V-on Insulator Photonic Integration Platforms **85**
4.1 SiO_2 to SiO_2 direct bonding 87
4.2 Al_2O_3 to Al_2O_3 direct bonding 92
4.3 Adhesion bonding using Medusa 95
4.4 Substrate Removal for AlGaAs-OI 98
4.5 GaAs slow etch 100
4.6 GaAs fast etch recipe 102
4.7 Substrate removal in AlGaAs sample bonded to SiO_2 104

5 Tuning Proximity Effect Correction for Fabrication of Metasurfaces **108**
5.1 PEC used for metasurface fabrication 109
5.2 Metasurface design and fabrication 109
5.3 Proximity effect correction tuning 112

6 Conclusion and Future Work **116**

7 Metasurface Optical Transmission Measurement Setup **122**

8 Lugiato-Lefever Equation and Split-Step Fourier Transform **124**
8.1 Maxwell's equation and Nonlinear Wave Equation 124
8.1.1 Free Carrier Dynamics and Spatial Mode Separation . 127
8.2 Cavity Dynamics & Formulation of the Extended LLE 130
8.3 Normalization of the Lugiato-Lefever Equation 132
8.4 Split-Step Fourier Method 134

9 FC lifetime in p–n junction integrated InGaAsP-OI waveguides **137**

Bibliography **140**

List of Figures

1.1 (a) Schematic of a slab waveguide showing light confinement 1D (y) . The core (central layer) has refractive index n_1, and the cladding layers have refractive indices n_2 and n_3. (b) Cross-sectional view of a strip waveguide with a 2D confinement in both x and y directions. The core has refractive index n_4, the lower cladding has refractive index n_5, and the upper cladding is air [32]. 7

1.2 Representative electric field intensity distributions for guided spatial modes in a 2D channel waveguide: (a) fundamental quasi-TE_{00} mode, (b) fundamental quasi-TM_{00} mode, and (c–d) higher-order spatial modes (TE_{01} and TM_{01}). 8

1.3 Schematic of various optical waveguide geometries including (from left to right) embedded strip, strip, rib and strip-loaded. Darker shading indicates regions of higher refractive index [32]. 9

1.4 Basic layout of a photonic integrated circuit (PIC) showing photonic components integrated on a single substrate [36]. The red arrows indicate the propagation of optical signals through the various photonic components. 10

1.5 Comparison of electronic band structures and radiative transition mechanisms in (a) indirect bandgap semiconductor requiring phonon assistance to conserve crystal momentum, (b) direct bandgap semiconductor exhibiting momentum-conserving vertical transitions. Dashed line represents a virtual intermediate state. VB and CB indicate valance band and conduction band, respectively. 13

1.6 Three-dimensional plot illustrating the lattice constant a_0 of $In_{1-x}Ga_xAs_{1-y}P_y$ across the full composition range ($0 < x < 1.0$, $0 < y < 1.0$). Here, x and y are the fractions of gallium (Ga) and arsenic (As). The highlighted line in red corresponds to compositions that are lattice-matched to InP [23]. 15
1.7 Bandgap as a function of lattice constant for various III-V semiconductors. InGaAsP that are lattice-matched to InP substrates are positioned vertically along the dashed line [56]. 16
1.8 Schematic illustration of III–V-OI platforms, showing representative III–V guiding layers (a) AlGaAs (b) InSb (c) InGaAsP, and (d) GaAs integrated on a SiO_2 substrate. 18
1.9 (a) Schematic of principle of SHG (b) Energy-level diagram describing SHG. Doted line represents virtual energy states. Solid line represents atomic ground state. [71]. 23
1.10 Calculated normalized power spectral density (PSD) of a Gaussian pulse undergoing SPM for maximum nonlinear phase shifts of (a) $\phi_{max} = 0.5\pi$, (b) $\phi_{max} = 1.5\pi$, (c) $\phi_{max} = 2.5\pi$, and (d) $\phi_{max} = 3.5\pi$. As ϕ_{max} increases, spectral broadening and multi-peak oscillations develop due to intensity-dependent phase modulation. 27
1.11 Energy level diagram illustrating (a) degenerate Four-Wave Mixing, where two pump photons ($\hbar\omega_p$) generate a signal ($\hbar\omega_s$) and idler ($\hbar\omega_i$) photon pair, and (b) non-degenerate Four-Wave Mixing involving two distinct pump frequencies ($\hbar\omega_{p1}, \hbar\omega_{p2}$). 29
1.12 Schematic representation of (a) an add-through microring resonator (b) the optical transmission spectrum of a microring resonator. Destructive interference produces periodic resonance dips at frequencies ν_m and ν_{m+1} separated by the Free Spectral Range (FSR). 31
1.13 Principle of frequency comb generation: (a) pump mode overlapping with resonant mode of the ring; (b) degenerate FWM; (c) Cascaded FWM with FSR spacing indicated. 33
1.14 Steps involved in developing III-V-OI platform. 35
1.15 Different categories of bonding methods for III-V-OI (a) Direct wafer bonding (b) Adhesive bonding 36

1.16 Substrate thinning process using (a) lapping (b) grinding. The abrasive grains are are shown in gray with the chips generated from the mechanical removal of substrate material. 37
1.17 A schematic layout of an electron beam lithography tool [115]. 41
1.18 Steps in E beam lithography: (a) Surface preparation; (b) Spin-coating the resist; (c) E-beam exposure, and (d) Resist development. 42
1.19 Schematic illustration of (a) the cross-section of the e-beam patterned sample after development, and (b) the corresponding energy density deposited in the e-beam resist, shown as a function of horizontal position within the resist [117] 44
1.20 Schematic representation of the mechanisms involved in plasma etching: (a) chemical etching, (b) Ion-assisted chemical etching, (c) physical etching [129]. 48
1.21 Schematic of a plasmonic metasurface consisting of cross-shaped gold (Au) meta-molecules on a SiO_2 substrate, illustrating nonlinear frequency conversion from an incident pump beam (violet) to a generated output beam (teal) [131]. 49
1.22 A general schematic of pump probe technique for free carrier lifetime measurement. 51

2.1 An illustration of TPA and associated FCA in direct band gap materials. 56
2.2 General chemical structure of HSQ. The labels R and X represent terminal substituent groups bound to the silicon-oxygen core, where R and X are Hydrogen atoms in HSQ prior to cross linking. [172]. 60
2.3 (a) InGaAsP/InP waveguides etched using the ICP-RIE recipe optimized in 2022, showing smooth sidewalls and good etch quality (b) InGaAsP/InP waveguides etched on the same RIE-ICP etcher in a later year by us in our first attempt using the same recipe, showing poor selectivity and needle-like microstructures. 61

2.4 (a) Effect of increasing the chamber conditioning time from 15 min to 30 min, reducing the density of needle-like microstructures. (b) InGaAsP/InP waveguides fabricated with a chamber pressure of 0.45 Pa showing improvement in etch profile. . 62
2.5 SEM images of the fabricated InGaAsP/InP strip loaded waveguide using HSQ mask. 63
2.6 Simulated optical mode profiles of the fabricated waveguide with arrows showing direction of electric field vectors: (a) TE_{00} and (b) TM_{00} mode. The x and y axes indicate the transverse dimensions in micrometers. 64
2.7 Schematic of the pump-probe experimental setup used to measure free-carrier lifetime. 64
2.8 Top-view image of the sample mount on the translational stage: (a) mount associated with observed thermal instability in the probe signal; (b) mount providing enhanced thermal stability of the probe signal. 66
2.9 Normalized probe transmission over three pump pulse periods. 67
2.10 Normalized probe transmittance for input pump powers of 14 mW and pump wavelength of 1533 nm for (a) TM and (b) TE fundamental mode 67
2.11 Normalized probe transmittance at various pump power for fixed input probe powers of 87 mW and pump wavelength of 1533 nm for (a) TE and (b) TM fundamental mode 69
2.12 Free-carrier lifetime as a function of input pump powers at fixed pump wavelength of 1533 nm for TE (blue circles) and TM (red squares) fundamental mode 70

3.1 Schematic drawing of the ring resonator: (a) top view, (b) cross-section. 75
3.2 Dispersion as a function of wavelength for a range of (a) ring thicknesses, (b) ring widths, (c) ring radii, and (d) modeled GVD of the ring. 79
3.3 The mode area difference calculated across a range of ring widths and thicknesses 79

3.4 (a) Intensity as a function of detuning at 10 µW pump power, with the instability region highlighted. Simulated frequency spectra of the device at a detuning (b) before the instability region, (c) within the instability region, and (d) after the instability region. 80
3.5 (a) Temporal evolution of the intracavity field as a function of normalized detuning. (b) Evolution of the frequency comb spectrum with varying normalized detuning. 81
3.6 Simulated frequency spectra of the device collected at the through port of the bus waveguide: (a) in the absence of nonlinear losses, (b) with TPA included, (c) with TPA and FCA (3 ns and 0.46 ns FC lifetime), (d) with TPA and FCA (3 ps FC lifetime). 83
3.7 Simulated frequency spectra of the device with increased propagation loss at input power 2.6 mW. 83

4.1 Schematic illustration of SiO_2-to-SiO_2 direct bonding. 87
4.2 SEM image of the cross-section of partially successful directly bonded thermally grown SiO_2-to-SiO_2 layers on a silicon substrate, with bonding interface highlighted in yellow and voids indicated in red. 89
4.3 SEM image of the cross-section of successfully bonded thermally grown SiO_2-to-SiO_2 layers on a silicon substrate, with the bonding interface highlighted in yellow. 90
4.4 Optical microscopic images of surface of PECVD- deposited SiO_2 on InGaAsP after standard cleaning. 91
4.5 AFM images of the cleaved sample from a 2-inch SiO_2 /Si wafer after ALD deposition of Al_2O_3. Light red dots visible in the dark background are attributed to the residue generated during the cleaving process. 94
4.6 SEM images of the cross-section of SiO_2 bonded to InGaAsP using a Medusa intermediate adhesive layer, showing detachment of Medusa from the InGaAsP/InP wafer. 97

4.7 (a) AlGaAs/GaAs epitaxial stack used to optimize both fast and slow GaAs etching processes (b) Cross-sectional SEM images of the wet-etched sample, showing complete removal of the 100 nm GaAs layer beneath the underlying 300 nm-thick $Al_{0.7}Ga_{0.3}As$ layer. 100
4.8 AFM images of the AlGaAs/GaAs sample following the slow etch and subsequent NH_4OH/DI water cleaning. 102
4.9 AFM images of the GaAs surface after the fast etch at (a) room temperature and (b) 32 °C. 103
4.10 Illustration of the layer structure and individual layer thicknesses of the sample after substrate thinning. 104
4.11 SEM images of the lapped sample viewed from the side, showing the thickness of the remaining substrate near (a) the edges and (b) the central region of the substrate. 105
4.12 SEM images of the bonding region after wet etching, showing (a) epoxy seepage from the bonding region with approximately 12 µm of substrate remaining in Sample 1, and (b) epoxy delamination within the bonding region in Sample 2. 106

5.1 (a) Metasurface unit cell (not to scale). (b) Dimensions of a single antenna. 110
5.2 (a) SEM images of the fabricated nanoantennae without proximity-effect correction: (i) L-shaped, (ii) inverted L, (iii) V-shaped, (iv) inverted V-shaped antennae. (b) Comparison of the fabricated shapes with the intended design. The approximate contour of the shapes in (a) is shown in red, and the solid shapes represent the design. 111
5.3 (a) Critical points of the antennae highlighted by black squares at the edges. Solid lines: enforce exposure. Dashed lines: reduce exposure. (b) A metasurface unit cell with the proximity-effect correction applied. 112
5.4 SEM images of the fabricated nanoantennae: (a) L-shaped, (b) inverted L, (c) V-shaped, (d) inverted V-shaped antennae. The antenna with optimum PEC is highlighted by a blue circle. . . 113

5.5 (a) Transmission response of the corrected fabricated (orange) and designed (blue) metasurface for incident linearly polarized light. (b) Simulated transmission for the uncorrected shapes. 114

7.1 Schematic of the linear experimental setup. 122

9.1 Schematic cross-section of the device used for simulations, featuring a reverse-biased p-n junction integrated with a InGaAsP-OI waveguide. 137

9.2 Extracted effective carrier extraction time constant (τ_{ext} in picoseconds) across the 220 nm $\times$ 490 nm InGaAsP waveguide core as a function of reverse bias voltage. 138

List of Abbreviations

AlGaAs	Aluminium Gallium Arsenide
AlGaAs- OI	Aluminium Gallium Arsenide On Insulator
AFM	Atomic Force Microscope
BCB	Benzocyclobutene
BPM	Beam Propagation Method
$\chi^{(2)}$	Second-Order Nonlinear Susceptibility
$\chi^{(3)}$	Third-Order Nonlinear Susceptibility
CMOS	Complementary Metal-Oxide-Semiconductor
CW	Continuous Wave
DFG	Difference-Frequency Generation
DI	Deionized water
FCA	Free Carrier Absorption
FCD	Free Carrier Dispersion
FDTD	Finite-Difference Time-Domain
FEM	Finite Element Method
FSR	Free Spectral Range
FWM	Four-Wave Mixing
GVD	Group-Velocity Dispersion
GVM	Group-Velocity Mismatch
HCl	Hydrochloric acid
H_3PO_4	Phosphoric acid
ICP	Inductively Coupled Plasma
InGaAsP	Indium Gallium Arsenide Phosphide

InGaAsP- OI	Indium Gallium Arsenide Phosphide On Insulator
InP	Indium Phosphide
LNOI	Lithium Niobate-on-Insulator
MBE	Molecular Beam Epitaxy
MIR	Mid-Infrared
MOCVD	Metal-Organic Chemical Vapor Deposition
n_2	Nonlinear refractive index
NIR	Near-Infrared
OPO	Optical Parametric Oscillator
PEC	Proximity Effect Correction
PECVD	Plasma-Enhanced Chemical Vapor Deposition
PML	Perfectly Matched Layer
RIE	Reactive Ion Etching
SEM	Scanning Electron Microscope
SFG	Sum-Frequency Generation
SHG	Second Harmonic Generation
SOI	Silicon on Insulator
SPM	Self-Phase Modulation
TE	Transverse Electric
TM	Transverse Magnetic
TPA	Two-Photon Absorption
XPM	Cross-Phase Modulation

Dedicated to my mother.

Chapter 1

Introduction

The history of modern optical communication networks and information processing is fundamentally a story of developing optical waveguides, light generation, manipulation, and optical integration. Prior to the mid-twentieth century, optical communications relied almost entirely on unguided, free-space transmission-ranging from historical line-of-sight beacons and late eighteenth-century optical telegraph semaphores to early wireless light transmission experiments in the 1880 [1]. Although early wireless light links successfully demonstrated speech transmission over modulated sunlight, free-space optical channels were severely constrained by atmospheric attenuation, fog scattering, air turbulence, and optical diffraction. These environmental vulnerabilities rendered unguided optical networks impractical for high-capacity, weather-independent data transmission, highlighting the fundamental need for guided-wave architectures.

The paradigm shift toward guided-wave photonics began with the seminal theoretical proposal by Stewart E. Miller in 1969 [2]. Miller envisioned combining discrete optical elements such as miniature dielectric waveguides, optical switches, phase modulators, and photodetectors onto unified planar dielectric substrates. To draw a direct historical parallel to the microelectronics revolution that was transforming computing, Miller formally coined the term *'integrated optical circuit'*.

During this same transformative era, low-loss silica optical fibers dramatically reduced signal attenuation, while continuous-wave (CW) room-temperature semiconductor injection lasers provided practical light sources [3], [4], [5]. As

global data traffic expanded in subsequent decades, traditional microelectronic architectures encountered severe physical bottlenecks dictated by copper interconnect resistive latency, heat generation, and signal cross-talk at elevated clock frequencies. Moving optical channels directly onto microchips-scaling down to inter-chip and intra-chip optical interconnects emerged as the primary strategy to overcome these electrical bottlenecks [6]. Today, this bandwidth demand has experienced an unprecedented surge driven by modern Artificial Intelligence and machine learning workloads, making Photonic Integrated Circuits (PICs) critical infrastructure for AI acceleration, co-packaged optics (CPO), and optical compute engines [7].

Initial commercial advancements in integrated photonics focused heavily on Silicon-on-Insulator (SOI) technology due to its compatibility with established microelectronics manufacturing infrastructure and strong optical confinement [8]. However, elementary silicon possesses inherent physical boundaries when pushed beyond passive light routing, as its fundamental electronic band structure prevents efficient light generation on chip. Furthermore, under high optical power levels, silicon experiences power-dependent losses that restrict its performance [9]. To address these physical limit - namely inefficient light generation, extensive research has focused on integrating compound semiconductor light sources directly onto silicon photonics platforms. Recent engineering advances have demonstrated hybrid and heterogeneous integration architectures, where active III-V semiconductor dies or thin films are directly bonded onto pre-patterned silicon or silicon nitride (Si_3N_4) wafers [10], [11]. At the same time, progress in monolithic epitaxial growth has enabled quantum dot lasers grown directly on silicon, where quantum dot structures provide resilience against crystallographic lattice defects [12], [13]. Techniques such as micro-transfer printing have also emerged to enable high-throughput placement of pre-fabricated micro-scale light sources across silicon wafers [14]. However, despite these notable breakthroughs in integrated silicon light sources, challenges such as thermal dissipation across buried oxide layers, lattice defect accumulation during direct epitaxy, on-chip optical feedback sensitivity without bulky isolators, and transition losses at material interfaces continue to complicate large-scale commercial yield [15], [16]. Consequently, compound semiconductor platforms remain indispensably at the core of optical generation, amplification,

and high-performance optoelectronic signal processing. [17], [18], [19], [20]

In contrast to elemental semiconductors such as Silicon and Germanium, direct-bandgap III-V semiconductor platforms enable fully monolithically integrated photonics allowing passive waveguides, electro-optic modulators, photodetectors, and active optical gain sources such as lasers and optical amplifiers to co-exist on a single substrate [21], [22]. This method of integration significantly reduces coupling insertion losses, back-reflections, and latency associated with multi-chip optical packaging interfaces. Furthermore, pure III-V materials like Indium Phosphide (InP) exhibit significantly higher electron mobility than silicon, making them superior for high-speed, low-power telecommunication, microwave-photonic, and sensing applications.

Among III-V semiconductor materials, the quaternary alloy Indium Gallium Arsenide Phosphide ($In_{1-x}Ga_xAs_yP_{1-y}$) occupies a paramount position in optical communications. By adjusting its material composition during epitaxial growth, this quaternary material can be continuously engineered to match the lattice of native InP substrates while tuning the operating wavelength across the primary telecommunication bands; most notably the telecom C-band ($1530 - 1565$ nm), which corresponds to the global minimum loss spectrum of optical fibers underpinning long-haul networks and data centers [23]. While commercial InP foundries, for example Canadian Photonics Fabrication Centers (CPFC) excel in the linear optical regime for transceiver architectures operating in the linear optical regime, native substrates suffer from weak refractive index contrast between the guiding core and the surrounding cladding. This low index contrast demands large waveguide cross-sections and wide bending radii to prevent severe radiative bend loss, ultimately restricting integration density and light intensity [24], [25]. To overcome these structural boundaries, research has shifted toward III-V-on-Insulator (III-V-OI) architectures, such as Indium Gallium Arsenide Phosphide-on-Insulator (InGaAsP-OI) [26]. By heterogeneously bonding thin, single-crystal III-V semiconductor films onto low-index carrier substrates followed by selective native substrate removal, a high index contrast platform is realized [27]. This strong mode confinement shrinks waveguide footprints to sub-micron cross-sections, allowing sharp bending radii, boosting optical field intensities, and enabling precise control over optical dispersion.

Crucially, InGaAsP exhibits a significantly higher Kerr nonlinear response, which is orders of magnitude higher than silica (SiO_2) or silicon nitride (Si_3N_4) [28], [29]. While related platforms such as Aluminum Gallium Arsenide-on-Insulator (AlGaAs-OI) have been widely studied for nonlinear photonics due to wide bandgap engineering that suppresses high-power losses [30], [31], InGaAsP remains uniquely attractive because it offers a direct path toward co-integrating active C-band optoelectronics with nonlinear optical processing within an established commercial foundry platform. Incorporating nonlinear optical signal processing-such as self-phase modulation, four-wave mixing, and Kerr optical frequency comb generation-directly onto InGaAsP platforms bridges the gap between active C-band optoelectronics and passive nonlinear signal processing.

Despite these evident physical advantages, using InGaAsP-OI for Kerr optical frequency comb generation remains largely unexamined in the literature. Fully realizing this platform requires addressing critical physical and nanofabrication constraints, high optical intensities induce power-dependent absorption near telecom wavelengths and its associated free-carrier dynamics. Furthermore, achieving favorable wave propagation conditions across the C-band requires careful geometric design to counteract intrinsic material characteristics, while dedicated wafer bonding and substrate removal workflows must be engineered to yield low-loss, high-quality material stacks.

This thesis systematically investigates the feasibility of the InGaAsP-OI platform for nonlinear optical signal processing and Kerr frequency comb generation. To achieve this, we first experimentally quantify free-carrier recombination dynamics in fabricated InGaAsP waveguides using pump-probe technique, providing the critical dynamics required to accurately model nonlinear phase accumulation. Building on these empirical dynamics, we establish numerical models to evaluate the feasibility of Kerr frequency comb generation in InGaAsP-OI microring resonators, incorporating material dispersion, Kerr phase shifts, power-dependent absorption, and free-carrier effects. Finally, we evaluate direct and adhesive wafer bonding methodologies to

establish reliable fabrication pathways for obtaining high-confinement platform stacks. Through this combined experimental, numerical, and fabrication study, this work establishes the foundation for realizing C-band nonlinear photonic devices on InGaAsP-OI platform. Future efforts must build on this foundation by implementing active p–n junction carrier sweep-out in microring resonators, optimizing Al_2O_3 and Hydrogen Silsesquioxane (HSQ) wafer bonding to resolve substrate removal peeling, and experimentally validating low-threshold Kerr comb generation.

To contextualize this work, this chapter establishes the foundational principles governing integrated waveguide optics, semiconductor material platforms, light propagation in dispersive nonlinear optical media, microring resonators, and nonlinear optical characterization method used to extract key parameters for InGaAsP-OI devices.

1.1 Waveguide Optics

Waveguide optics describes how light is guided and confined within a high-refractive-index region (core or guiding layer) surrounded by lower-index materials (cladding), primarily through total internal reflection (TIR) [32]. While ray optics provides an intuitive picture of guidance via TIR, a complete description requires treating light as an electromagnetic wave [33]. In dielectric waveguides, light propagates only in the form of bound electromagnetic modes (guided modes) supported by the refractive index contrast and geometry of the waveguide [32]. These guided modes represent spatial electromagnetic field distributions

$$\vec{E}(x,y,z,t) = \vec{E}(x,y)e^{i(\omega t-\beta z)}; \tag{1.1}$$

$$\vec{H}(x,y,z,t) = \vec{H}(x,y)e^{i(\omega t-\beta z)}, \tag{1.2}$$

that are solutions of Maxwell's equations satisfying the continuous boundary conditions at the material interfaces [33], [34]. Here, β is the propagation constant of a guided mode along the propagation direction (z), defined as

$$\beta = k_0 n_{\text{eff}}, \tag{1.3}$$

where k_0 is the vaccum wavenumber defined as

$$k_0 = \frac{2\pi}{\lambda_0}, \tag{1.4}$$

and n_{eff} is the modal effective index. For a mode to remain strictly guided and bound within the core, its effective index must satisfy the condition given by

$$n_{\text{cladding}} < n_{\text{eff}} < n_{\text{core}}. \tag{1.5}$$

If n_{eff} falls below n_{cladding}, the field is no longer confined and escapes into the surrounding cladding as a radiation mode [34].

The analytical solution to Maxwell's equations is generally tractable only for one-dimensional (1D) planar slab waveguides as shown in Figure 1.1 (a), where the core extends infinitely in one lateral direction ($\partial/\partial x = 0$) and the fields can be decoupled strictly into pure Transverse Electric (TE, $E_z = 0$) and Transverse Magnetic (TM, $H_z = 0$) modes [33], [34]. In contrast, practical two-dimensional (2D) channel waveguides exhibit optical confinement in both transverse dimensions (x and y). A schematic of cross-sectional view of a channel waveguide is shown Figure 1.1 (b). Due to the corner boundary conditions inherent to 2D cross sections, pure TE or TM modes do not exist; instead, the guided solutions are hybrid "quasi-TE" and "quasi-TM" modes, which must be calculated numerically using methods such as Finite Difference Eigenmode (FDE) or Finite Difference Time Domain (FDTD) solvers [35].

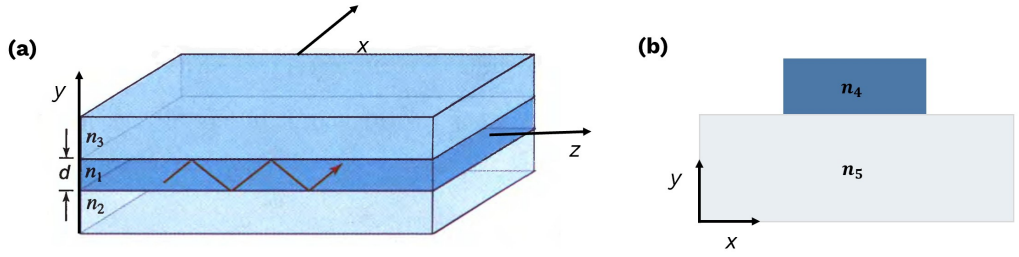


FIGURE 1.1: (a) Schematic of a slab waveguide showing light confinement 1D (y) . The core (central layer) has refractive index n_1, and the cladding layers have refractive indices n_2 and n_3. (b) Cross-sectional view of a strip waveguide with a 2D confinement in both x and y directions. The core has refractive index n_4, the lower cladding has refractive index n_5, and the upper cladding is air [32].

In 2D channel waveguides, spatial modes are classified by their polarization state and transverse nodal indices, denoted as TE_{mn} and TM_{mn}, where m and n represent the number of zero-crossings (nodes) in the field intensity profile along the horizontal (x) and vertical (y) transverse axes, respectively [35]. As shown in Figure 1.2 (a) the fundamental TE_{00} mode features a single intensity maximum with no transverse field nodes ($m = 0, n = 0$), with its primary electric field vector polarized parallel to the substrate plane ($E_x \gg E_y$). Similarly, the fundamental TM_{00} mode also exhibits a single intensity peak with no transverse field nodes as shown in Figure 1.2 (b), but its primary electric field vector is polarized perpendicular to the substrate plane ($E_y \gg E_x$). Higher-order modes, such as TE_{01} or TM_{01}, exhibit multiple spatial lobes separated by field nodes, as shown in Figure 1.2 (c) and (d) respectively. Depending on the physical cross-sectional dimensions and wavelength, waveguides can support single-mode or multi-mode propagation [33]. Single-mode operation (restricting propagation strictly to TE_{00} and TM_{00}) is typically desired in integrated optics to eliminate intermodal dispersion and to maintain signal integrity.

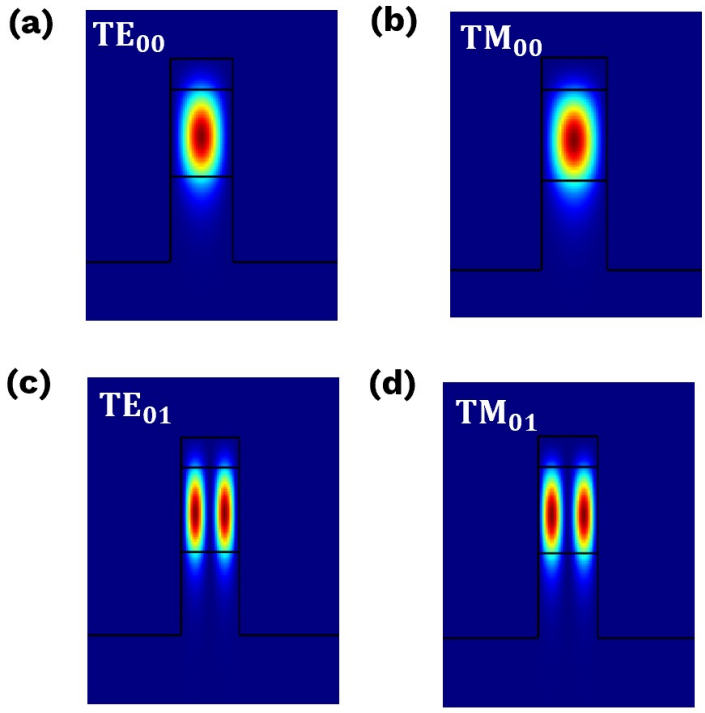


FIGURE 1.2: Representative electric field intensity distributions for guided spatial modes in a 2D channel waveguide: (a) fundamental quasi-TE_{00} mode, (b) fundamental quasi-TM_{00} mode, and (c–d) higher-order spatial modes (TE_{01} and TM_{01}).

Depending on the material platform, as well as fabrication and etching geometry, channel waveguides we discussed can take several forms, including embedded strip, strip, rib, and strip-loaded waveguides, as illustrated in Figure 1.3 [32]. In this work, we experimentally study InGaAsP/InP waveguides that have a strip-loaded geometry [32], while theoretically exploring FCG in an InGaAsP-OI waveguide represented by a strip geometry.

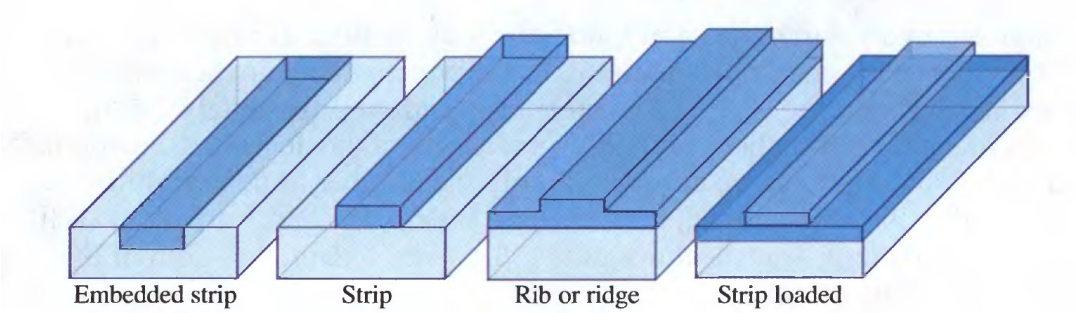


FIGURE 1.3: Schematic of various optical waveguide geometries including (from left to right) embedded strip, strip, rib and strip-loaded. Darker shading indicates regions of higher refractive index [32].

While individual optical waveguides represent the fundamental building blocks of integrated optics, a functional Photonic Integrated Circuit (PIC) relies on the dense integration of both active and passive devices on a single chip [36]. Active devices require electrical or optical power to generate, modulate, or detect light, whereas passive devices route, split, or filter light purely through their geometrical designs without any external power. Figure 1.4 presents a schematic of the basic components of a PIC and their roles in manipulating optical signals on a single chip [36]. The red arrows indicate the propagation of optical signals through the various photonic components [36]. Light generated by a laser is coupled into the chip through an input coupler, which transfers the optical signal from an optical fiber to an on-chip optical waveguide [36]. The waveguides route light between different components, while directional couplers split or combine optical signals and distribute optical power throughout the circuit [36]. Depending on the application, the guided light may interact with an optical ring resonator, where resonant light confinement enables wavelength-selective filtering, sensing, and nonlinear optical processes, or with an optical modulator, which encodes electrical information onto the optical carrier by varying its amplitude, phase, or frequency [36].

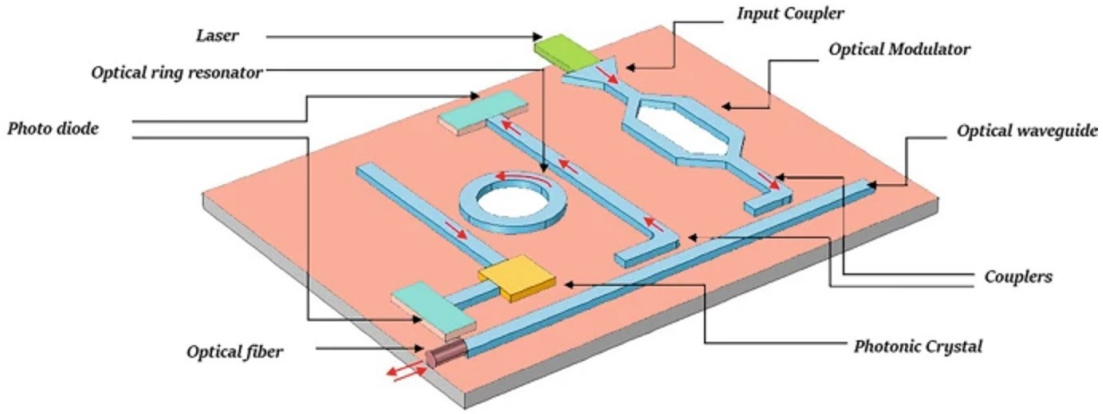


FIGURE 1.4: Basic layout of a photonic integrated circuit (PIC) showing photonic components integrated on a single substrate [36]. The red arrows indicate the propagation of optical signals through the various photonic components.

Following optical processing, the signal is directed to a photodiode for conversion into an electrical signal for detection and analysis [36]. The figure also highlights a photonic crystal – a periodic dielectric structure that offers robust light confinement and enables key functions like filtering, slow-light propagation, and enhanced light-matter interaction [36]. By integrating passive elements (such as waveguides, microring resonators, couplers, and photonic crystals) with active devices (including lasers, modulators, and photodiodes) on a single substrate as illustrated in Figure 1.4, photonic integrated circuits deliver compact, stable, and power-efficient systems capable of advanced optical signal processing and communication [36]. This thesis focuses primarily on two of the photonic components illustrated in Figure 1.4, waveguides and ring resonators.

1.2 Material Technologies in Integrated Photonics

TABLE 1.1: Nonlinear integrated photonics material platforms.

Material	**Structure & Symmetry**	E_g **(eV)**	**Index (**n**)**	$\chi^{(2)}$ **/** $\chi^{(3)}$	n_2 **(m^2/W)**	**NL Loss (TPA+FCA)**	**Capability & Limitations**
SOI [9], [37], [38]	Crystalline /Centrosymmetric	1.12	3.45	$\chi^{(3)}$ only	4.5×10^{-18}	High TPA + FCA at 1550 nm	Passive routing; high Δn; no native gain.
Si_3N_4 [39], [40]	Amorphous /Centrosymmetric	~ 5.0	2.00	$\chi^{(3)}$ only	2.4×10^{-19}	Negligible TPA	Ultra-low loss ($<$ 0.1 dB/m); lower Δn; no gain.
$LiNbO_3$ [41], [42]	Crystalline /Non-centrosym.	4.00	2.20	$\chi^{(2)}$ & $\chi^{(3)}$	1.8×10^{-19}	Negligible TPA	High $\chi^{(2)}$; fast E/O modulators; no gain.
InP [20], [43]	Crystalline /Non-centrosym.	1.35	3.17–3.4	$\chi^{(2)}$ & $\chi^{(3)}$	$\sim 5 \times 10^{-18}$	High TPA + FCA at 1550 nm	Monolithic integration; weak Δn.
AlGaAs-OI [30], [44]	Crystalline /Non-centrosym.	1.42–2.0	> 3.3	$\chi^{(2)}$ & $\chi^{(3)}$	$\sim 1.5 \times 10^{-17}$	Low TPA	high n_2; high Δn; no gain at 1550 nm
InGaAsP-OI [28], [45]	Crystalline /Non-centrosym.	0.73–1.35	3.2–3.5	$\chi^{(2)}$ & $\chi^{(3)}$	$\sim 1 \times 10^{-17}$	High TPA + FCA at 1550 nm	Monolithic integration; high Δn; high n_2 at 1550 nm.

The selection of a material platform for Photonic Integrated Circuits (PICs) is dictated by the targeted application, typically requiring a fundamental balance of core physical parameters-such as leveraging high second-order nonlinear susceptibility ($\chi^{(2)}$) for electro – optic modulation, wide bandgap energy (E_g) for high-power passive routing, or large third-order optical nonlinearity ($\chi^{(3)}$) and high refractive index (n) for compact Kerr nonlinear devices [46]. As summarized in Table 1.1, no single material system simultaneously optimizes optical gain, high refractive index contrast (Δn), and suppressed nonlinear losses at telecommunication wavelengths (1530-1565 nm). Consequently, integrated photonics has evolved into a multi-platform landscape governed by specific physical mechanisms and device integration requirements.

A primary structural bottleneck in native III-V semiconductor platforms, such as InGaAsP/InP, is the low refractive index contrast ($\Delta n \approx 0.2$—0.3) between the waveguiding core layer (typically InGaAsP) and its cladding or substrate [21], [47], [48]. This weak optical confinement mandates wide bending radii to prevent radiative bending loss, thereby limiting device integration density [49]. Conversely, insulator-backed architecture; pioneered by SOI and extended to III-V-OI structures via wafer bonding; introduces a high refractive index contrast ($\Delta n > 1.8$) by utilizing a low- refractive index dielectric buried cladding (SiO_2, $n \approx 1.45$) [46], [50], [51]. This strong spatial confinement enables sub-micron waveguide cross-sections, tight micrometer-scale bend radii, and enhanced light-matter interaction essential for dense photonic circuits.

For nonlinear optical applications, the operational power handling and Kerr phase accumulation are fundamentally constrained by nonlinear losses created by multi-photon absorption. In wide-bandgap platforms such as Si_3N_4 ($E_g \approx 5.0$ eV) and high aluminum content AlGaAs (AlGaAs-OI, $x_{Al} > 0.18$), two-photon absorption (TPA) is completely suppressed at 1550 nm because the photon energy is below half the bandgap ($2\hbar\omega < E_g$) [39], [44]. In contrast, elemental silicon ($E_g \approx 1.12$ eV) and narrow-gap III-V semiconductors such as InGaAsP, experience significant TPA at telecom frequencies, generating free carriers that induce free-carrier absorption (FCA) that affects nonlinear phase shift.

Despite these nonlinear loss limitations, InGaAsP-OI retains a unique role among III-V-OI platforms. Through stoichiometric tuning of the quaternary alloy $In_{1-x}Ga_xAs_yP_{1-y}$ lattice-matched to InP ($x \approx 0.47y$), the bandgap can be engineered across 0.73–1.35 eV, yielding an exceptionally high Kerr nonlinear coefficient ($n_2 \approx 1 \times 10^{-17}$ m^2/W at 1550 nm) alongside native optical gain within the telecom C-band [28], [29].

The strong sub-micron modal confinement offered by the InGaAsP-OI architecture ($\Delta n \approx 1.83$) dictates the geometric dispersion engineering required for phase-matched nonlinear processes. In the next section we will discuss the physics behind the optical properties of InGaAsP.

1.2.1 Optical Properties and Advantages of $In_{1-x}Ga_xAs_{1-y}P_y$

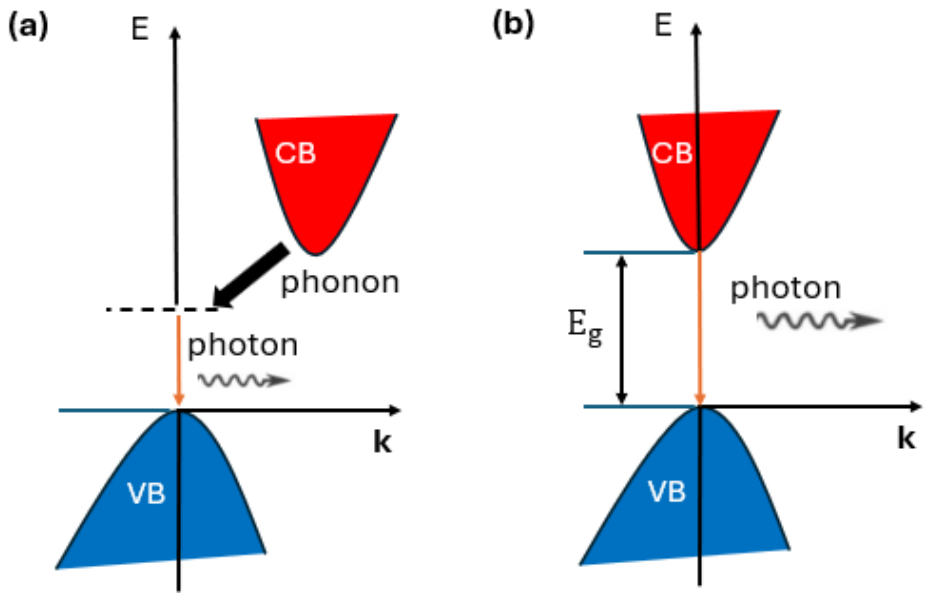


FIGURE 1.5: Comparison of electronic band structures and radiative transition mechanisms in (a) indirect bandgap semiconductor requiring phonon assistance to conserve crystal momentum, (b) direct bandgap semiconductor exhibiting momentum-conserving vertical transitions. Dashed line represents a virtual intermediate state. VB and CB indicate valance band and conduction band, respectively.

Fundamentally, the optical absorption and emission characteristics of any semiconductor used in a photonic platform are dictated by its energy-momentum (E-$\mathbf{k}$) dispersion relation [17]. In indirect bandgap semiconductors like silicon or germanium, the conduction band minimum and valence band maximum occur at different crystal momentum vectors ($\mathbf{k}$), as shown in Figure 1.5 (a). Consequently, optical transitions require phonon interactions (lattice vibrations) to conserve momentum, rendering radiative absorption and emission processes inherently inefficient. In contrast, InGaAsP is a direct bandgap

semiconductor where the conduction band minimum and valance band maximum align at $\mathbf{k} = 0$, as shown in Figure 1.5 (b). Because optical photons carry negligible momentum relative to electrons, transitions occur vertically in E-$\mathbf{k}$ space without requiring phonons [52]. This enables momentum-conserving, highly efficient optical absorption, spontaneous emission, and stimulated amplification, making direct-bandgap semiconductors exceptional light emitters and the foundational material choice for semiconductor lasers and light-emitting diodes (LEDs). This direct bandgap structure gives Indium Phosphide (InP) integration technology a distinct advantage over silicon through monolithic integration. InP- based material platforms can efficiently emit and amplify light while simultaneously supporting passive components such as waveguides and splitters, allowing both active and passive components to be integrated on the same wafer – a capability that silicon lacks.

However, leveraging these material advantages at scale presents manufacturing challenges. Complementary Metal Oxide Semiconductor (CMOS) is the dominant semiconductor manufacturing technology for electronic integrated circuits and has become the foundation of modern silicon photonics [53]. Over several decades, CMOS technology has evolved into a mature global fabrication ecosystem characterized by highly standardized manufacturing processes, exceptional scalability, high production yields, and cost-effective high-volume manufacturing through commercial foundries [8]. Its proven ability to support continuous increases in integration density has established an unparalleled worldwide manufacturing infrastructure, making CMOS compatibility a key objective for scalable photonic integration [54], [55]. However, unlike silicon, InP is not compatible with conventional CMOS fabrication, limiting its access to these standard foundry services. Standard CMOS manufacturing relies on repeated steps such as deposition, photolithography, ion implantation, etching, metallization, and passivation that are strictly optimized for silicon. The differing lattice structures, chemical properties, and processing chemistries of III-V semiconductor materials like InP prevent them from being processed in standard CMOS fabs [43]. Nevertheless, specialized III-V semiconductor foundry services, such as the Heinrich-Hertz Institut (HHI) and SMART Photonics, have emerged to provide dedicated fabrication processes specifically for InP photonic integrated

circuits [43].

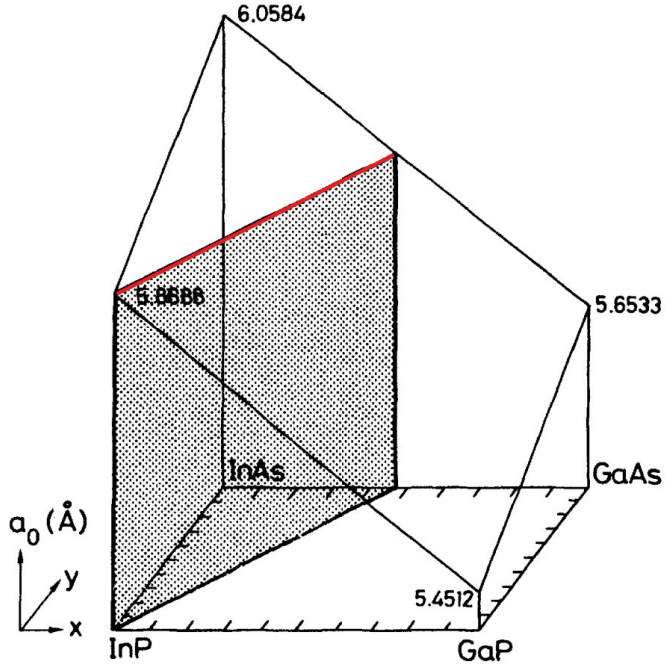


FIGURE 1.6: Three-dimensional plot illustrating the lattice constant a_0 of $In_{1-x}Ga_xAs_{1-y}P_y$ across the full composition range $(0 < x < 1.0,\ 0 < y < 1.0)$. Here, x and y are the fractions of gallium (Ga) and arsenic (As). The highlighted line in red corresponds to compositions that are lattice-matched to InP [23].

Within this InP ecosystem, $In_{1-x}Ga_xAs_yP_{1-y}$ serves as a crucial quaternary alloy derived from InP, GaAs, GaP, and InAs. The various possible compositions of this quaternary alloy by varying the Ga fraction (x) and As (y) fraction correspond to a continuous range of lattice constants a_0, as shown in Figure 1.6. The shaded region in this figure represents all attainable compositions, while the highlighted line indicates compositions that are lattice-matched to the InP substrate ($a_0 \approx 5.8688$ Å). Staying along this specific compositional boundary allows for defect-free, strain-free epitaxial growth using techniques such as molecular beam epitaxy (MBE) or metal-organic chemical vapor deposition (MOCVD).

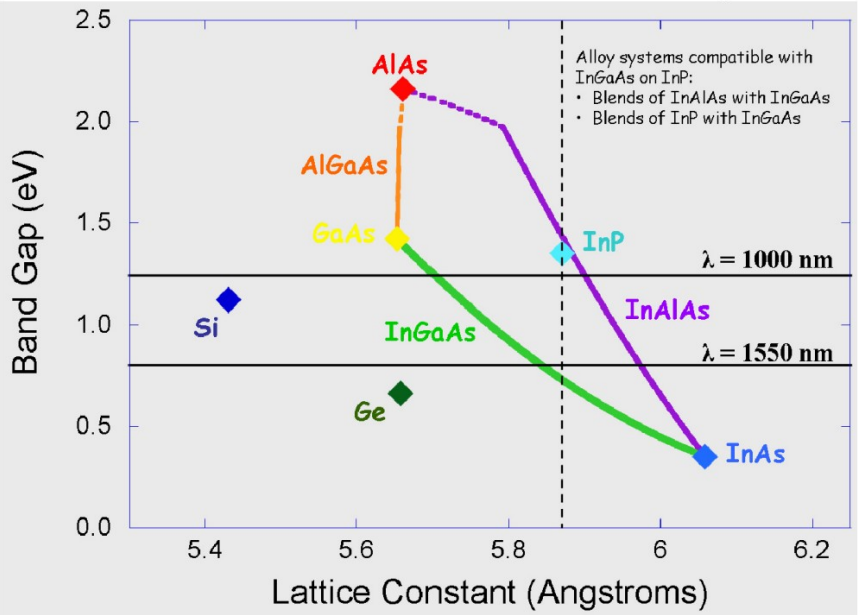


FIGURE 1.7: Bandgap as a function of lattice constant for various III-V semiconductors. InGaAsP that are lattice-matched to InP substrates are positioned vertically along the dashed line [56].

By simultaneously adjusting the x and y along this lattice-matched line, the material's bandgap can be continuously engineered without introducing structural strain. As illustrated in the bandgap versus lattice constant diagram in Figure 1.7, lattice-matched InGaAsP lies vertically along the dashed line between InP and InGaAs [56]. Along this vertical line, the direct bandgap energy E_g can be tuned from 0.73 eV to 1.35 eV, comprehensively spanning the near-infrared spectrum as well as the standard telecommunications O- and C-bands. This bandgap energy as a function of the compositional parameter y (fraction of arsenic) is described empirically by

$$E_g(y) = 0.75 + 0.46y + 0.14y^2 \quad [\text{eV}], \tag{1.6}$$

where y controls the quaternary alloy composition along the lattice-matched boundary.

This precise compositional tuning directly dictates the material's dielectric response. In the telecom C-band ($\sim$ 1550nm), the linear refractive index n ranges from 3.2 ($y = 0.9$) to 3.6 ($y = 0.1$), providing strong optical field

confinement when integrated with lower-index cladding materials such as SiO_2 ($n = 1.45$). Beyond its linear optical response, the InGaAsP platform exhibits a remarkably high Kerr nonlinear refractive index n_2 on the order of 1.9×10^{-17} m^2/W, which is considerably higher than that of silicon (5×10^{-18} m^2/W) [28], [57]. This strong optical nonlinearity makes InGaAsP exceptionally well-suited for nonlinear applications at telecommunication wavelengths, allowing for compact chips capable of highly efficient all-optical signal processing at relatively low optical intensities.

1.2.2 III-V on Insulator Photonics

The III–V on insulator (III-V-OI) platform involves integrating a III–V semiconductor core layer onto a silica (SiO_2) cladding as shown in Figure 1.8. This configuration inherently provides a high refractive index contrast between the core and the cladding, which leads to strong optical confinement [58], [59]. As a result, light can be tightly confined within the core, enabling more compact integrated photonic devices. For example, waveguides can support small bending radii without incurring significant bending losses [60]. From a fabrication standpoint, the strong mode confinement also relaxes tolerance to sidewall roughness introduced during dry etching [61]. Because the optical mode remains concentrated near the center of the core cross-section, its overlap with the etched sidewalls is reduced, thereby limiting scattering losses. Another key advantage of the III–V-OI platform is the relative ease of dispersion engineering [62]. Owing to the high confinement, the geometrical (waveguide) dispersion can dominate over the intrinsic material dispersion. This shift allows more direct and flexible control over the total dispersion of the device through waveguide or device design [63]. Finally, the enhanced optical confinement significantly strengthens nonlinear light–matter interactions [58]. By increasing the optical intensity within a small modal area, the III–V-OI platform improves the efficiency of nonlinear optical processes, making it highly attractive for advanced photonic applications [61], [64].

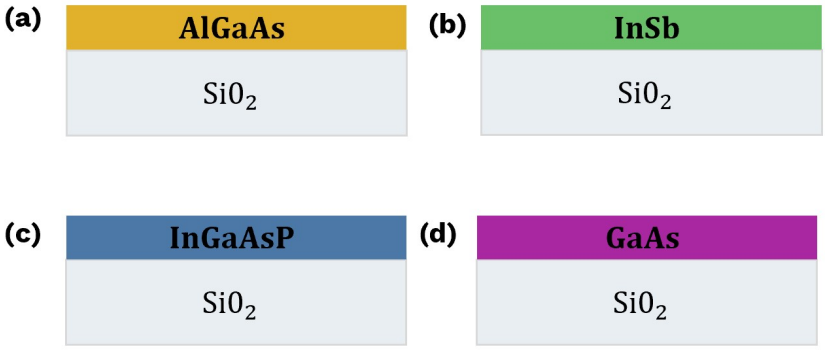


FIGURE 1.8: Schematic illustration of III–V-OI platforms, showing representative III–V guiding layers (a) AlGaAs (b) InSb (c) InGaAsP, and (d) GaAs integrated on a SiO_2 substrate.

III–V integration on substrates such as silicon or silica is explored in the literature primarily through two main approaches: direct growth and heterogeneous integration [12], [65]. Direct growth techniques, such as aspect ratio trapping (ART), involve growing III–V materials selectively within narrow silica trenches on silicon substrates [65]. While scalable, this method suffers from crystal defects caused by lattice and thermal expansion mismatches between III–V semiconductors and silicon or silica, and it is inherently restricted in geometry [65]. In contrast, heterogeneous integration typically involves bonding pre-fabricated III–V semiconductor laser dies onto passive platforms such as silicon or silicon nitride (Si_3N_4). This technique avoids lattice mismatch constraints by joining the materials using direct molecular, adhesive, or metallic wafer bonding [66]. Although this approach successfully combines active and passive functionality on one chip, it introduces significant fabrication complexity, requiring sub-micron die-alignment precision, intricate mode-coupling tapers between layers, and complex heat dissipation management [66].

Wafer bonding prior to any device patterning offers a compelling alternative to avoid die-level alignment challenges [30], [44]. By first bonding the full III–V semiconductor layer onto the silica-clad host substrate and removing the growth substrate, the resulting stack functions effectively as a monolithic wafer. Consequently, complete photonic circuits—including waveguides, microringresonators, and active elements—can be defined and etched

across the chip in a single lithographic patterning step. This eliminates the need for individual die positioning and multi-layer optical coupling, providing a streamlined, single-step fabrication route for high-confinement nonlinear photonics. This blanket wafer bonding strategy is adopted in this work for the realization of the III–V-OI platforms, and the detailed fabrication process flow is discussed in upcoming sections of this thesis.

Current research efforts on III–V-OI platforms development worldwide investigate various III–V semiconductor material systems as guiding layers and their applications in photonic devices, as illustrated in Figure 1.8. For instance, AlGaAs on insulator (AlGaAs-OI) has been mostly demonstrated for waveguide devices and high-Q ring resonators [58]. Indium antimonide on insulator (InSb-OI) has been explored theoretically for metasurface designs with potential bioimaging applications [67]. InGaAsP-OI platform has been demonstrated for waveguide-based devices used in variable optical attenuation of optical signals [26]. Similarly, GaAs on insulator (GaAs-OI) structures have been used for second harmonic generation [68]. While these advancements highlight the versatility of III-V-OI platforms, this thesis specifically focuses on expanding the capabilities of the InGaAsP-OI platform for nonlinear photonic applications. We investigate optical frequency comb generation in InGaAsP-OI microring resonators, alongside the foundational nanofabrication techniques–specifically wafer bonding for InGaAsP-OI and substrate removal for AlGaAs-OI–while addressing key technical challenges and proposing viable mitigation strategies.

1.3 Light Propagation in Optical Waveguides

Following the analysis of guided optical modes and spatial field confinement in channel waveguides, it is essential to examine how the phase and velocity of guided light vary across its constituent optical frequencies [69]. In integrated optical waveguides, chromatic dispersion governs this frequency dependence and arises from two distinct physical mechanisms: material dispersion and waveguide dispersion [33].

At the atomic level, material dispersion (D_{mat}) originates from the intrinsic dielectric response of the material. Bound electrons act as damped harmonic

oscillators that respond to the electric field of propagating light. Because optical frequencies lie near electronic bandgap resonances (such as the interband transitions in semiconductor layers like InGaAsP), the material's bulk refractive index $n(\omega)$ inherently varies with wavelength of the propagating light [23].

In contrast, waveguide dispersion (D_{wg}) is a structural phenomenon determined by spatial boundary conditions and light confinement in high-index contrast geometries [33]. Longer-wavelength (lower-frequency) components exhibit broader spatial mode profiles that extend further into the cladding material, whereas shorter-wavelength components remain tightly confined within the high-index core. Consequently, the guided mode experiences a frequency-dependent effective refractive index $n_{\text{eff}}(\omega)$ that can differ significantly from the bulk index of either constituent material.

The total chromatic dispersion experienced by light in a waveguide is the direct superposition of these two physical contributions [33]:

$$D_{\text{total}}(\lambda) = D_{\text{mat}}(\lambda) + D_{\text{wg}}(\lambda). \tag{1.7}$$

In semiconductor platforms such as InGaAsP-OI operating in the C-band, the bulk material dispersion is strongly normal ($D_{\text{mat}} < 0$) [23]. To enable ultrafast pulse propagation, Kerr frequency comb generation, or phase-matched nonlinear optical interactions, controlling this total dispersion is critical. By tailoring the waveguide cross-sectional dimensions (width, height, and sidewall angle), geometric waveguide dispersion (D_{wg}) can be engineered to be strongly anomalous, thereby overcoming the intrinsic normal material dispersion to yield a net anomalous total dispersion ($D_{\text{total}} > 0$) [70].

To mathematically model light propagation under these combined dispersion mechanisms, the spatial phase evolution of a monochromatic guided wave along the z-axis is described by the mode propagation constant (or effective wavenumber) $\beta(\omega)$ [69]

$$\beta(\omega) = \frac{\omega}{c} n_{\text{eff}}(\omega) = k_0 n_{\text{eff}}(\omega), \tag{1.8}$$

where c is the speed of light in vacuum, $n_{\text{eff}}(\omega)$ is the effective refractive

index calculated from the waveguide cross-section, and k_0 is the vacuum wavenumber.

For an optical pulse or multi-frequency interaction centered at a carrier frequency ω_0, the propagation constant $\beta(\omega)$ is expanded in a Taylor series around ω_0 [69]

$$\beta(\omega) = \beta_0 + \beta_1(\omega - \omega_0) + \frac{1}{2}\beta_2(\omega - \omega_0)^2 + \frac{1}{6}\beta_3(\omega - \omega_0)^3 + \dots, \tag{1.9}$$

where the expansion coefficients correspond to the m-th order derivatives evaluated at ω_0

$$\beta_m = \left.\frac{\mathrm{d}^m\beta}{\mathrm{d}\omega^m}\right|_{\omega=\omega_0} \quad (m = 0, 1, 2, \dots). \tag{1.10}$$

The primary expansion terms carry physical significance regarding pulse propagation and phase velocity matching. The zeroth-order term $\beta_0 = \beta(\omega_0)$ represents the phase shift per unit length, defining the phase velocity v_p [69]

$$v_p = \frac{\omega_0}{\beta_0} = \frac{c}{n_{\text{eff}}(\omega_0)}. \tag{1.11}$$

The first-order term β_1 defines the group velocity v_g, which specifies the speed at which the temporal envelope travels through the waveguide [69]:

$$\beta_1 = \left.\frac{\mathrm{d}\beta}{\mathrm{d}\omega}\right|_{\omega=\omega_0} = \frac{1}{v_g}. \tag{1.12}$$

The second-order term β_2 represents the group velocity dispersion (GVD) parameter, related to the total dispersion parameter D_{total} by $D = -\frac{2\pi c}{\lambda^2}\beta_2$ [69]:

$$\beta_2 = \left.\frac{\mathrm{d}^2\beta}{\mathrm{d}\omega^2}\right|_{\omega=\omega_0}. \tag{1.13}$$

From a wave-dynamics perspective, dispersion regimes are categorized by how the group velocity changes with optical frequency ($\mathrm{d}v_g/\mathrm{d}\omega$). In the normal dispersion regime ($\beta_2 > 0$, $D < 0$), group velocity decreases with frequency ($\mathrm{d}v_g/\mathrm{d}\omega < 0$), causing lower frequencies to travel faster than higher

frequencies [69]. Conversely, in the anomalous dispersion regime ($\beta_2 < 0$, $D > 0$), group velocity increases with frequency ($\mathrm{d}v_g/\mathrm{d}\omega > 0$), allowing higher frequencies to travel faster than lower frequencies [69]. Higher-order terms ($\beta_2, \beta_3, \dots$) induce a wave-vector offset across interacting optical frequencies, generating the linear phase mismatch term ($\Delta k_{\text{dispersion}}$) [69]. Achieving precise control over dispersion is essential for compensating temporal pulse broadening, achieving nonlinear phase-matching, and maintaining stable microresonator comb states in integrated photonic devices [69], [70].

1.4 Nonlinear Optics

Nonlinear optics is the study of changes in the optical properties of a material induced by the presence of intense light [71]. The electric field associated with such light exerts a force on the electron cloud surrounding the atoms of the medium, causing it to deform and become polarized.

Optical nonlinearity originates from the non-proportional relationship between the polarization of a material and the applied electromagnetic field strength. When an electromagnetic wave interacts with a medium, it induces a dipole moment per unit volume, known as the electric polarization $\mathbf{P}$. This total polarization can be expanded as a power series in the electric field strength $\mathbf{E}$ [71]:

$$\mathbf{P} = \varepsilon_0 \left(\chi^{(1)}\mathbf{E} + \chi^{(2)}\mathbf{E}^2 + \chi^{(3)}\mathbf{E}^3 + \dots \right) = \mathbf{P}^{(1)} + \mathbf{P}^{(2)} + \mathbf{P}^{(3)} + \dots,$$

where ε_0 is the permittivity of free space, and the coefficients $\chi^{(1)}$, $\chi^{(2)}$, and $\chi^{(3)}$ represent the n-th order optical susceptibility tensors, with higher-order terms following accordingly.

These susceptibility terms serve as fundamental material response parameters that quantify the magnitude, polarizability, and spatial symmetry dependence of the medium's bound charges under an applied optical field [71]. Under weak optical illumination, the polarization response of a dielectric medium is governed predominantly by the linear susceptibility $\chi^{(1)}$. This parameter dictates the linear polarizability of atomic bound charges in the

harmonic regime, directly defining intrinsic linear optical properties such as the linear refractive index n and the optical absorption coefficient [71].

As the applied optical field strength increases, the bound electron clouds are driven into an anharmonic displacement regime, causing higher-order nonlinear susceptibility terms to become significant [69]. The second-order nonlinear susceptibility $\chi^{(2)}$ acts as a material response parameter quantifying the leading-order quadratic anharmonicity. Because quadratic polarization requires an asymmetric potential well, $\chi^{(2)}$ is non-zero exclusively in non-centrosymmetric media (materials lacking structural inversion symmetry) [71]. This term governs second-order three-wave mixing processes, including second-harmonic generation (SHG), sum-frequency generation (SFG), and difference-frequency generation (DFG).

In contrast, the third-order nonlinear susceptibility $\chi^{(3)}$ quantifies the cubic anharmonic response of the bound electron displacement. Unlike $\chi^{(2)}$, the cubic parameter $\chi^{(3)}$ is present in media regardless of crystal symmetry [69], [71]. It serves as the primary material response parameter governing the Kerr effect, self-phase modulation (SPM), and four-wave mixing (FWM) which are relevant for frequency comb generation in microring resonators. This will be discussed in the following sections.

1.4.1 Second-Harmonics Generation

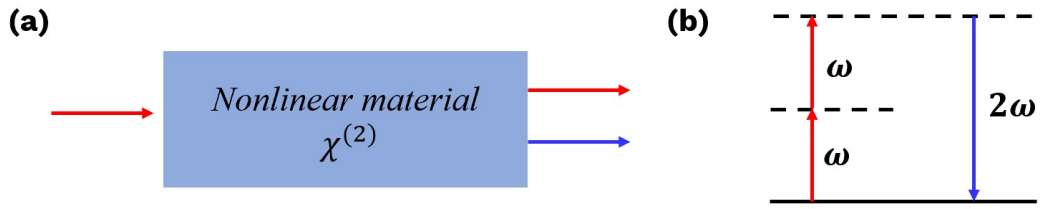


FIGURE 1.9: (a) Schematic of principle of SHG (b) Energy-level diagram describing SHG. Doted line represents virtual energy states. Solid line represents atomic ground state. [71].

Second-harmonic generation (SHG) is a fundamental second-order ($\chi^{(2)}$) nonlinear optical process where two photons of frequency ω combine in a non-centrosymmetric medium to generate a single photon at 2ω, as depicted in

Figure 1.9 (a) and (b). Within the electric-dipole approximation, bulk SHG is strictly forbidden in centrosymmetric materials—such as silicon, silica (SiO_2), and alumina (Al_2O_3)—because their crystal structures possess spatial inversion symmetry, forcing the second-order nonlinear susceptibility to vanish ($\chi^{(2)} = 0$). In contrast, non-centrosymmetric zinc-blende III–V semiconductors—including GaAs, InP, and InGaAsP—possess strong intrinsic second-order susceptibilities.

While the primary experimental scope of this thesis focuses on third-order ($\chi^{(3)}$) nonlinear photonics in III–V-OI platforms, developing high-index-contrast III–V-OI waveguides concurrently establishes the structural and material foundation required for second-order nonlinear interactions. Combining the high optical confinement of the III–V-OI architecture with the intrinsic material non-centrosymmetry of III–V layers lays the groundwork for on-chip second-harmonic generation which are outlined as future research directions in the conclusions of this thesis.

1.4.2 Kerr Effect

The optical Kerr effect describes the intensity-dependent refractive index of a material arising from the third-order nonlinear susceptibility $\chi^{(3)}$. In this regime, the refractive index can be written as

$$n = n_0 + n_2 I, \tag{1.14}$$

where n_0 is the linear refractive index, n_2 is the nonlinear refractive index coefficient, and I is the optical intensity. The nonlinear refractive index is related to the real part of the third-order susceptibility by

$$n_2 = \frac{3\,\mathrm{Re}(\chi^{(3)})}{4n_0^2\varepsilon_0 c}. \tag{1.15}$$

Materials in which the refractive index depends on the optical intensity in this manner are referred to as Kerr media. This Kerr nonlinearity provides the fundamental physical basis for several nonlinear optical processes, including self-phase modulation and four-wave mixing, which are discussed in

the subsequent sections. In particular, in resonant structures such as micro-ring resonators, the strong enhancement of the intracavity field significantly amplifies Kerr interactions, enabling efficient parametric processes that ultimately lead to optical frequency comb generation, as detailed in the following section.

1.4.3 Self Phase Modulation

Self-phase modulation (SPM) is a single-beam nonlinear process where an optical field modulates its own phase during propagation through a Kerr medium [71]. As light travels through a medium of length L (or effective length L_{eff}), an optical field given by

$$E(t,z) = A(t,z)e^{i(\omega_0 t - k_0 z)} \tag{1.16}$$

experiences a total intensity-dependent phase shift $\phi(t,z)$ defined as

$$\phi(t,z) = k_0 nz = k_0(n_0 + n_2 I(t))z = \phi_0(z) + \phi_{\text{NL}}(t,z), \tag{1.17}$$

where the vacuum wavenumber k_0 is expressed as

$$k_0 = \frac{2\pi}{\lambda_0}, \tag{1.18}$$

the linear phase shift $\phi_0(z)$ is given by

$$\phi_0(z) = k_0 n_0 z, \tag{1.19}$$

and ϕ_{NL} represents the SPM-induced nonlinear phase shift

$$\phi_{\text{NL}}(t,z) = k_0 n_2 I(t) z = \gamma P(t) z. \tag{1.20}$$

Here, $P(t)$ is the optical power profile of the pulse, and $\gamma = k_0 n_2 / A_{\text{eff}}$ is the waveguide nonlinear parameter, where A_{eff} is the effective mode area.

A time-varying intensity profile $I(t)$ leads to a time-dependent phase shift, which induces a shift in the instantaneous optical frequency $\delta\omega(t)$ across the

pulse, defined as

$$\delta\omega(t) = -\frac{\partial\phi_{\mathrm{NL}}(t,z)}{\partial t} = -k_0 n_2 z \frac{\partial I(t)}{\partial t}. \tag{1.21}$$

This time-dependent frequency shift creates a chirp across the optical field: on the leading edge ($\partial I/\partial t > 0$), $\delta\omega(t) < 0$, resulting in a red-shift (shift toward lower frequencies), whereas on the trailing edge ($\partial I/\partial t < 0$), $\delta\omega(t) > 0$, resulting in a blue-shift (shift toward higher frequencies). Therefore,the resulting optical field leaving the Kerr medium after experiencing SPM-induced phase modulation is given in the time domain by

$$E(t,L) = A(t,0)\exp(i\left[\omega_0 t - \phi_{\mathrm{NL}}(t,L)\right]). \tag{1.22}$$

To determine the processed optical spectrum $S(\omega, L)$, the output field is transformed into the frequency domain via a Fourier transform

$$\begin{aligned} S(\omega,L) &= \left|\mathcal{F}\left\{A(t,0)e^{-i\phi_{\mathrm{NL}}(t,L)}\right\}\right|^2 \\ &= \left|\int_{-\infty}^{\infty} A(t,0)e^{-i\phi_{\mathrm{NL}}(t,L)}e^{-i(\omega-\omega_0)t}\,dt\right|^2. \end{aligned} \tag{1.23}$$

As the pulse propagates, it experiences a time-varying frequency chirp across its temporal profile. Because identical instantaneous frequency shifts $\delta\omega(t)$ occur at two distinct points within the pulse profile—one on the leading edge and one on the trailing edge—these two temporal components interfere either constructively or destructively depending on their relative phase difference.

Consequently, the processed spectra in Figure 1.10 (a)–(d) display characteristic multi-peaked oscillations and progressive spectral broadening as the maximum nonlinear phase shift increases from $\phi_{\max} = 0.5\pi$ to 3.5π. For lower values such as $\phi_{\max} = 0.5\pi$ as shown in Figure 1.10 (a), the spectrum broadens smoothly. As $\phi_{\max}$ increases to 1.5π, 2.5π, and 3.5π shown in Figure 1.10 (b)-(d), clear interference fringes emerge, increasing the peak count N according to

$$N \approx \frac{\phi_{\max}}{\pi}. \tag{1.24}$$

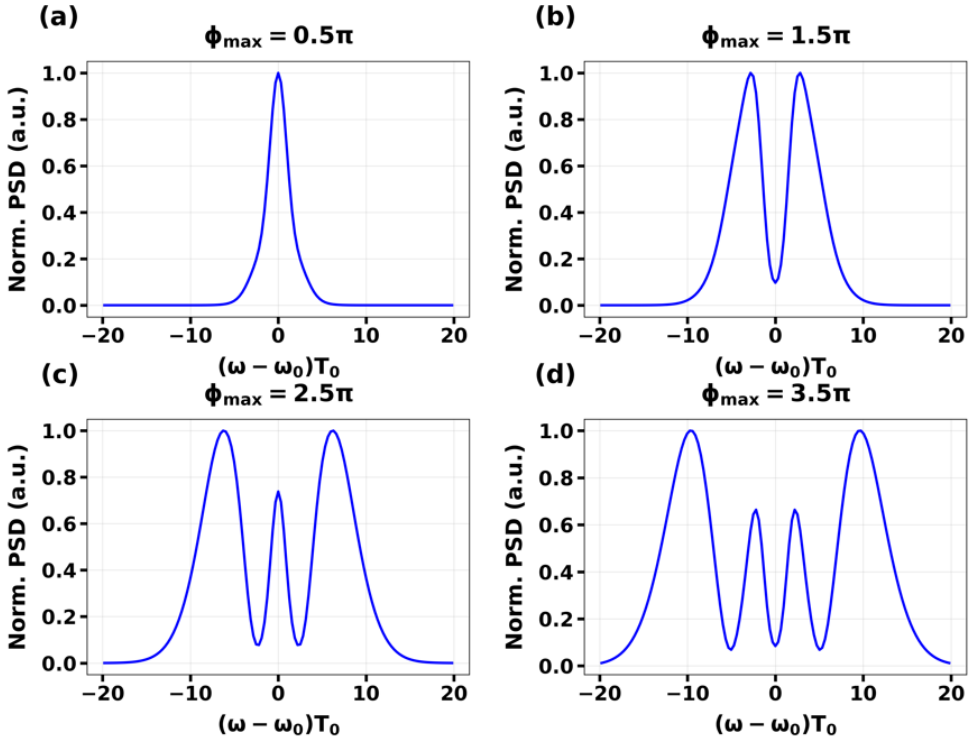


FIGURE 1.10: Calculated normalized power spectral density (PSD) of a Gaussian pulse undergoing SPM for maximum nonlinear phase shifts of (a) $\phi_{\max} = 0.5\pi$, (b) $\phi_{\max} = 1.5\pi$, (c) $\phi_{\max} = 2.5\pi$, and (d) $\phi_{\max} = 3.5\pi$. As $\phi_{\max}$ increases, spectral broadening and multi-peak oscillations develop due to intensity-dependent phase modulation.

In resonant structures like microring resonators and optical fibers, this SPM-induced spectral broadening serves as a core mechanism for all-optical switching, supercontinuum generation, and temporal soliton formation [69], [72], [73], [74]. Specifically, for frequency comb generation in micro-rings, the SPM-induced phase chirp must be balanced by anomalous group-velocity dispersion ($\beta_2 < 0$), while the pump laser is red-detuned relative to the cavity resonance. This combined balance of dispersion, Kerr nonlinearity, and detuning compensates for cavity loss and stabilizes circulating pulses into bright Kerr Solitons [72]. An analysis of Kerr soliton formation in InGaAsP-OI microring resonators is presented in Chapter 3.

1.4.4 Four-Wave Mixing

Four-Wave Mixing (FWM) is a nonlinear process governed by the third-order nonlinear susceptibility $\chi^{(3)}$, wherein four optical waves exchange power through the Kerr nonlinearity of the waveguide medium [69]. Depending on the number of distinct pump frequencies involved, parametric wave mixing occurs in either a degenerate or non-degenerate regime [75] as shown in Figure 1.11.

In degenerate FWM shown in Figure 1.11 (a), the foundational mechanism for optical wavelength conversion and single-pump parametric amplification—two pump photons from a single optical field at frequency ω_p are annihilated to simultaneously generate a frequency-downshifted signal photon at ω_s and a frequency-upshifted idler photon at ω_i [75]. Energy conservation for the degenerate process requires that

$$2\omega_p = \omega_s + \omega_i. \tag{1.25}$$

In non-degenerate FWM shown in Figure 1.11 (b), the process involves two distinct pump waves at frequencies ω_{p1} and ω_{p2}. One photon from each pump wave is annihilated ($\omega_{p1} + \omega_{p2}$) to generate a signal photon (ω_s) and an idler photon (ω_i) [69]. Energy conservation for the non-degenerate process dictates

$$\omega_{p1} + \omega_{p2} = \omega_s + \omega_i. \tag{1.26}$$

For efficient energy transfer from the pump waves to the generated sidebands over a propagation length L, the interacting waves must maintain phase coherence [76]. The local propagation phase mismatch Δk accounts for both linear chromatic dispersion ($\Delta\beta_{\text{linear}}$) and intensity-dependent nonlinear phase shifts ($\Delta k_{\text{nonlinear}}$) [76]. For degenerate FWM, this phase mismatch is expressed as [69]

$$\Delta k = \Delta\beta_{\text{linear}} + \Delta k_{\text{nonlinear}} \approx \beta_2(\omega_s - \omega_p)^2 + 2\gamma P_p, \tag{1.27}$$

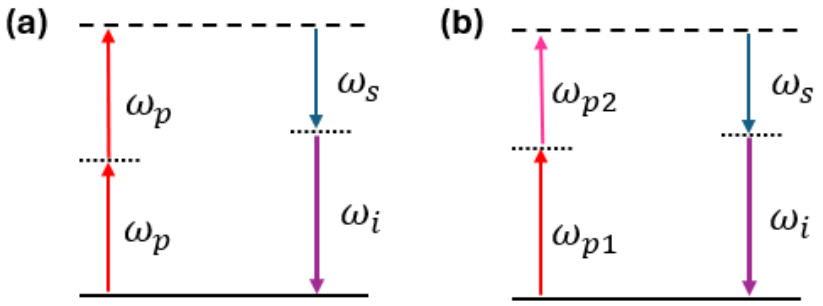


FIGURE 1.11: Energy level diagram illustrating (a) degenerate Four-Wave Mixing, where two pump photons ($\hbar\omega_p$) generate a signal ($\hbar\omega_s$) and idler ($\hbar\omega_i$) photon pair, and (b) non-degenerate Four-Wave Mixing involving two distinct pump frequencies ($\hbar\omega_{p1}, \hbar\omega_{p2}$).

where β_2 represents the group velocity dispersion (GVD) parameter evaluated at the pump frequency, P_p is the peak pump power, and γ is the waveguide nonlinear parameter. The parameter γ quantifies the strength of nonlinear interactions per unit power and length within the waveguide cross-section, defined as [69]

$$\gamma = \frac{2\pi n_2}{\lambda_0 A_{\text{eff}}} = \frac{\omega_0 n_2}{c A_{\text{eff}}}, \tag{1.28}$$

Here, A_{eff} mathematically accounts for the spatial intensity distribution of guided transverse electromagnetic modes, such as the fundamental (TE_{00}, TM_{00}) or higher-order (TE_{01}, TM_{01}) spatial modes illustrated in Figure 1.2—across the waveguide cross-section (x, y). For a complex spatial electric field profile $E(x, y)$, the effective mode area is formally defined via spatial self-overlap integrals as [69]

$$A_{\text{eff}} = \frac{\left(\iint_{-\infty}^{\infty} |E(x,y)|^2 \, dx \, dy\right)^2}{\iint_{-\infty}^{\infty} |E(x,y)|^4 \, dx \, dy}. \tag{1.29}$$

This equation captures how optical power density is spatially distributed across the high-index core and the surrounding cladding layers. Operationally, A_{eff} serves as the bridge between total guided optical power P and peak spatial intensity $I(x, y) \approx P/A_{\text{eff}}$. Smaller effective mode areas concentrate energy into a tighter spatial volume, resulting in higher local optical field intensities that directly scale the γ and enhance Kerr-mediated phase shifts. In practice, analytical calculation of Equation (1.29) is often intractable

for complex or asymmetric dielectric waveguide profiles. This is because the complex cross-sectional boundaries prevent closed-form mathematical solutions for the electric field. Consequently, numerical mode solvers using Finite Difference Eigenmode (FDE, Ansys Lumerical Mode) algorithms or Finite Element Methods (FEM, COMSOL Multiphysics) are used to extract A_{eff} directly from the solved vector fields. In Chapter 2, these numerical techniques are utilized to calculate A_{eff} and quantify spatial mode confinement in InGaAsP strip-loaded waveguides. In Chapter 3, A_{eff} is computed for microring resonators to evaluate γ and model Four-Wave Mixing dynamics.

The term $2\gamma P_p$ in Equation (1.27) arises directly from Self-Phase Modulation (SPM) on the pump and Cross-Phase Modulation (XPM) exerted by the pump onto the generated sidebands [69]. For non-degenerate FWM with total pump power $P_{\text{total}} = P_1 + P_2$, the phase mismatch expands to include mutual XPM between the two pump fields [69], [76]:

$$\Delta k_{\text{non-deg}} \approx \beta_2(\omega_s - \omega_{p1})(\omega_s - \omega_{p2}) + 2\gamma P_{\text{total}}. \tag{1.30}$$

In both operational regimes, achieving exact phase matching ($\Delta k \approx 0$) requires the linear dispersion term in Equation (1.27) or Equation (1.30) to be negative to offset the positive Kerr-induced phase shift ($2\gamma P$), making the anomalous dispersion regime ($\beta_2 < 0$) essential for efficient parametric conversion in Kerr media with $n_2 > 0$ [75]. In the next section, we will discuss how FWM drives optical frequency comb generation within microring resonators.

1.5 Microring Resonators and Frequency Comb Generation

A microring resonator is a foundational composite building block in photonic integrated circuits that plays a crucial role in on-chip optical signal processing and data transmission [77]. As illustrated in Figure 1.12 (a), in its simplest add-through configuration, a microring resonator consists of a straight bus waveguide evanescently coupled to a closed-loop circular waveguide of radius r and perimeter $L = 2\pi r$, separated by a narrow coupling gap.

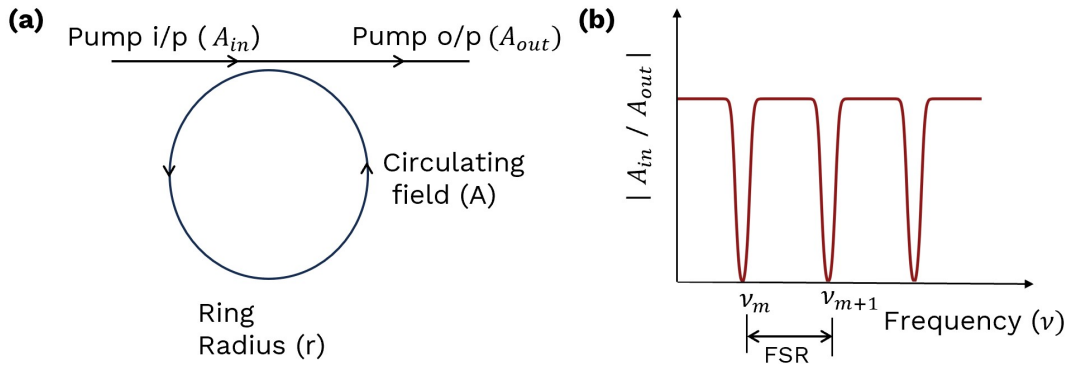


FIGURE 1.12: Schematic representation of (a) an add-through microring resonator (b) the optical transmission spectrum of a microring resonator. Destructive interference produces periodic resonance dips at frequencies ν_m and ν_{m+1} separated by the Free Spectral Range (FSR).

Light from an input pump field A_{in} propagating along the bus waveguide couples into the ring cavity across the directional coupling region with power transmission coupling coefficient θ. As light circulates around the closed loop of length L, it accumulates a round-trip optical phase shift given by

$$\phi = \beta L = \frac{2\pi n_{\text{eff}}}{\lambda} L. \tag{1.31}$$

Constructive interference occurs when the round-trip phase accumulated by the circulating field is an integer multiple of 2π

$$\phi = 2\pi m \implies m\lambda_m = n_{\text{eff}} L \quad (m \in \mathbb{N}), \tag{1.32}$$

Here, m represents the azimuthal mode number, and λ_m denotes the corresponding resonance wavelength. At these resonant angular frequencies given by

$$\omega_{\text{res}} = \frac{2\pi c}{\lambda_m}. \tag{1.33}$$

Power builds up inside the cavity, resulting in sharp dips in the output transmission spectrum due to destructive interference between the uncoupled input field and the cavity leakage field. As depicted in Figure 1.12 (b), the frequency separation between two adjacent longitudinal cavity modes (m and $m+1$) defines the FSR. Differentiating the resonance condition with respect

to frequency yields the round-trip time t_R and corresponding FSR as

$$t_R = \frac{Ln_g}{c} = \frac{L}{v_g}; \tag{1.34}$$

$$\text{FSR}_\nu = \Delta\nu = \nu_{m+1} - \nu_m \approx \frac{1}{t_R} = \frac{c}{n_g L} = \frac{c}{2\pi r\, n_g}, \tag{1.35}$$

where n_g is the group refractive index accounting for waveguide and material dispersion given by

$$n_g = n_{\text{eff}} + \omega \frac{dn_{\text{eff}}}{d\omega}. \tag{1.36}$$

As shown in Figure 1.12 (b), the FSR directly sets the repeating spectral cavity grid that governs nonlinear wave interactions inside the resonator. Building upon this resonant framework, frequency comb generation arises from the third-order nonlinear susceptibility tensor $\chi^{(3)}$ in resonators with high Kerr nonlinearity, providing a compact source for Wavelength Division Multiplexing (WDM) systems and energy-efficient optical interconnects [78]. As illustrated in Figure 1.13 (a), when a material with strong Kerr nonlinearity - such as InGaAsP or AlGaAs - is pumped by a CW laser field A_{in} at angular frequency ω_l tuned near the central resonant mode ω_0 with phase detuning [79]

$$\delta_0 = (\omega_l - \omega_0) t_R, \tag{1.37}$$

high intra-cavity power densities build up. Once the intra-cavity threshold power is reached, degenerate FWM is initiated.

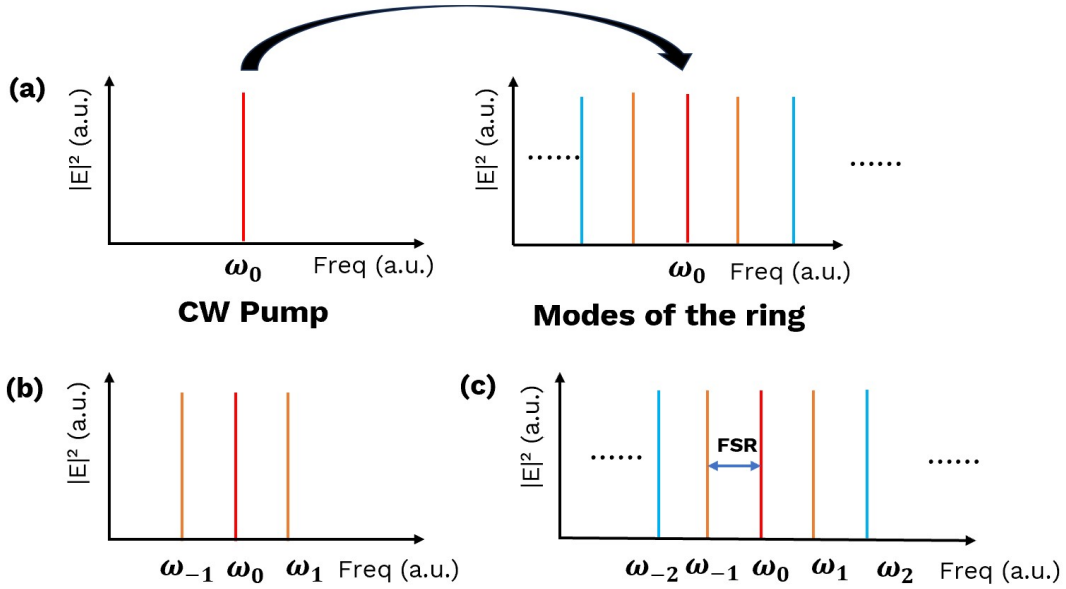


FIGURE 1.13: Principle of frequency comb generation: (a) pump mode overlapping with resonant mode of the ring; (b) degenerate FWM; (c) Cascaded FWM with FSR spacing indicated.

This process annihilates two pump photons to generate a pair of signal and idler sidebands at frequencies ω_1 and ω_{-1} symmetrically positioned around the pump mode ω_0, as shown in Figure 1.13 (b). This is given by

$$2\omega_0 = \omega_1 + \omega_{-1}. \tag{1.38}$$

Because the cavity field is strongly enhanced at the underlying mode grid, these newly generated sidebands align with adjacent cavity modes separated by integer multiples of the resonator FSR ($\omega_1 - \omega_0 \approx 2\pi \times \text{FSR}$). As intracavity power grows, these primary sidebands act as secondary pumps, driving non-degenerate (cascaded) FWM processes given by

$$\omega_0 + \omega_1 = \omega_2 + \omega_{-1}; \tag{1.39}$$

$$\omega_0 + \omega_{-1} = \omega_{-2} + \omega_1. \tag{1.40}$$

Through this cascaded nonlinear interaction, a broad family of discrete, equally spaced spectral lines is generated, forming an optical frequency comb where

the comb line spacing is fundamentally dictated by the cavity FSR, as depicted in Figure 1.13 (c) [79].

For efficient energy transfer and coherent comb buildup across multiple round trips, phase matching must be maintained [71], [80]. The net round-trip phase mismatch Δk_{total} is given by [81]

$$\Delta k_{\text{total}} = \Delta k_{\text{dispersion}} + \Delta k_{\text{nonlinear}} \approx 0. \tag{1.41}$$

Here, $\Delta k_{\text{dispersion}}$ accounts for linear group velocity dispersion through the second-order dispersion coefficient β_2, while $\Delta k_{\text{nonlinear}}$ is given by

$$\Delta k_{\text{nonlinear}} = 2\gamma |A|^2. \tag{1.42}$$

Here, $|A|^2$ represents inter-cavity optical power. Consequently, $\Delta k_{\text{nonlinear}}$ captures Kerr-induced phase shifts from Self-Phase Modulation (SPM) and Cross-Phase Modulation (XPM). In positive Kerr coefficient materials ($n_2 > 0$) such as InGaAsP operating in the C-band, $\Delta k_{\text{nonlinear}}$ is positive [28]. Consequently, achieving $\Delta k_{\text{total}} \approx 0$ requires engineered anomalous chromatic dispersion ($\beta_2 < 0$) in the waveguide cross-section to provide a compensating negative phase shift, as detailed in Chapter 3.

1.6 Development of III-V-OI Platforms

The development of the III–V-OI platforms begins with wafer bonding a III–V wafer to a Silicon wafer that has a SiO_2 top layer, as illustrated in Figure 1.14. After the bonding, the III–V substrate and the etch-stop layer are removed from the bonded III-V wafer in order to expose the III-V guiding layer. The following section discusses wafer bonding and layer removal techniques including fundamental principles and the basic mechanisms involved.

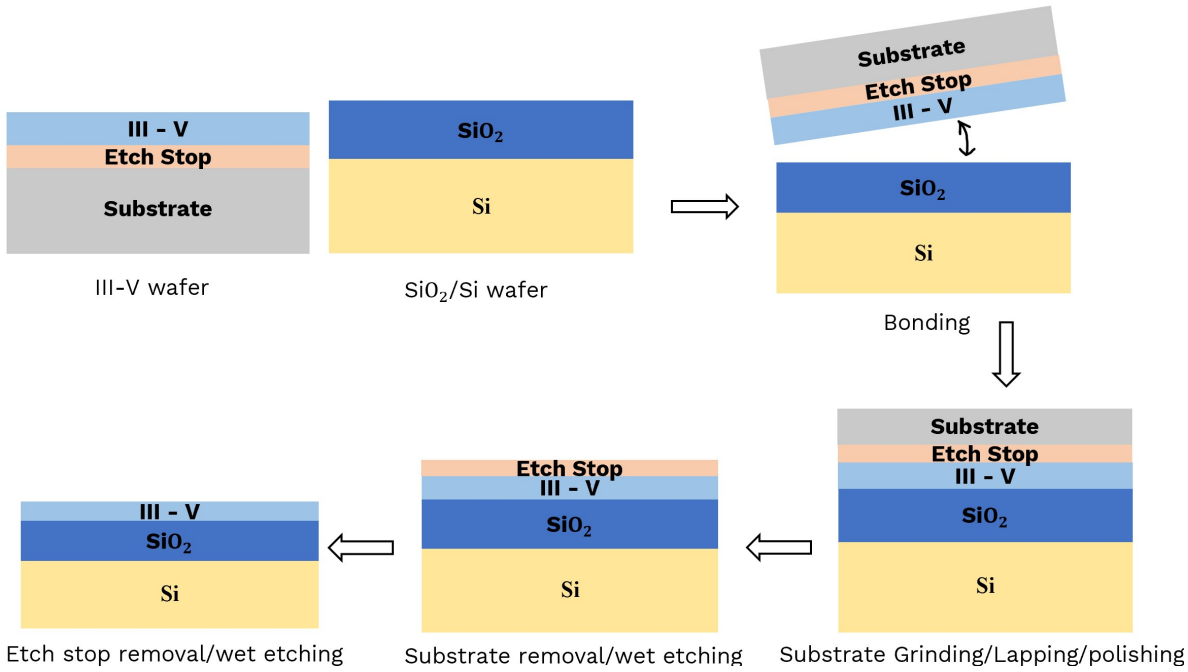


FIGURE 1.14: Steps involved in developing III-V-OI platform.

1.6.1 Wafer bonding

Bonding is a layer transfer technology that was first explored in 1986 for semiconductors to realize the silicon-on-insulator (SOI) platform [82]. Nearly four decades after this initial demonstration, bonding continues to be a critical technique in the fabrication of 3D integrated circuits, microelectronics, microelectromechanical systems (MEMS), and heterogeneous integration [83], [84], [85], [86]. Two bonding methods have been extensively studied in III-V-OI research: direct bonding and adhesive bonding. Direct bonding involves bringing two mirror-like, ultra-smooth wafer surfaces into close contact without any intermediate layer as illustrated in Figure 1.15 (a) [87]. This proximity enables the formation of chemical bonds at the interface, effectively joining the wafers into a single unit. It is also referred to as Van der Waals bonding, because the initial bonding arises from Van der Waals forces between surface molecules [88]. Fundamentally, these forces represent short-range physical attractions driven by temporary or permanent dipole interactions between neighboring atoms. These forces can evolve into permanent bonds under optimized bonding conditions, which may include precise control of applied force , temperature, bonding duration, and surface activation

via plasma or wet chemical treatments, or a combination of these techniques [89], [90], [91], [92], [93]. For Van der Waals forces to act effectively, the distance between molecules on the two surfaces being bonded must be between 0.3 nm and 0.5 nm [94]. For this reason, mirror-like, ultra-smooth surfaces are a fundamental requirement for direct bonding. A typical workflow of direct bonding includes wafer surface polishing, cleaning and surface preparation, room-temperature alignment and contact of the wafers under applied force, followed by annealing to enhance bond strength [95].

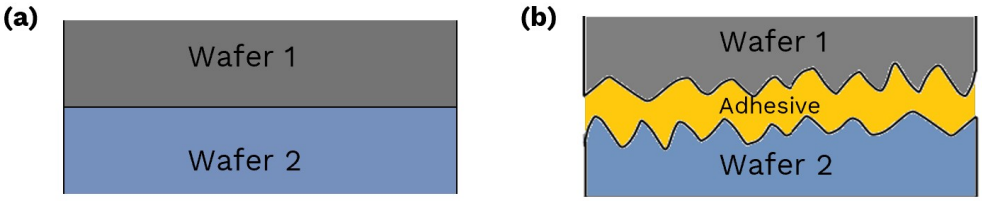


FIGURE 1.15: Different categories of bonding methods for III-V-OI (a) Direct wafer bonding (b) Adhesive bonding

In contrast, adhesive wafer bonding uses an intermediate adhesive layer to join the two wafers as shown in Figure 1.15 (b). Typically, a flowable polymer or epoxy is applied one or both of the wafer surfaces [96]. This adhesive layer fills the microscopic valleys on the surfaces and smooths out surface roughness. As a result, adhesive bonding can tolerate surface roughness up to some extend compared to direct bonding [97].

Besides being tolerant to surface roughness, adhesive bonding offers several additional advantages. It requires relatively low bonding temperatures, provides resilience against stress and mechanical vibrations, and ensures uniform load distribution over a large area—benefits made possible by advances in polymer chemistry [96].

Once the wafer surfaces are brought together and aligned, pressure is applied to ensure intimate interfacial contact during adhesive bonding [98]. The polymer adhesive is then transformed from a flowable state into a solid state, typically through heat exposure. During this curing process, the adhesive must harden into a material capable of withstanding the forces required

to keep the surfaces bonded [98]. Polymer adhesives with low viscosity and minimal shrinkage during thermal treatment generally result in strong and reliable bonds [94]. In the context of this work, both direct and adhesive bonding techniques are explored to develop III-V-OI platforms. Specifically, we investigate direct bonding between SiO_2 layers deposited via plasma-enhanced chemical vapor deposition (PECVD) and thermal oxidation, as well as adhesive bonding using an alumina (Al_2O_3) interlayer and Medusa in Chapter 4.

1.6.2 Substrate thinning or removal

Substrate thinning methods for III-V-OI platforms typically begin with mechanical material removal from the substrate, followed by wet chemical etching or polishing when the remaining substrate thickness reaches a few tens of microns. The initial mechanical techniques enable coarse thinning, whereas subsequent chemical or polishing processes provide fine thinning.

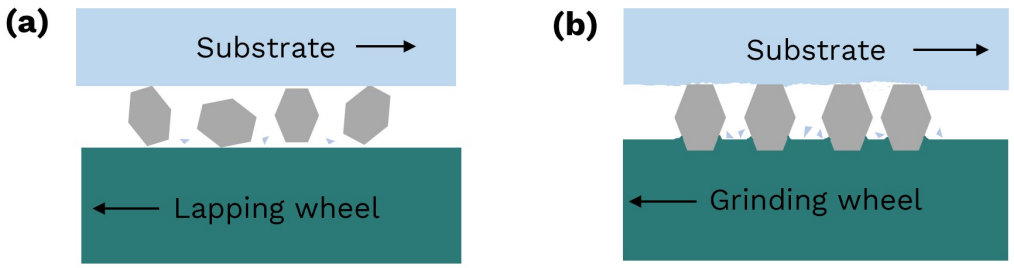


FIGURE 1.16: Substrate thinning process using (a) lapping (b) grinding. The abrasive grains are are shown in gray with the chips generated from the mechanical removal of substrate material.

Mechanical techniques for substrate thinning include lapping and grinding, both of which use abrasive grains for material removal [56]. A schematic illustration of lapping and grinding is shown in Figure 1.16. During lapping, the abrasive grains are free to roll between the sample surface and the lapping wheel, as shown in Figure 1.16 (a). In this thesis, grinding is used, where abrasive particles are embedded within a grinding wheel as shown

in Figure 1.16 (b). Although lapping is relatively gentle on the substrate, its material removal rate is slower than that of grinding [99]. Therefore, it is well suited for the final stages of grinding, where surface roughness is more critical than the rate of material removal [99], [100].

For fine thinning, polishing is typically used, employing much finer abrasive particles with grain sizes as low as 0.12 μm, compared to the larger grain sizes used in grinding or lapping, which can range from a few micrometers to several tens of micrometers [101], [102]. Polishing operates on a similar material removal principle as grinding or lapping but achieves higher surface smoothness due to the smaller abrasive size used [103].

Another fine substrate thinning approach is wet chemical etching, where chemical solutions are used to selectively remove or further thin the substrate material. For InP removal, hydrochloric acid (HCl)-based solutions are commonly used, while for GaAs removal, a citric acid ($C_6H_8O_7$) and hydrogen peroxide (H_2O_2) solution is widely popular [26], [58]. In this thesis, wet chemical etching is used for fine substrate thinning to develop the III-V-OI platform.

Overall, three critical factors determine the success of III-V-OI platform development using these thinning methods. The first is the presence of a suitable etch stop layer that is chemically inert to the wet etching solution used during substrate thinning [58]. The second is strong bonding strength between the III-V and insulator layer, which ensures mechanical stability during grinding or lapping. Third, resistance of the bonding material to chemical attack during wet thinning processes (in the case of adhesive bonding) [104]. To achieve the mechanical thinning of substrate in this thesis, grinding was carried out using diamond films with embedded diamond abrasive particles. A two-step thinning process was employed, utilizing films with grit sizes of 3 μm and 1 μm to progressively thin the substrate.

1.7 Fabrication of III-V Photonic Components

Fabrication of high-performance photonic components for Photonic Integrated Circuits (PICs) relies on nanofabrication technology. The conceptual foundation of this technology was laid by Richard Feynman in 1959 in his famous

lecture, "There's Plenty of Room at the Bottom" [105]. In this talk, he envisioned the possibility of manipulating matter at the nanoscale—an idea that has since been realized through modern semiconductor fabrication techniques. Over the past six decades since Faymann's lecture, nanofabrication has evolved significantly in the silicon semiconductor industry while also driving extensive research and development in III–V semiconductor nanofabrication [106], [107].

In photonics, a key advantage of nanofabrication is the ability to realize devices with at least one characteristic dimension smaller than the wavelength of the light under consideration. Structures engineered at this subwavelength scale enable precise control over light propagation and light–matter interactions, thereby enabling advanced on-chip photonic functionalities in III–V semiconductors, such as nonlinear frequency conversion and all-optical signal processing among others [71], [108]. In addition, nanofabrication facilitates the development of compact and complex photonic integrated circuits with lower power consumption [109], [110]. In this thesis, the nanofabrication process used for the realization of III–V photonic components consists of two main steps: patterning and etching. Pattern definition is carried out using electron-beam (e-beam) lithography, followed by plasma etching to transfer the patterns into the III-V layer.

1.7.1 Electron Beam Lithography

Electron Beam Lithography (EBL) is a maskless patterning method that uses a focused electron beam to selectively expose a radiation-sensitive polymer layer on a substrate, thereby defining features in the polymer layer [111].

Among various nanofabrication lithography techniques—such as extreme UV lithography, focused ion beam, plasmonic lithography, nanoimprint lithography, and EBL—the latter stands out, offering the highest resolution, down to just a few nanometers [112]. Such high resolution of electron beam (E-beam) lithography arises from the extremely small wavelength of electrons compared to that of photons. The wavelength of an electron is given by

$$\lambda = \frac{h}{\sqrt{2meV}}, \tag{1.43}$$

where $h = 6.62 \times 10^{-34}$ J $\cdot$ s is Planck's constant, m is the electron mass, e is the electron charge, and V is the acceleration voltage of the electron.

For example, in a typical low-voltage EBL system, such as a 10 kV system, Equation (1.43) predicts a wavelength of approximately 7 pm. However, the practically achievable minimum feature size is not at the picometer scale, nor can the resolution be increased indefinitely by increasing the acceleration voltage. Practical limitations arise from factors such as:

- Proximity effects;
- The finite size of resist molecules;
- Noise and instability in the beam positioning system.

These effects limit the achievable minimum feature size to the nanometer scale, well above the theoretically possible picometer scale. The proximity effect is discussed in detail in the following section of this chapter.

Principle of Operation

A general schematic of EBL is illustrated in Figure 1.17. It consists of an electron gun assembly that generates high-energy electrons directed down a column. Electron guns are categorized into two types based on how the electrons are produced: thermionic electron guns and field emission electron guns [113]. The condenser lenses control the beam by either expanding or narrowing it, thereby adjusting both the beam diameter and current. Deflection coils allow the electron beam to be scanned in both horizontal and vertical axes across the sample surface. The objective lens serves as the final focusing element, adjusting the focal length (or working distance) to ensure the beam is precisely focused on the sample.

The sample is placed on a stage equipped with a mechanical drive that offers high positional accuracy, minimal drift, and rapid movement. The stage and deflection coils operate together within a position control system to enable highly precise pattern writing using electron beam lithography.

The entire system is enclosed within a vacuum chamber to ensure that the electrons have a long mean free path. This allows them to travel in a ballistic regime, where their trajectories remain predictable without significant scattering before reaching the sample [114].

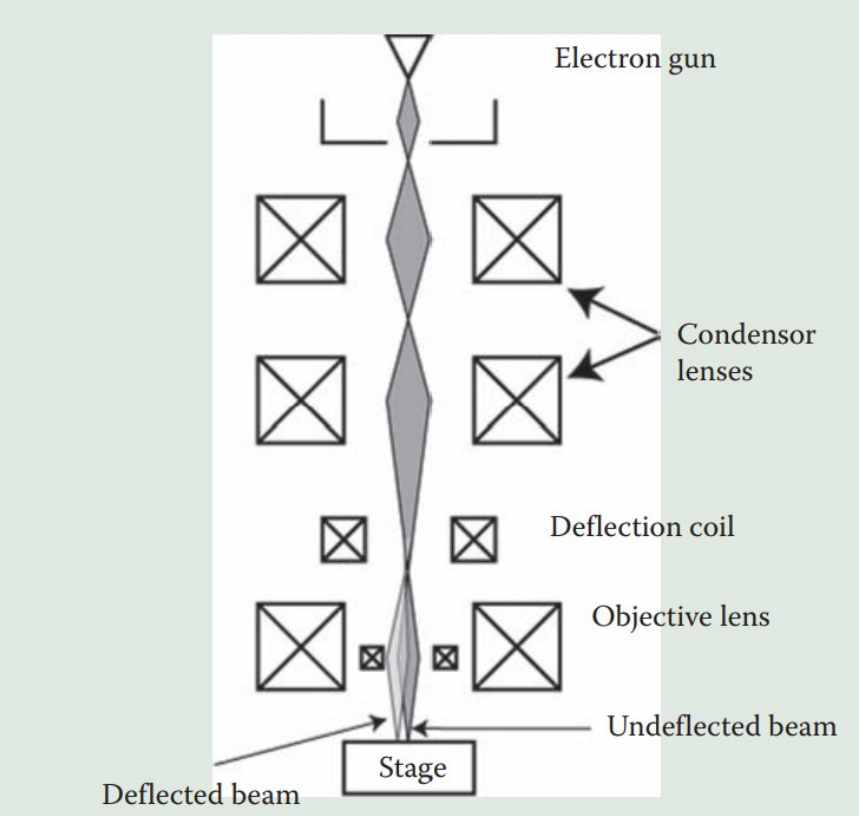


FIGURE 1.17: A schematic layout of an electron beam lithography tool [115].

The EBL process involves several steps: surface preparation, resist coating, e-beam exposure, and development, as illustrated in the Figure 1.18. Surface preparation typically involves sonication of the substrate in acetone, isopropyl alcohol (IPA), and deionized (DI) water, followed by drying with a nitrogen (N_2) blow. However, based on the chemistry of the resist, additional steps to EBL such as adhesion layer coating prior to spin-coating of resist and baking before and/or after spin coating may be required. After surface preparation, an electron-beam resist is deposited onto the clean and flat sample surface. In this work, the resist layer was coated using the spin-coating

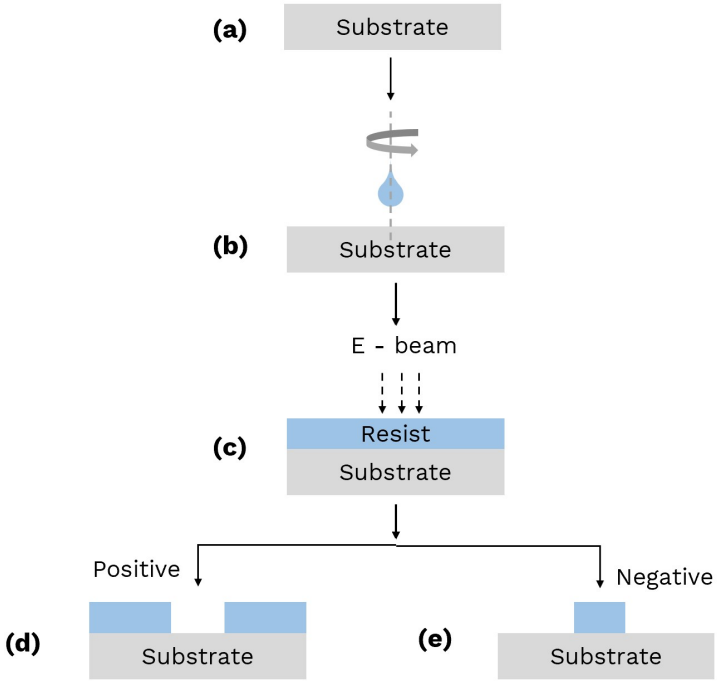


FIGURE 1.18: Steps in E beam lithography: (a) Surface preparation; (b) Spin-coating the resist; (c) E-beam exposure, and (d) Resist development.

technique, as shown in Figure 1.18 (a),(b), which allows the formation of a uniform thin film of resist on the substrate.

Next, the resist layer is exposed to the electron beam, as illustrated in Figure 1.18 (c), to write the desired pattern onto the resist. Finally, the sample is immersed in a suitable liquid developer, where the soluble portion of the resist is dissolved, leaving behind the patterned resist structure, as shown in Figures 1.18 (d) and (e).

E-beam Resist

E-beam resists are polymers that are sensitive to exposure by an electron beam. They are called "resists" because they protect selected areas of the sample surface during later fabrication steps, such as etching.

There are two main categories of e-beam resists: positive and negative. A

positive e-beam resist consists of long polymer chains that break when exposed to the electron beam. During the development step, the exposed regions become soluble in a suitable chemical developer and are removed, as shown in Figure 1.18 (d). A good example of positive tone resist is Poly Methyl Methacrylate (PMMA). Chapter 5 provides a detailed discussion on EBL using PMMA resist for the fabrication of metasurfaces.

In contrast, a negative e-beam resist contains polymers that crosslink to form longer polymer chain when exposed to the electron beam. This crosslinking hardens the exposed regions, making them resistant to the developer. As a result, the unexposed areas are dissolved and removed during development, leaving the exposed polymer behind, as illustrated in Figure 1.18 (e). Hydrogen Silsesquioxane (HSQ) is an example of a negative-tone e-beam resist. Chapter 2 discusses in detail the fabrication of waveguides using HSQ as the e-beam resist in EBL. It also discusses the bonding of the sample using Medusa—a negative e-beam resist and a variant of HSQ—as an adhesion layer to develop the III–V-OI platform.

Proximity Effect

Proximity effect in lithography refers to how features written close to one another influence each other's exposure conditions. In electron beam lithography, this occurs primarily due to electron scattering within the resist, while in photolithography it arises from wave diffraction and the resulting interference [116].

In EBL specifically, these interactions include forward scattering within the resist and backscattering from the underlying substrate coated with resist. Owen, et al. provide one of the most effective schematic illustrations of this proximity effect [117].

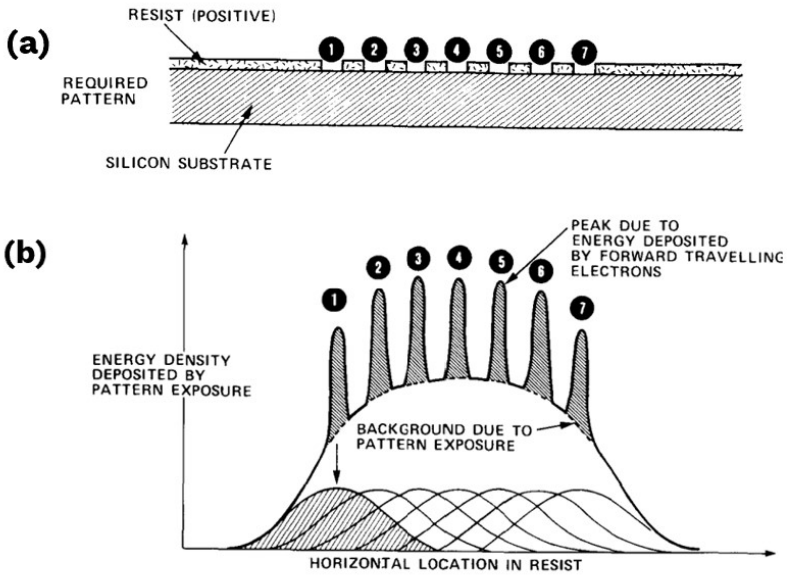


FIGURE 1.19: Schematic illustration of (a) the cross-section of the e-beam patterned sample after development, and (b) the corresponding energy density deposited in the e-beam resist, shown as a function of horizontal position within the resist [117]

.

Figure 1.22 (a) shows a cross-section of an electron-beam lithography patterned sample after development. The sample consists of a silicon substrate with lines defined in a positive e-beam resist layer on top. Prior to exposure, all lines have identical geometrical dimensions, equal spacing, and are subjected to same exposure dose.

Figure 1.22 (b) illustrates the resulting energy density deposited in the resist as a function of horizontal position in the resist. The contribution from forward-traveling electrons is represented by the seven shaded spikes labeled 1–7. In contrast, the energy deposited by backscattered electrons is shown as seven Gaussian-like curves along the horizontal axis. As seen in the Figure 1.22 (b), the backscattered electron distributions from adjacent lines overlap. Consequently, each written line experiences a different overall energy density distribution (indicated by thick black line). Upon development, this leads to variations in the resist dissolution rates at the seven line positions, causing the lines to develop with different widths. This effect is known

as the proximity effect. This situation is undesirable, as it can lead to discrepancies between the designed device dimensions and the fabricated structure, and limit the achievable resolution to tens or hundreds of nanometers—far from the theoretically attainable picometer-scale resolution. Therefore, it is important to perform proximity effect correction.

Proximity Effect Correction

Proximity Effect Correction (PEC) in EBL was first introduced in 1979 [118]. This first error-correction strategy involve the calculation of an adjusted exposure value in different regions based on a proximity function that models electron scattering events in the resist. Following this initial dose-based correction method, several computational models have been developed over the years [119]. Proximity-effect correction methods can be broadly classified into four categories: dose correction, background exposure correction, multi-layer resist usage, and modification of pattern shape [117].

Dose correction

Instead of exposing every pixel in a feature with the same dose, the dose-modulation method calculates the exposure energy for each pixel individually and adjusts the dose accordingly. This calculation is influenced by several factors, such as the distance between the centers of pixels that need to be exposed [120].

Although several algorithms exist, many of them focus on calculating a point spread function (PSF), which describes how the exposure energy from a single electron beam spot spreads to the surrounding area [120]. Such algorithms have been implemented in many modern EBL systems. However, when the circuit to be written is large, these proximity effect correction (PEC) methods require significant computational time and memory.

Background exposure correction

Background exposure correction is another form of dose correction used in EBL. Tools such as GHOST and PowerProx are commonly employed for this method [121], [122]. Though they generally rely on simplified algorithms

that mainly address the proximity effect (PE) caused by backscattered electrons from the substrate, while often neglecting forward scattering within the resist.

In the GHOST method, the sample is exposed twice [123]. The first exposure is the pattern exposure, which defines the intended feature geometry. The second exposure—known as the ghost or correction exposure—writes the inverse of the pattern with a dose that is adjusted according to the background energy distribution calculated from the initial pattern exposure. The goal is to maintain a uniform total energy distribution across the pattern so that all features develop uniformly in the developer solution after EBL, regardless of whether the features are dense or isolated. Alternatively, PowerProx accounts for background exposure in the primary dose, thereby eliminating the need for a second exposure [122].

Multi-layer Resist usage

In this technique, an intermediate layer made of either a polymer or a metal is introduced between the substrate and the top e-beam resist layer [124]. The purpose of this intermediate layer is to absorb or reflect backscattered electrons originating from the substrate, preventing them from reaching the top imaging resist layer. However, this approach can complicate the fabrication process [117]. For example, in nanofabrication processes that require multilayer lithography steps, fiducial marks are often used as reference points to align the electron beam with previously written patterns. These marks are typically detected through backscattered electrons. When a multilayer resist technique is used to reduce the proximity effect, detecting these fiducial marks becomes difficult or even impossible.

Shape Correction

In this category of PEC the shapes in the pattern layout are adjusted so that the developed image aligns as closely as possible with the intended design [125]. In the shape modification technique, these adjustments are typically implemented using computational algorithms, such as Monte Carlo simulations [126]. Software tools like BEAMER [127] and PYRAMID [128] apply

these methods to resize the edges of features by calculating the energy distribution resulting from electron scattering events. A similar approach is used in Chapter 5 of this thesis for the fabrication of metasurface.

1.7.2 Plasma Etching

The etching process is a crucial step in the nanofabrication of photonic integrated circuits. It is a subtractive process in which excess material surrounding the desired features is removed, allowing the pattern from the resist to be transferred onto the underlying substrate. In photonic component or circuit fabrication, two primary etching approaches are commonly used. The first is wet etching, where a liquid etchant chemically converts the unwanted material into a soluble product that dissolves in the liquid. The second is plasma etching, in which a gaseous etchant in a plasma converts the excess material into a volatile product that can be removed. For nanofabrication, plasma etching is generally preferred over wet etching because it can achieve anisotropic etch profiles and excellent etch selectivity between the substrate and resist —capabilities that wet etching cannot provide.

In this thesis, we focus on the plasma etching of InGaAsP/InP using a widely adopted plasma etching system, the RIE-ICP (Reactive Ion Etch–Inductively Coupled Plasma) etcher. Compared to other plasma etching tools, such as RIE or Electron Cyclotron Resonance (ECR) etchers, the RIE-ICP system offers greater versatility for III-V semiconductors because it can generate a stable, high-density plasma at low pressure while independently controlling ion flux and energy—capabilities that are essential for achieving both high etch rates and anisotropic profiles.

Plasma is essentially an ionized gas containing electrons, ions, radicals, molecules, and photons. In an RIE-ICP etcher, a radio-frequency (RF) generator operating at 13.56 MHz excites electrons in the reaction chamber, causing collisions with etchant molecules and atoms that produce plasma. Additionally, an ICP coil integrated into the chamber and powered by a separate RF source generates a magnetic field that further stimulates electron collisions, increasing the density of charged particles and radicals. This enhances plasma stability

even at low pressures. Typical reactions in a plasma is given are the following

$$\begin{aligned}
\text{Ionization:} \quad & e^- + XY \rightarrow 2e^- + XY^+ \\
\text{Excitation:} \quad & e^- + XY \rightarrow e^- + XY^* \rightarrow e^- + XY + h\nu \\
\text{Dissociation:} \quad & e^- + XY \rightarrow e^- + X + Y \\
\text{Attachment:} \quad & e^- + XY \rightarrow XY^- \\
\text{Dissociative recombination:} \quad & e^- + XY^+ \rightarrow X + Y^* \\
\text{Electron detachment:} \quad & e^- + XY^- \rightarrow 2e^- + XY
\end{aligned}$$

Here XY represents an arbitary etchent molecule or compound in the plasma and XY^* or Y^* represents reactive radicals generated in the plasma.

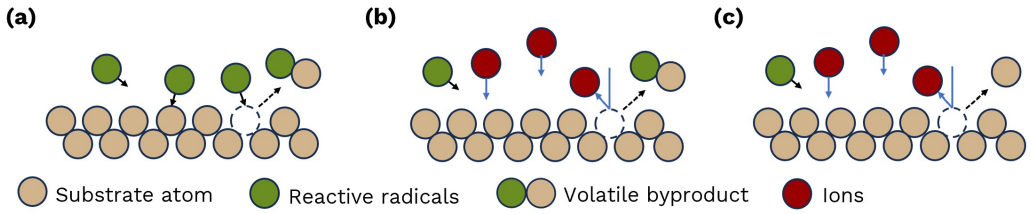


FIGURE 1.20: Schematic representation of the mechanisms involved in plasma etching: (a) chemical etching, (b) Ion-assisted chemical etching, (c) physical etching [129].

During plasma etching, three dominant mechanisms are typically observed: chemical etching, ion-assisted chemical etching, and physical etching, as depicted in Figure 1.20 (a), (b) and, (c), respectively [130]. Chemical etching occurs when reactive radicals in the plasma chemically react with the substrate, producing byproducts, as shown in Figure 1.20 (a). This process is generally isotropic, taking place uniformly in all directions. Ion-assisted chemical etching involves ion bombardment, which helps remove reaction byproducts-including non-volatile ones and can break covalent bonds to generate additional volatile subproducts, as depicted in Figure 1.20 (b). Physical etching relies on energetic ions, typically argon ions, to physically sputter the substrate by breaking bonds and amorphizing the surface, as shown in Figure 1.20(c). The ions are accelerated vertically by the plasma sheath electric field, making physical etching highly anisotropic. Physical etching can also assist in byproduct desorption. Optimizing the etching recipe to achieve

vertical sidewalls, high selectivity, and an adequate etch rate is critical for fabricating photonic waveguides, as discussed in Chapter 2. This optimization requires a careful balance of chemical and physical etching mechanisms, which is achieved by adjusting RIE (bias) power, ICP power, chamber pressure, gas flow rate to the chamber and, in some cases, substrate temperature. In Chapter 2, we present the RIE-ICP etching of InGaAsP/InP with a chlorine-based plasma chemistry.

1.8 Metasurface Fabrication and PEC

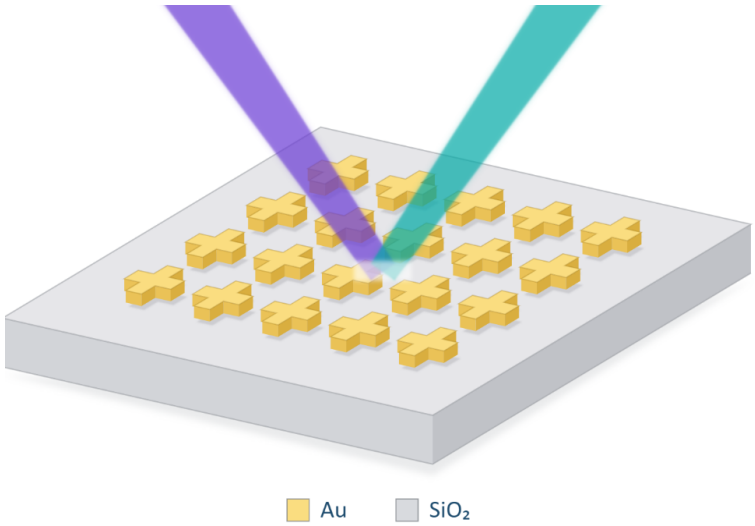


FIGURE 1.21: Schematic of a plasmonic metasurface consisting of cross-shaped gold (Au) meta-molecules on a SiO_2 substrate, illustrating nonlinear frequency conversion from an incident pump beam (violet) to a generated output beam (teal) [131].

Metasurfaces represent two-dimensional arrangements of artificial structural units, termed meta-molecules, designed to manipulate electromagnetic waves at subwavelength scales [132]. Since the initial experimental demonstration of a "flat antenna" over two decades ago [133], the scientific community has made significant strides in achieving advanced electromagnetic control. A diverse array of meta-molecule geometries has been investigated, with the periodic array of cross-shaped gold antennas on silica (SiO_2) illustrated in Figure 1.21 serving as a representative example from the literature [131].

Key functionalities demonstrated using these platforms include optical cloaking [134], [135], beam steering [136], holography [137], and coherent-wave down-conversion [138]. Design methodologies for metasurfaces with these functionalities have seen rapid progress over the past few years with the integration of deep learning [139]. In contrast, experimental demonstrations have lagged behind, largely due to the limited accessibility to high-performance fabrication equipment, which requires high monetary investments to acquire, maintain, and upgrade [140]. The flat antennae initially had lateral dimensions of a few microns and were fabricated using conventional optical lithography techniques [133]. However, following their initial demonstration, researchers began investigating antennae with reduced lateral dimensions, on the order of several tens of nanometers [112]. These studies revealed that scaling down to smaller sizes offers improved control over electromagnetic waves at desired wavelength ranges.

Building on our earlier discussion of nanofabrication techniques, EBL offers the highest resolution among competing methods like extreme UV, focused ion beam, plasmonic, and nanoimprint lithography, achieving features down to a few nanometers [112]. However, one key factor that limits the resolution of EBL is the proximity effect [141]. This limitation was recognized well before the first experimental demonstration of metasurfaces but gained renewed attention following that breakthrough [142], [143], [144], [145]. The proximity effect is more pronounced in lower kV EBL systems because lower-energy electrons undergo stronger forward scattering and result in a larger beam spot size inside the resist [146]. Although lower-kV systems offer lower resolution and higher proximity effects, they are more widely available than higher-kV systems due to their considerably lower costs and operation and maintenance simplicity [147].

In chapter 5 of this thesis, a shape modification method of PEC that is not computationally intensive is discussed, making it suitable for use with low kV e-beam system, particularly in environments where access to high-performance computing resources is limited. Chapter 5 will present the work flow of fabrication of gold metasurface on glass starting from spin coating of resist, followed by EBL, evaporation of gold and lift off of excess gold. Additionally, the chapter outlines the full fabrication workflow for gold metasurfaces on

glass, spanning resist spin coating, EBL patterning, evaporation, and final metal lift-off.

1.9 InGaAsP Nonlinear Optical Characterization: Pump-Probe Measurement

The pump–probe technique is an all-optical method that has been widely employed in semiconductor research since the 1990s to study carrier generation, dynamics, and recombination [71], [148]. In photonic devices, it has been extensively used to investigate a variety of phenomena, including decay dynamics [149], sub-bandgap absorption [150], optical gain [151], [152], exciton dissociation [153], and surface or interface recombination velocity [154], [155], among others.

The operating principle of pump–probe measurements relies on a high-energy pump pulse that excites the process of interest within the device, followed by a time-delayed, lower-energy probe pulse that monitors its temporal evolution [156]. This technique is particularly well suited for measuring the free-carrier (FC) lifetime of carriers generated through two-photon absorption (TPA), as it enables the study of carrier dynamics over a broad range of timescales [156].

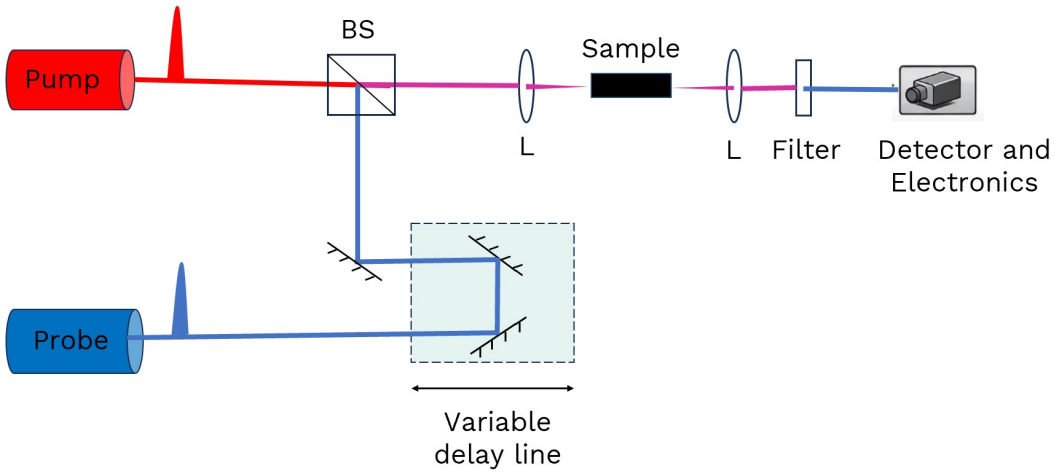


FIGURE 1.22: A general schematic of pump probe technique for free carrier lifetime measurement.

A standard experimental configuration for measuring FC lifetime using the pump–probe technique is shown in Figure 1.22. The setup includes a pulsed pump beam to excite the carrier dynamics in the sample and a delay line in the probe arm to introduce a controllable temporal delay between the pump and probe pulses. By varying this delay, the transmission or reflection of the probe can be measured at different times following excitation, providing insight into the temporal evolution of the carrier dynamics [157].

In this configuration, the pump and probe beams are spatially overlapped using a beam splitter and focused onto the sample with a lens. A second lens collects the transmitted signal, which is then passed through a filter to remove the pump contribution before detection. With a fast and precise tunable delay line, this conventional arrangement enables temporal resolution in the femtosecond to picosecond range [158].

Despite its effectiveness in FC lifetime measurement, practical implementation of the pump–probe technique shown in Figure 1.22 can be challenging, because it requires precise optical alignment of mirrors in the delay line and may suffer from mechanical instability due to moving components in the delay line as we measure FC lifetime as a function of time delay (Δt) [56]. Depending on the required temporal resolution and signal quality, various modifications to this basic setup can be implemented [71], [159], [160].

In Chapter 2, an alternative pump–probe configuration is used, employing a CW probe without a delay line in the probe arm to measure the FC lifetime in an InGaAsP/InP strip waveguide. In this approach, a fast detection system is used to achieve the temporal resolution necessary for FC lifetime measurements in nanosecond scale.

1.10 Thesis Outline and Contributions

This thesis is organized into five interconnected chapters that systematically address the challenges of nonlinear loss, material platform integration, and

advanced nanofabrication for next-generation integrated photonics. Chapter 1 introduces the physical principles and historical motivation for integrated photonics, highlighting the key trade-offs between silicon and direct-bandgap III-V semiconductors. It establishes the foundational material properties of the quaternary alloy InGaAsP and outlines the rationale for transitioning from native InP substrates to high-confinement InGaAsP-OI architectures for nonlinear optical processing.

Chapter 2 builds upon these foundational material considerations by experimentally investigating free-carrier absorption (FCA) and recombination dynamics in InGaAsP/InP strip-loaded waveguides. It details the nanofabrication process of the measured waveguides, presents a non-degenerate pump-probe experimental methodology used to extract the free-carrier lifetime, and analyzes the resulting carrier dynamics. The chapter concludes by demonstrating that InGaAsP suffers from severe two-photon absorption (TPA) followed by persistent free-carrier effects, providing the core physical rationale for carrier lifetime management when transitioning to high-intensity InGaAsP-OI platforms.

Chapter 3 focuses on the numerical modeling of microring resonators on the high-confinement InGaAsP-OI platform, evaluating the specific influence of nonlinear losses on optical frequency comb generation. Crucially, these simulations incorporate the empirical free-carrier lifetimes extracted from the pump-probe experiment in Chapter 2, directly linking empirical recombination dynamics to cavity modeling. The modeling demonstrates that optical microcomb generation remains achievable despite TPA and free-carrier effects through strategic carrier lifetime engineering. This key finding confirms the feasibility of the nonlinear-loss-limited microcomb approach and directly motivates the development of heterogeneous integration techniques for InGaAsP-OI.

Chapter 4 addresses the material platform development, exploring adhesive bonding, direct wafer bonding, and substrate removal methodologies employed in the realization of III-V-OI architectures. This work specifically focuses on InGaAsP-OI and AlGaAs-OI platforms, establishing quantitative characterizations of bonding quality, interface bond strength, and process limitations necessary for scalable photonic integration.

Finally, Chapter 5 presents an additional nanofabrication contribution by detailing a shape-modification-based proximity effect correction (PEC) technique developed for metasurface fabrication using a low-kV electron-beam lithography system. The methodology is validated through experimental implementation on high-density sub-wavelength dielectric metasurfaces, expanding the nanofabrication capabilities required for complex nanophotonic structures.

The main original contributions of this thesis encompass both fundamental physical characterizations and practical technological developments in integrated photonics. First, this work provides the experimental extraction and physical analysis of free-carrier lifetimes and dynamics in InGaAsP/InP waveguides via pump-probe spectroscopy. Second, it delivers the numerical study on frequency comb generation in InGaAsP-OI microring resonators operating under significant nonlinear loss. Third, it establishes the process development, bonding quality evaluation, substrate removal protocols, and challenges for direct and adhesive wafer bonding of InGaAsP-OI and AlGaAs-OI material systems. Fourth, it presents a validated, shape-modification-based proximity effect correction technique optimized for low-kV electron-beam lithography of sub-wavelength metasurfaces.

Collectively, these contributions advance the study of nonlinear integrated photonics and nanophotonics by clarifying the impact of TPA and FCA in bandgap-limited, high-index-contrast III-V semiconductor platform and establishing advanced nanofabrication pathways. By unifying empirical carrier lifetime measurements, frequency comb modeling, wafer bonding process evaluations, and low-kV proximity effect corrections for plasmonic metasurfaces, this work establishes the fundamental physical baseline and nanofabrication framework required for advanced photonic devices. Crucially, by identifying the specific interface mechanisms that restrict wafer bonding yields, this thesis establishes a clear technological roadmap for future realization of high-confinement III-V-OI photonic integrated circuits.

Chapter 2

Free-Carrier Lifetime Measurement of InGaAsP/InP Waveguide

In recent past, our research group fabricated and characterized three layer heterostructure $In_{0.86}Ga_{0.14}As_{0.30}P_{0.70}$/InP waveguides of different geometries and explored their nonlinear optical performances [28], [29]. This work revealed strong TPA at an operating wavelength of 1550 nm, yielding a TPA coefficient of 19 cm/GW [29]. However, while these measurements established the magnitude of the nonlinearity, a complete understanding of the material's nonlinear dynamics requires investigating carrier decay in the time domain.

This chapter reports, to the best of our knowledge, the first experimental measurement of the free-carrier (FC) lifetime in $In_{0.86}Ga_{0.14}As_{0.30}P_{0.70}$/InP at the telecommunication wavelength of 1550 nm. The FC lifetime was measured using a non-degenerate pump-probe spectroscopy technique, in which the pump and probe operate at different wavelengths. To enable these measurements, strip-loaded waveguides (see section 1.2 for the waveguide geometry description) were fabricated using hydrogen silsesquioxane (HSQ) as the etch mask. I performed fabrication of the waveguides, data analysis and experimental characterization. The ICP-RIE etch recipe discovery for InGaAsP was developed through valuable discussions with Dr. Kashif Awan, a PhD graduate from our research group. The FC lifetime experiments were conducted under the supervision of Dr. Gabriel Flizikowski, a postdoctoral researcher in our research group. I would also like to acknowledge Prof.

Nathalie Vermeulen for the valuable discussions through out the experimental and analytical stages of this work. We begin by examining the underlying mechanisms of Two-Photon Absorption (TPA) and Free-Carrier Absorption (FCA) in direct-bandgap semiconductors.

2.1 Two Photon Absorption and Free Carrier Absorption

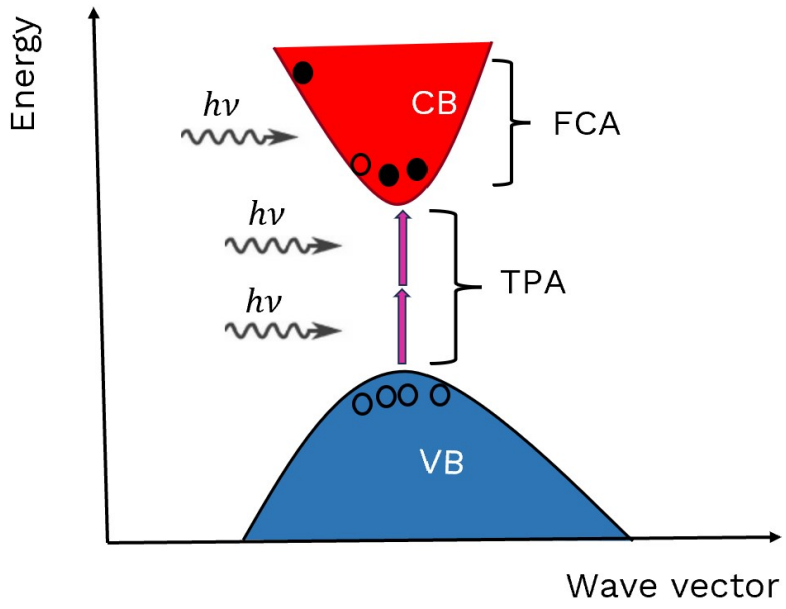


FIGURE 2.1: An illustration of TPA and associated FCA in direct band gap materials.

Figure 2.1 illustrates the process of TPA in a direct bandgap semiconductor. In this process, electrons are excited from the valence band to the conduction band through the simultaneous absorption of two photons. This occurs when the photon energy is lower than the bandgap energy but greater than or comparable to half of the bandgap [71]. Such conditions explained before are met in materials like InGaAsP and silicon at the 1550 nm (C-band) operating wavelength [28], [161]. The carriers generated via TPA initially occupy states near the bottom of the conduction band, where they can subsequently absorb photons through free-carrier absorption (FCA) as shown in Figure 2.1. The average time that carriers remain in these states before undergoing FCA

is defined as the free-carrier lifetime. TPA and FCA are undesirable nonlinear effects because they introduce intensity-dependent absorption that depletes optical power and reduces the efficiency of useful nonlinear interactions. In the following section we will discuss experimental measurement of FC lifetime in InGaAsP.

2.2 Free-Carrier Lifetime: Significance and State of the Art

Designing photonic integrated circuits on material platforms that exhibit TPA at the operating wavelength, such as silicon and InGaAsP in the C-band, requires careful consideration of TPA-induced FCA and free-carrier dispersion (FCD) [62], [161]. Collectively referred to as the free-carrier (FC) effect, FCA and FCD significantly influence the nonlinear dynamics of semiconductor waveguides. They reduce the efficiency of FWM [162], limit the achievable nonlinear phase shift in self-phase modulation [28], decrease parametric gain [163], and modify the refractive index [164], thereby degrading the performance of wavelength-sensitive nonlinear photonic devices. The influence of the FC effect on pulse propagation and nonlinear dynamics in silicon waveguides has also been investigated by Lefrançois et al [165].

A key parameter governing the FC dynamics is the free-carrier lifetime [166]. Defined as the average time that the carriers remain in the excited state after being generated through TPA, the FC lifetime directly determines the accumulation of free carriers and, consequently, the magnitude of FCA and FCD [167]. Our previous numerical study demonstrated the critical influence of the FC lifetime on frequency comb generation in the InGaAsP platform [62], emphasizing the importance of experimentally determining this parameter for accurate device modeling and optimization.

FC lifetimes reported in the literatures span several orders of magnitude depending on the material system, device geometry, and carrier extraction mechanism. The lifetime values as short as a few picoseconds have been reported in reverse-biased p-i-n diode-integrated silicon waveguides and ring resonators [168], [169], while lifetimes on the order of nanoseconds have been

measured in doped InP [162] and in silicon waveguides with modified fabrication processes [170], [171]. In bulk doped silicon, free-carrier lifetimes can extend into the microsecond regime [168]. Most of these values have been obtained directly using pump–probe spectroscopy, whereas others have been inferred through numerical modeling.

Despite the extensive body of work on FC lifetime measurements in silicon at telecommunications wavelengths, no corresponding measurements have previously been reported for InGaAsP. The experimental results presented in this chapter therefore establish the first reference values for the FC lifetime in this material platform. These measurements provide an essential baseline for the device modeling and lifetime engineering studies presented in Chapter 3.

2.3 Fabrication of Strip Loaded waveguides

A 600-nm-thick $In_{0.86}Ga_{0.14}As_{0.30}P_{0.70}$ core layer was grown on an approximately 340-μm-thick InP substrate, followed by the deposition of a 1 μm thick InP cladding layer. All epitaxial layers were fabricated using metal–organic chemical vapor deposition (MOCVD) at the Centre for Integrated Nanotechnologies (CINT), Sandia National Laboratories, USA, under a III–V semiconductor epitaxy grant.

The 2-inch InGaAsP/InP wafer was cleaved into smaller samples of approximately 1 cm × 1 cm for subsequent patterning. These samples were cleaned using a standard solvent cleaning process involving sequential immersion in acetone, isopropyl alcohol (IPA), and deionized (DI) water, each for 5 minutes with gentle sonication. Sample cleaning was conducted using an 80 kHz dual-frequency ultrasonic bath (Fisherbrand FB11201, 2.75 L maximum tank capacity) operated at 30 % effective power or 30 W of effective acoustic output. Due to the relatively brittle nature of InP compared to other III–V semiconductors such as AlGaAs or GaAs, care was taken to ensure that sonication remained mild to prevent sample damage. After cleaning, the samples were dried using nitrogen (N_2) blow-drying, followed by baking on a hotplate at 180 °C for 4 minutes to remove residual moisture.

A negative e-beam resist consisting of 10% hydrogen silsesquioxane (HSQ, Applied Quantum Materials Inc.) dissolved in methyl isobutyl ketone (MIBK) was used as e-beam resist for patterning. HSQ was selected for its excellent line edge roughness, high-resolution capability (down to 10 nm), and strong resistance to O_2 plasma, making it well-suited for metasurface and metawaveguide fabrication our group has been actively exploring. Additionally, HSQ provides sufficient etch resistance without requiring an intermediate hard mask, unlike resists such as ZEP. This motivated an investigation into the etch rate and selectivity of developed HSQ in $BCl_3/Cl_2/Ar$ - plasma for InGaAsP photonic device fabrication.

The resist was stored at room temperature and spin-coated at 5000 rpm with a 1-second ramp-up and 3-second ramp-down, resulting in an HSQ film thickness of approximately 315 nm, as measured by atomic force microscopy (AFM). Achieving a uniform coating required careful control of the delay between resist dispensing and spin initiation to minimize solvent evaporation and HSQ particle sedimentation. After spin coating, the sample was left in the spinner for 5 minutes to allow partial drying. Importantly, spin coating was performed within approximately one hour prior to EBL exposure to minimize premature crosslinking, as HSQ is highly sensitive to ambient moisture.

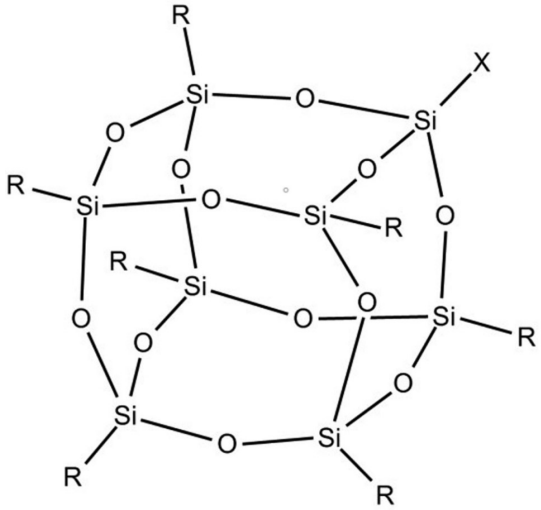


FIGURE 2.2: General chemical structure of HSQ. The labels R and X represent terminal substituent groups bound to the silicon-oxygen core, where R and X are Hydrogen atoms in HSQ prior to cross linking. [172].

Compared to conventional resists such as PMMA and ZEP, HSQ has a shorter shelf life. The reason for this lies in its chemical structure. A general structure of HSQ is shown in Figure 2.2. As an inorganic polymer with a Si–O–Si cage structure and reactive Si–H bonds, HSQ can undergo spontaneous crosslinking over time, leading to increased viscosity and eventual solidification. This change in viscosity was observed to affect adhesion to the InP substrate, resulting in pattern loss after development. Improved adhesion was achieved by applying an HMDS adhesion promoter prior to HSQ coating, which allowed partial recovery of the patterned features.

Patterning was carried out using 30 kV EBL (Raith PIONEER system), followed by development in aqueous tetramethylammonium hydroxide (TMAH, MF-24A) for 75 seconds. The pattern was then transferred into the underlying III–V layer using a $BCl_3/Cl_2/Ar$-based dry etching process in an ICP-RIE system (SAMCO 110iP). The ICP-RIE etch recipe for InGaAsP/InP was initially optimized in 2022 by Dr. Kaustubh Vyas, a former PhD student in our research group, using a 320 nm-thick PECVD-deposited silica hard mask. His optimized process served as the starting point for the dry etching performed in this work.

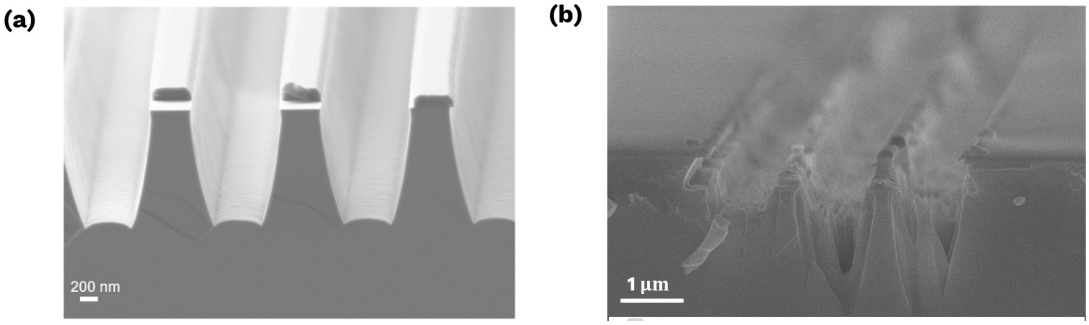


FIGURE 2.3: (a) InGaAsP/InP waveguides etched using the ICP-RIE recipe optimized in 2022, showing smooth sidewalls and good etch quality (b) InGaAsP/InP waveguides etched on the same RIE-ICP etcher in a later year by us in our first attempt using the same recipe, showing poor selectivity and needle-like microstructures.

The process began with a 1-hour chamber clean using a chlorine/argon plasma, followed by 15 minutes of chamber conditioning using the etch chemistry at room temperature and an additional 15 minutes of conditioning at a substrate temperature of 190 °C. The etching was then carried out using a gas mixture of Cl_2:BCl_3:Ar = 1:4:4, a chamber pressure of 0.15 Pa, an ICP power of 50 W, an RF power of 20 W, and a substrate temperature of 190 °C. Using the described parameters, Dr. Vyas accomplished etching with smooth sidewalls, as shown Figure 2.3 (a).

Although the same ICP-RIE system was used in this work, we anticipated that the previously optimized recipe might not produce identical results because the chamber had undergone numerous process changes over time. In particular, the chamber had been repeatedly switched between chlorine- and fluorine-based chemistry to accommodate the requirements of different users. Such changes can alter the chamber wall condition and seasoning, which are known to influence plasma characteristics and etch reproducibility.

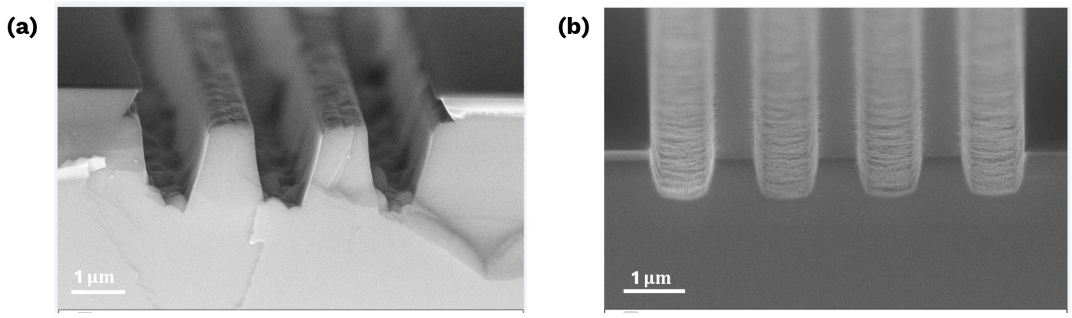


FIGURE 2.4: (a) Effect of increasing the chamber conditioning time from 15 min to 30 min, reducing the density of needle-like microstructures. (b) InGaAsP/InP waveguides fabricated with a chamber pressure of 0.45 Pa showing improvement in etch profile.

When the original recipe was applied under the current chamber conditions, the etch exhibited poor mask selectivity, and numerous needle-like microstructures were observed in the regions between adjacent waveguides, as shown in Figure 2.3 (b). To re-establish the chamber conditioning, the duration of the conditioning step was increased from 15 minutes to 30 minutes. As shown in Figure 2.4 (a), this significantly reduced the density of the needle-like features between the waveguides.

To further optimize the process, additional experiments were performed by increasing the chamber pressure. We hypothesized that excessive physical sputtering caused by energetic ion bombardment was contributing to the roughness and formation of microstructures in the etched regions. Increasing the chamber pressure reduced the ion energy reaching the sample surface, thereby improving the etch morphology. Figure 2.4 (b) shows the resulting waveguides etched at a chamber pressure of 0.45 Pa, where a noticeable reduction in roughness was achieved. The optimized etch conditions were subsequently used to fabricate the InGaAsP/InP devices using an HSQ mask.

Etching was performed at a chamber pressure of 0.45 Pa, bias power of 15 W, and ICP power of 50 W, with the substrate heated to 190 °C to enhance the volatility of etch by-products [173]. Under these conditions, an InP etch depth of 1 µm was achieved at an approximate etch rate of $4.2\,\mathrm{nm\,s^{-1}}$. The HSQ mask etched at roughly $1.3\,\mathrm{nm\,s^{-1}}$, yielding an etch selectivity of 3.2.

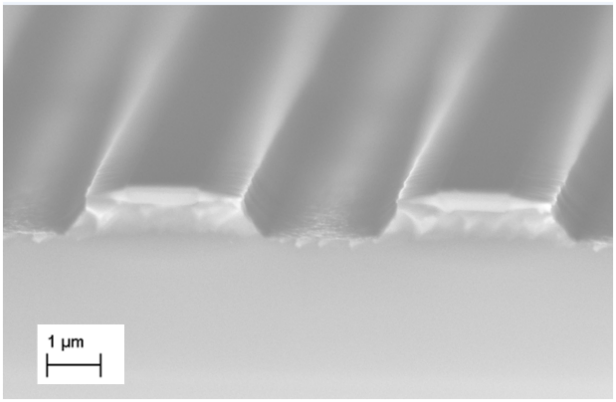


FIGURE 2.5: SEM images of the fabricated InGaAsP/InP strip loaded waveguide using HSQ mask.

Scanning electron microscope (SEM) images of the fabricated waveguides are shown in Figure 2.5. Figure 2.6 presents the normalized optical mode intensity profiles of the fabricated waveguide, illustrating both the fundamental transverse electric (TE) and transverse magnetic (TM) modes. The mode profiles were simulated using Lumerical MODE Solutions (version 2024 R1) [174]. Because the waveguide has a completely symmetric cladding structure (InP on both top and bottom) and the core dimensions are sufficiently large, the fundamental mode is strongly confined within the InGaAsP core. The boundary conditions and decay rates are identical in both top and bottom claddings, and because the vast majority of the optical power resides inside the uniform core, both TE_{00} and TM_{00} modes adopt a centered, quasi-Gaussian intensity profile with nearly identical spatial distributions as shown in Figure 2.6 (a) and (b).

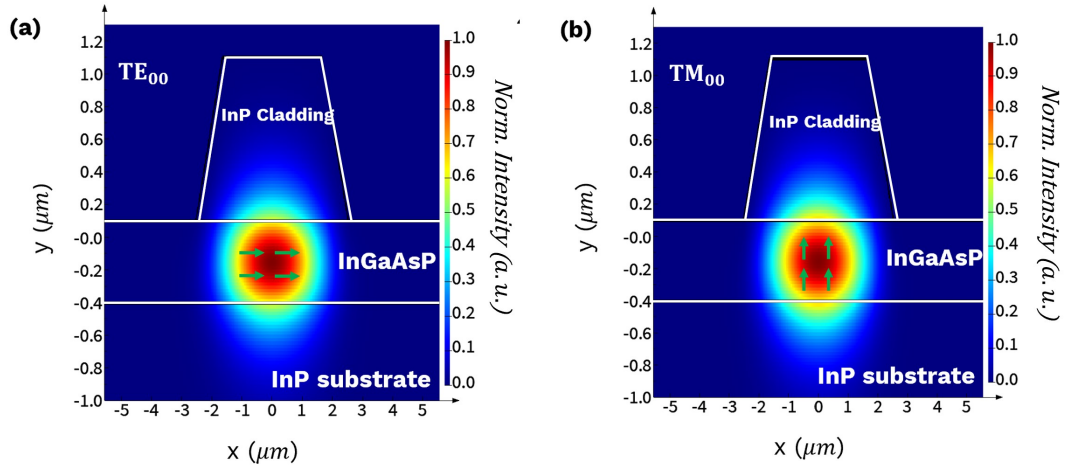


FIGURE 2.6: Simulated optical mode profiles of the fabricated waveguide with arrows showing direction of electric field vectors: (a) TE_{00} and (b) TM_{00} mode. The x and y axes indicate the transverse dimensions in micrometers.

2.4 Free-carrier Lifetime Measurement

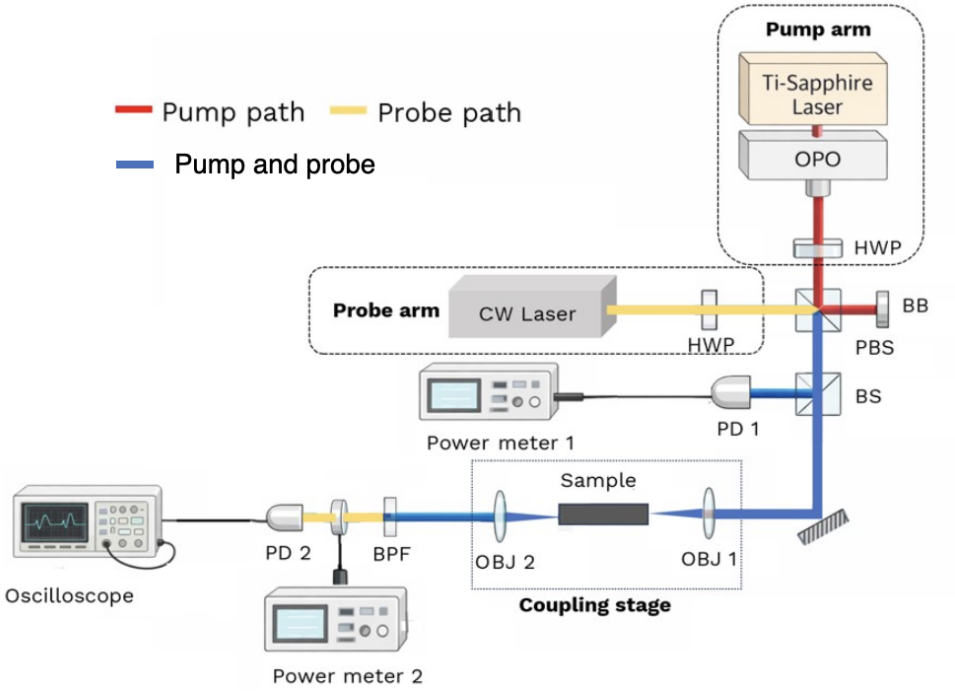


FIGURE 2.7: Schematic of the pump-probe experimental setup used to measure free-carrier lifetime.

The pump–probe experimental setup is schematically shown in Figure 2.7. The experimental pump source was an optical parametric oscillator (OPO, Coherent Inc.), pumped by an 800 nm Ti:Sapphire laser (Mira, Coherent Inc.). The OPO generats picosecond pulses at a repetition rate of 76.6 MHz, with a tunable wavelength range spanning 1200 nm to 1600 nm. A continuous-wave (CW) tunable laser (Santec TSL-710) operating at 1550 nm provided the probe signal. Polarization control for both pump and probe beams was achieved using a polarizing beam splitter (PBS) and a half-wave plate (HWP) placed in each optical arm. A reference photodetector (PD 1) was used to monitor the optical power of the pump or probe beams before they were coupled into the waveguide. The pump and probe beams were simultaneously coupled into the fabricated waveguides using an objective lens (OBJ 1) and collected at the output using a second objective lens (OBJ 2). For FC lifetime measurements, the probe signal was filtered using a band-pass filter (BPF) centered at 1550 nm and detected using a high-speed InGaAs photodiode (PD 2) with a 5 GHz bandwidth and 70 ps rise time. The power meter 1 and 2 were used only during the measurements of the average optical power at the input and output of the waveguide respectively. The temporal evolution of the probe signal was recorded using an 80 GHz oscilloscope connected to PD 2.

At the repetition rate we used in the experiment, successive pulses arrive every $\sim 13\,\text{ns}\,\left(1/76.6\times10^{6}\approx13\,\text{ns}\right)$, corresponding to 13,000 ps, which is approximately 4333 times longer than a 3 ps pulse duration. Based on this separation, we initially expected that the heat deposited by each pump pulse would dissipate before the arrival of the next pulse.

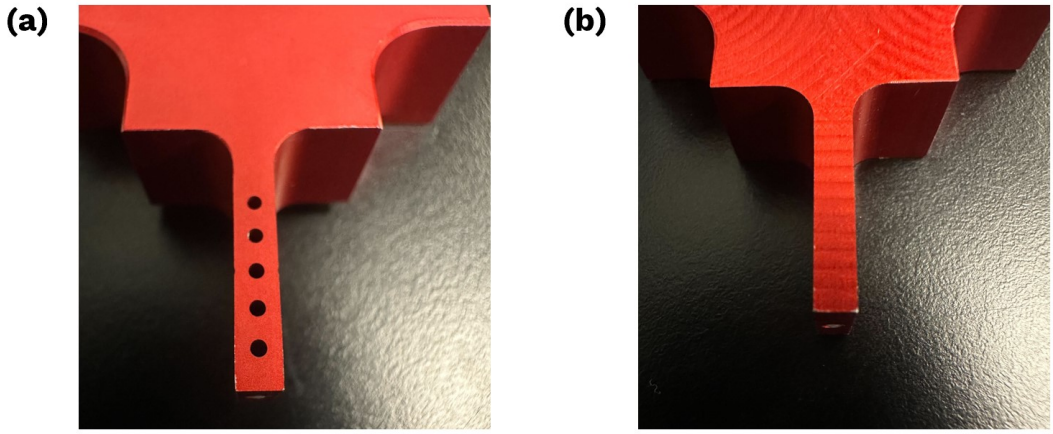


FIGURE 2.8: Top-view image of the sample mount on the translational stage: (a) mount associated with observed thermal instability in the probe signal; (b) mount providing enhanced thermal stability of the probe signal.

Despite this expectation, we observed gradual disappearance of the expected dip in the probe transmittance signal. Instead of a stable transient response, the dip—anticipated from FC dynamics—vanished on a millisecond timescale, consistent with thermal accumulation effects. This behavior suggested that heat buildup within the chip was destabilizing the probe signal associated with carrier dynamics. This interpretation was further supported by improving the thermal contact of the sample with the stage. As shown in Figure 2.8 (a), the initial mount design introduced thermal instability in the probe signal from the waveguide due to reduced contact area caused by mounting holes. In contrast, the modified mount in Figure 2.8 (b), which eliminated these holes, improved thermal contact between the waveguides and the translational stage, thereby reducing local thermal accumulation. Following the transition from the mount in Figure 2.8 (a) to that in Figure 2.8 (b), the probe signal instability disappeared immediately, confirming that the observed effects were due to thermal accumulation arising from insufficient thermal contact between the sample and the mount.

We further observed that, with the mount shown in Figure 2.8 (a), thermal instability in the probe transmittance was less pronounced in silicon waveguide samples, attributed to silicon's higher thermal conductivity and consequently lower effective thermal resistance, which facilitates more efficient

heat dissipation compared to InP [175], [176]. After achieving thermal stability, we were able to observe the probe transmittance repeating consistently with each pulse period, as shown in Figure 2.9.

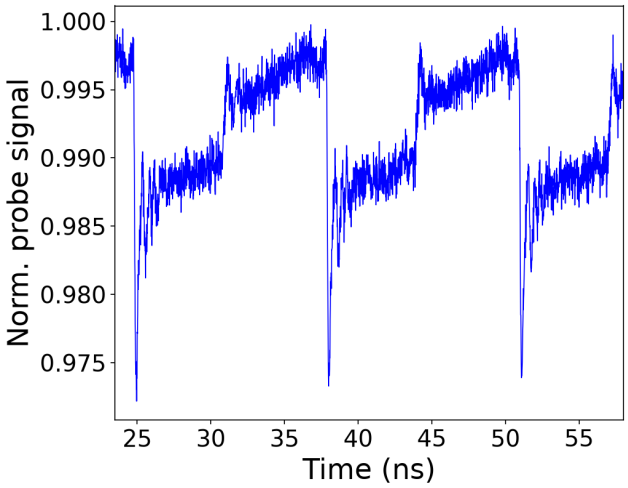


FIGURE 2.9: Normalized probe transmission over three pump pulse periods.

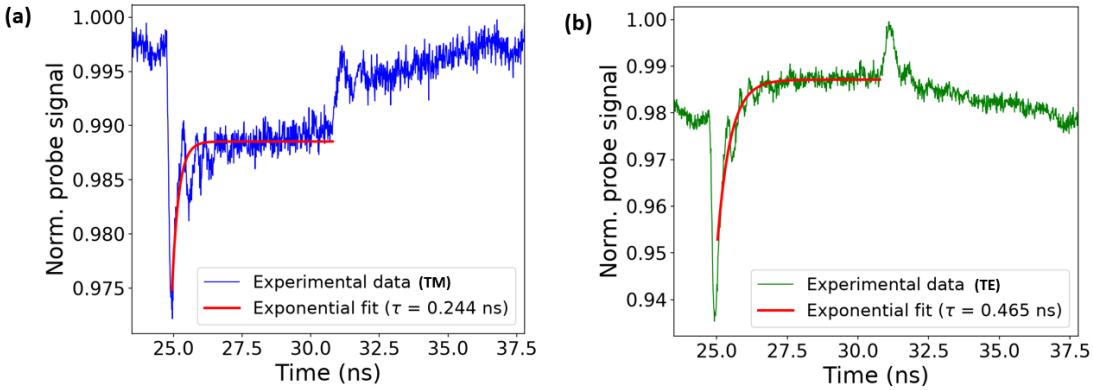


FIGURE 2.10: Normalized probe transmittance for input pump powers of 14 mW and pump wavelength of 1533 nm for (a) TM and (b) TE fundamental mode

A probe power of 87 mW (detected by PD 1) was selected to achieve a sufficient signal-to-noise ratio (SNR) to clearly resolve the transmission dip. At this probe power, measurements performed without the pump showed no measurable modulation of the probe transmission, confirming that the probe itself did not induce any detectable effect in the measured signal. Figure 2.10

presents the normalized probe transmittance recorded at room temperature when the pump beam excites the waveguide's fundamental TE mode in (a) and TM mode in (b), respectively. Normalization is done by dividing the measured probe transmission by its maximum value over the full recorded trace. To determine the FC lifetime (τ), the normalized probe transmission was fitted using the standard exponential function [177]

$$y = y_0 + A\exp(R_0 x), \tag{2.1}$$

where y represents the normalized transmission (T/T_0), y_0 is the unpumped baseline transmission (normalized to 1), A is the modulation depth corresponding to the maximum transmission decrease due to FC absorption, and R_0 is the recovery rate, yielding a FC lifetime of

$$\tau = -\frac{1}{R_0}. \tag{2.2}$$

The fit was restricted to a time window beginning immediately after the transmission minimum and ending just before the onset of a secondary "hump" that appeared several nanoseconds later in every measurement period (the nature of this feature is explained below). This fitting window was selected to isolate the FC recovery from the subsequent thermal response.

Using this fitting procedure, a characteristic FC lifetime of 0.24 ns was obtained for excitation of the fundamental TM mode, as shown in Figure 2.10 (a). Under approximately the same experimental conditions, excitation of the fundamental TE mode yielded a FC lifetime of 0.46 ns as shown in Figure 2.10 (b). The measured FC lifetime is within the same order of magnitude as values reported in the literature for doped InP, while remaining an order of magnitude shorter than those reported for undoped bulk InP [178]. Additionally, observed polarization dependence of the FC lifetime is attributed to the splitting between the heavy-hole and light-hole bands in the valence band of InGaAsP [179]. This splitting removes the energy overlap between the heavy-hole and light-hole states, causing TE and TM polarizations to interact with different hole species. TE-polarized light generates heavy holes because its in-plane electric field aligns with in-plane (p_x, p_y) valence orbitals,

whereas TM-polarized light generates light holes by coupling its perpendicular field to out-of-plane (p_z) orbitals of InGaAsP [180]. Because heavy and light holes have different effective masses and energy states, they relax and recombine at different rates. As a result, TE and TM light create carrier populations with distinct decay speeds, leading to the polarization-dependent FC lifetimes observed in pump-probe measurements.

The secondary hump was observed for both TM- and TE-polarized pump excitation and is attributed to local heating. As shown in Figure 2.11 (a) and Figure 2.11 (b), the amplitude of the hump increases approximately linearly with pump power for both pump polarizations, allowing us to rule out the possibility of significant Auger recombination [181]. Notably, the secondary hump peaks slightly later at higher pump powers compared to lower pump powers. Because pump-excited TPA creates a highly localized central heat spike, higher pump powers generate steeper thermal gradients. Consequently, heat requires more time to diffuse radially outward across the waveguide core to maximize its spatial overlap with the CW probe mode, delaying the peak of the secondary thermal hump [182], [183]. It would be interesting to extend these measurements to waveguides with different lengths or different heat-sinking conditions to investigate how the position and magnitude of the thermal hump change, providing further insight into the thermal dynamics of the device.

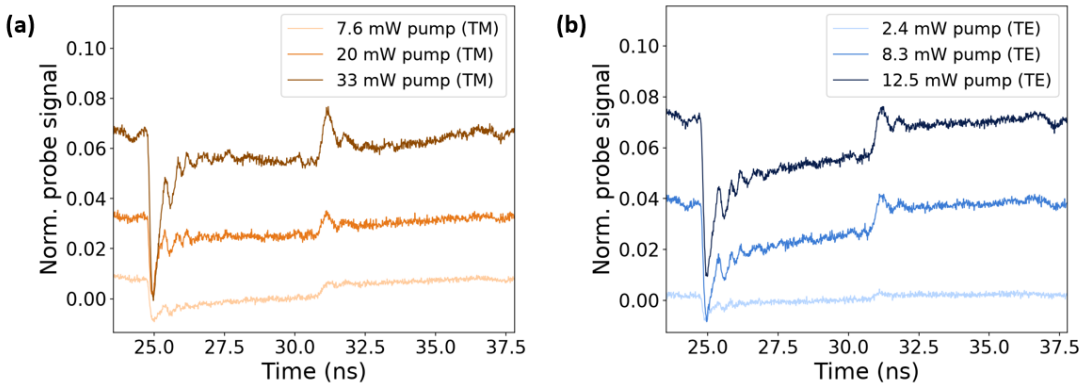


FIGURE 2.11: Normalized probe transmittance at various pump power for fixed input probe powers of 87 mW and pump wavelength of 1533 nm for (a) TE and (b) TM fundamental mode

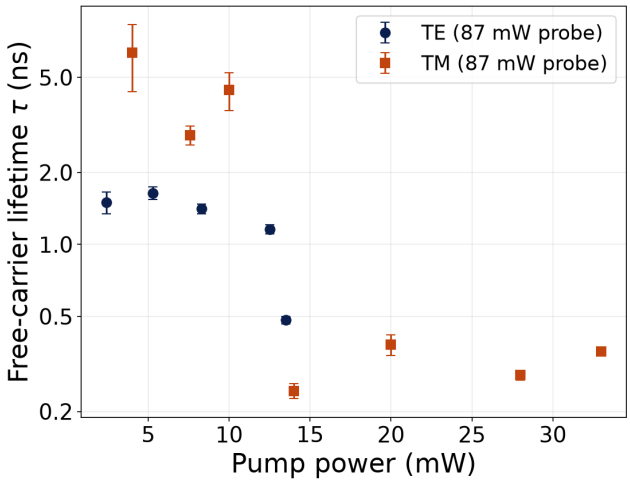


FIGURE 2.12: Free-carrier lifetime as a function of input pump powers at fixed pump wavelength of 1533 nm for TE (blue circles) and TM (red squares) fundamental mode

Additionally, a damped oscillation is present before the signal settles into the plateau used for the exponential fit. This oscillation is attributed to a resonance in the detection electronics rather than to the device under test. Its frequency (2.5 GHz) lies well within the 5 GHz bandwidth of the InGaAs photodiode used for detection (PD 2), in the frequency range where high-speed photodiode packages commonly exhibit resonant peaking due to the interplay between bond-wire inductance and junction capacitance [184], [185]. This interpretation is supported by the observation that the oscillation frequency remained constant over the entire range of pump powers and for both pump polarizations, while only its amplitude scaled with the signal strength. This behavior is consistent with a fixed linear resonance in the detection electronics rather than a power-dependent phenomenon such as carrier–photon relaxation oscillations, as illustrated in Figures 2.11 (a) and Figures 2.11 (b).

Figure 2.12 shows FC lifetime (τ) as a function of pump power for TE- and TM-polarized pump excitation, measured using a fixed probe power of 87 mW (1550 nm probe, 1533 nm pump). The error bars represent the statistical uncertainty (standard deviation) obtained from the single-exponential fit using Equation (2.1). The uncertainity is obtained from covariance matrix of the

nonlinear least-square fit. The lifetime is plotted on a logarithmic scale to accommodate the approximately one-order-of-magnitude variation across the measured range. For TM- polarized pumping, the lifetime decreases sharply from approximately 6.3 ns at 4 mW to a nearly constant plateau of approximately 0.24 – 0.38 ns for pump powers above 14 mW. TE- polarized measurements were performed up to approximately 14 mW to enable a direct comparison of the FC lifetime for TE and TM pump polarizations over the same pump-power range.

To assess the reproducibility of the pump-probe measurements performed in this work, it is important to distinguish between measurement repeatability and variations arising from the fabricated devices themselves. Repeated measurements conducted under identical experimental conditions are expected to yield FC lifetimes that agree within the statistical uncertainty of the exponential fitting procedure. However, variations between nominally identical waveguides can occur because the effective FC lifetime is governed by the density of recombination centers, which may be affected by fabrication-related factors such as surface damage, sidewall roughness, interface trap density, etch-induced defects, and local material quality. In addition, the extracted lifetime can be influenced by the device temperature, as thermal activation of defect states can alter the recombination pathways and consequently modify the measured carrier lifetime.

Nevertheless, fabrication-induced variations are generally modest unless the material or device structure is intentionally engineered to modify the carrier recombination rate. For example, techniques such as ion implantation and controlled wet chemical treatments have been used to introduce additional recombination pathways and modify the FC lifetime in semiconductor waveguides, resulting in changes on the order of several nanoseconds in silicon and InP systems. In contrast, more aggressive lifetime engineering approaches, such as the integration of reverse-biased p–n junctions, can significantly reduce the FC lifetime by efficiently extracting carriers, enabling reductions from nanosecond timescales to the picosecond regime [168], [169].

Therefore, the lifetime measured in this work provides a realistic baseline for modeling the nonlinear response of InGaAsP platform and establishes an initial reference point for future carrier lifetime engineering approaches. The

influence of the FC lifetime range on the performance of InGaAsP ring resonators and the requirements for optimizing this parameter will be discussed in Chapter 3.

Chapter 3

Impact of Nonlinear losses in InGaAsP-OI ring resonators

This chapter presents theoretical analysis of frequency-comb generation in InGaAsP-OI ring resonator. We theoretically investigate the impact of nonlinear losses such as TPA and FCA on the generation of frequency combs in ring resonators made on this platform. We demonstrate that FCA is the primary loss mechanism in an InGaAsP-OI ring resonator at 1550 nm, hindering the observation of frequency comb generation. This issue can be mitigated by reducing free-carrier lifetime closer to the cavity roundtrip time.

The theoretical analysis presented in this chapter was originally performed using the free-carrier lifetime reported for InP [178], which, at the time, was the only available value for a closely related material system. This value was adopted in our original study, published in the Journal of the Optical Society of America B [62]. Subsequently, we experimentally determined the free-carrier lifetime in $In_{0.86}Ga_{0.14}As_{0.30}P_{0.70}$, as reported in Chapter 2 of this thesis. Because this composition more closely resembles the material system considered in our theoretical study, the experimentally measured lifetime provides a more representative parameter for refining the original analysis. Incorporating this value leads to some changes in the predicted results and their interpretation, including certain conclusions. However, these revisions do not invalidate the original theoretical analysis, which remains valid within the assumptions adopted at the time of publication. Rather, the subsequent experimental measurements provide a more accurate physical basis

for the model, allowing us to refine and extend the previously published results. The analysis presented in this chapter thus builds upon our original publication [62] by incorporating experimental findings that became available subsequently.

The frequency comb simulations for the InGaAsP-OI ring resonators presented in this chapter were supported by key technical contributions from group members and collaborators. Dr. Tara Moradi and Dr. Connor Kupchak provided the foundational script implementing the generalized Lugiato-Lefever Equation (LLE). In collaboration with Dr. Laís Fujii dos Santos, a postdoctoral researcher of our group, I contributed to extending this framework to include nonlinear losses in the script. Furthermore, Dr. Laís Fujii dos Santos handled advanced simulation scripting, numerical troubleshooting, and intermediate data analysis while I focused on adapting the simulation framework specifically for the InGaAsP-OI ring resonator geometry, and performing the primary data analysis for the study. The following sections detail the numerical modeling approach used to study frequency comb generation in this device.

3.1 Comb Modeling

The ring resonator under investigation is coupled to a single waveguide, as shown in Figure 3.1 (a). The device is patterned in the InGaAsP layer, which rests on the glass substrate (bottom cladding) and is surrounded by air (top cladding), as illustrated in Figure 3.1 (b). This resonator is of the add-through type: it receives a CW input at one end of the bus waveguide (known as the add port) and produces output (e.g., frequency comb) at the other end (through port).

As described in Chapter 1, InGaAsP has a positive nonlinear refractive index value $n_2 > 0$, therefore anomalous dispersion is necessary to counteract the resonance's Kerr shift and meet the phase-matching condition between the pump mode and the generated sidebands, thereby ensuring efficient and coherent comb formation.

Ignoring FC effects and assuming that the pumps are not depleted by nonlinear energy transfer, one can derive analytical expressions for the frequency spacing between the pump and the generated FWM lines, as well as the

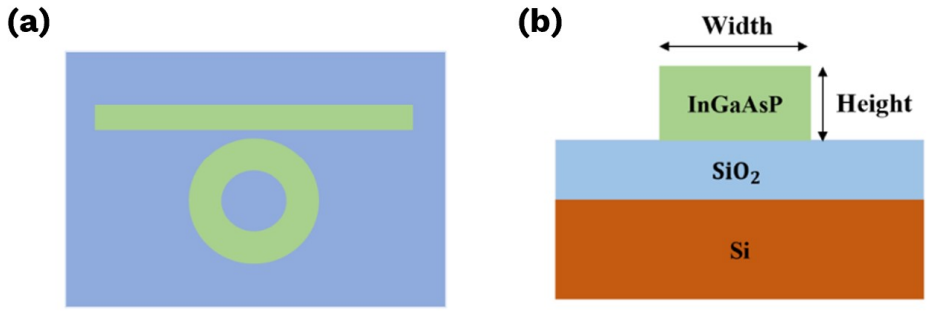


FIGURE 3.1: Schematic drawing of the ring resonator: (a) top view, (b) cross-section.

threshold power,

$$P_{\text{th}} \propto \frac{n}{n_2} \cdot \frac{\omega_p}{D_1} \cdot \frac{A_{\text{eff}}}{Q_L^2}, \tag{3.1}$$

at which the nonlinear gain surpasses cavity losses [186]. Equation (3.1) acts as a guide for efficient comb generation: reducing the refractive index of the material n, the pump frequency ω_p, and the effective mode area A_{eff} leads to a lower threshold power, while increasing the nonlinear refractive index (Kerr coefficient, n_2), FSR (first-order dispersion parameter, D_1), and loaded quality factor Q_L improves conversion efficiency. The loaded quality factor Q_{L} accounts for both internal cavity losses and external waveguide coupling. In the case of critical coupling, $Q_{\text{L}} = Q_0/2$, where the intrinsic quality factor Q_0 is given by

$$Q_0 = \frac{2\pi n_g}{\lambda_0 \alpha_m}, \tag{3.2}$$

with λ_0, and α_m representing the resonant wavelength and power propagation loss coefficient (m^{-1}) respectively [187]. We chose $\omega_p = 2\pi \times 193.41$ THz (telecom C band), and n/n_2 is limited by the material used. The other parameters can be fine-tuned by designing the geometrical features of the resonator. Semiconductor on-insulator platforms naturally offer high refractive index contrast between the core and cladding, reducing the threshold power needed for frequency comb generation by increasing light confinement and lowering propagation losses. The refractive index contrast between the InGaAsP ($n = 3.28$) guiding layer and the SiO_2 cladding ($n = 1.45$) is $\Delta n = 1.83$ at a wavelength of 1550 nm. This high index contrast enables better light confinement, improves the compactness of the integrated device, facilitates

dispersion engineering, and enhances nonlinear optical interactions in ring resonators for more efficient frequency comb generation.

The challenge in increasing the FWM efficiency is that resonant field enhancement may also amplify nonlinear losses. Therefore, we simulate the complete nonlinear problem to determine whether a lower threshold power could allow the formation of frequency combs within a power range where nonlinear losses are less prominent.

Two mathematical frameworks are commonly employed to model frequency comb dynamics in microresonators. The first is the coupled mode equation (CME) approach, in which a separate equation is written for each individual comb line. Due to non-degenerate FWM interactions, the number of nonlinear coupling terms in this formulation scales cubically with the number of modes, rendering it computationally prohibitive for broadband comb modeling [188]. As a result, the CME approach is typically restricted to describing the early stages of comb formation, where only three modes are required to capture the primary degenerate FWM process — a process in which two pump photons of identical frequency interact to generate a signal and idler pair. The second framework is the LLE, a mean-field model, which describes the full intracavity field evolution through a single partial differential equation, irrespective of the number of comb lines [189]. It is termed a mean-field model because it averages discrete cavity effects over a full round trip in the ring. This allows the model to describe the slow temporal evolution of a continuous optical field envelope rather than stepping through discrete, round-trip-by-round-trip propagation maps. By representing all FWM interactions implicitly through a single nonlinear term in the time domain, the LLE inherently circumvents the cubic scaling problem associated with the CME, making it a computationally efficient framework for the simulation of broadband and octave-spanning frequency combs [188], [189].

The LLE, including contributions from TPA and FC effects, can be written as

$$t_R \frac{\partial A}{\partial t} = \sqrt{\theta} A_{\text{in}} + A \Bigg[-\alpha + i\delta_0 + \frac{iL\beta_2}{2} \left(\frac{\partial}{\partial T} \right)^2 + iL\gamma |A|^2 - \frac{\beta_{\text{TPA}}}{2A_{\text{eff}}} L|A|^2 - \frac{\sigma L}{2}(1 + i\mu) \left(\frac{\pi \beta_{\text{TPA}}}{2h\omega_p A_{\text{eff}}^2} \right) |A|^4 \tau_c \Bigg]. \tag{3.3}$$

where $A(t, T)$ is the field amplitude inside the ring, normalized so that $|A|^2$ represents the optical power. The slow time t describes the field changes over multiple round-trips, while the fast time T corresponds to the field's oscillation time scale. The resonator's round-trip time is t_R, θ is the power transmission coefficient, A_{in} is the amplitude of the pump field in the bus waveguide, $\alpha = \alpha_i L + \theta$ is the total linear loss coefficient, α_i is the propagation loss per unit length, $\delta_0 = t_R(\omega_l - \omega_0)$ is the detuning between the laser frequency ω_l and the cavity resonance ω_0, L is the length of the cavity, β_2 is the second-order dispersion coefficient, γ is the nonlinear coefficient, β_{TPA} is the two-photon absorption coefficient, σ is the FCA coefficient, and μ is the FC dispersion parameter. The first term on the right-hand side of the LLE indicates external input. The subsequent terms, in order, account for linear losses, detuning, dispersion, Kerr effect, TPA losses, and the losses due to FC effects. Before proceeding with the numerical analysis of the nonlinear optical response, using the normalized SSFT framework presented in Appendix 8, we need to determine the values of β_2, A_{eff}, and L. In the next section, we will design the resonator's geometry to achieve anomalous dispersion.

3.2 Ring Design

In this section, we assess how variations in each of the geometrical parameters—height, width, and radius, as shown in Figure 3.1 (b)—impact dispersion across a range of wavelengths. The wavenumber for each geometry was computed using the COMSOL Finite Element solver (version 6.5) for wavelengths spanning 1400 to 1700 nm. Second-order dispersion was derived by fitting a second-order Taylor series expansion to the propagation constant

around a reference wavelength within the 1450–1650 nm range. The results are presented in Figure 3.2 (a), (b), (c), corresponding to variations in thickness, width, and radius, respectively.

Figure 3.2 (a) shows the calculated dispersion for different ring thicknesses, demonstrating that anomalous dispersion ($\beta_2 < 0$) can be achieved over a wide range of thicknesses. Figure 3.2 (b) illustrates the strong dependence of dispersion on ring width, with narrower widths shifting the zero-dispersion wavelength. In contrast, Figure 3.2 (c) confirms that ring radius has only a minor effect on dispersion. Although anomalous dispersion can be attained across a broad range of thicknesses, we selected 220 nm to align with the standard for silicon-on-insulator. A width of 490 nm was chosen because it permits single-mode operation at 1550 nm. Additionally, the selected cross-section is resilient to fabrication-related variations in size and accounts for constraints related to electron-beam lithography and etching in subsequent stages [190]. The ring radius was kept sufficiently small to increase D_1 and minimise the device footprint, but not so small as to cause excessive bending losses. Finally, Figure 3.2 (d) presents the simulated group-velocity dispersion (GVD) for the selected geometry (490 × 220 nm cross-section, 25 µm radius). The results show anomalous dispersion ($\beta_2 < 0$) over a broad wavelength range that includes 1550 nm, confirming the suitability for telecom-band operation.

Figure 3.3 shows the mode area difference calculated across a range of ring widths and thicknesses. This difference indicates the deviation between the physical ring cross-sectional area and the effective mode area of the TE mode within the ring cross section. As observed, the mode area difference tends to increase as the ring's cross-sectional dimensions decrease. This trend is particularly advantageous for reducing propagation loss, since tighter mode confinement within the core diminishes sensitivity to surface roughness and fabrication defects. The calculated mode area for the fundamental TE mode and the specified cross-section is 0.09 µm^2. The small value results from the high refractive index contrast between InGaAsP and the underlying layer.

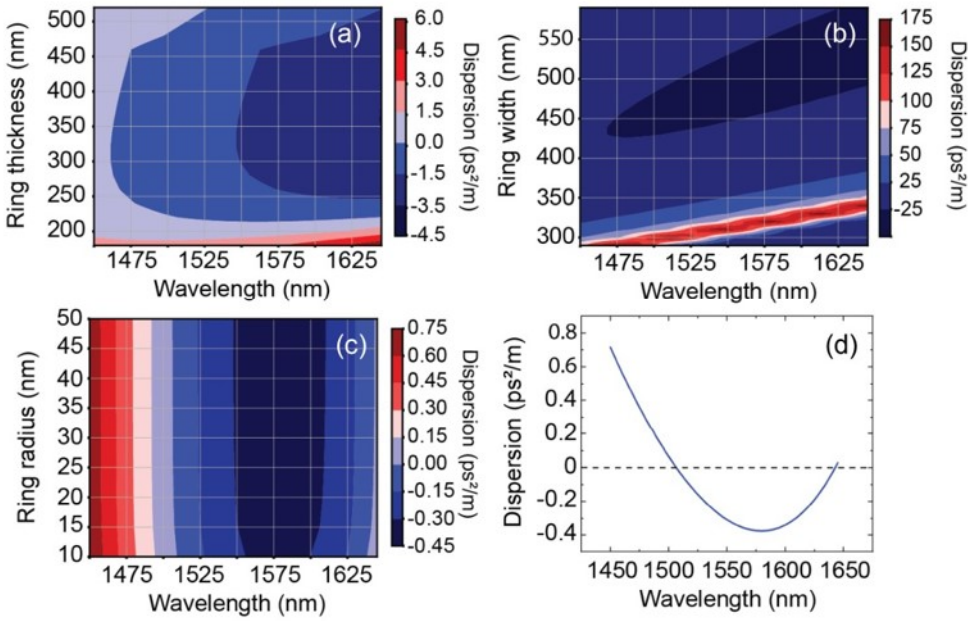


FIGURE 3.2: Dispersion as a function of wavelength for a range of (a) ring thicknesses, (b) ring widths, (c) ring radii, and (d) modeled GVD of the ring.

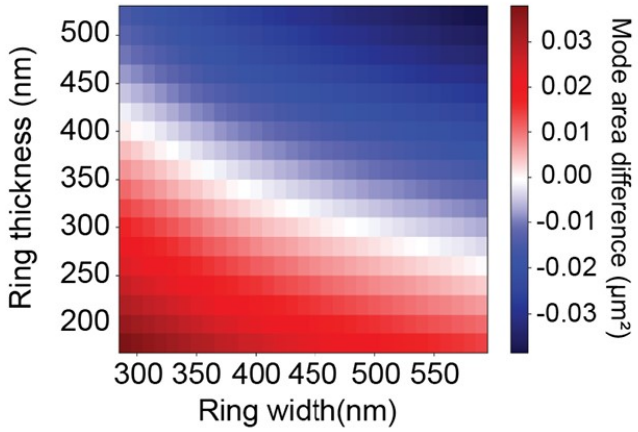


FIGURE 3.3: The mode area difference calculated across a range of ring widths and thicknesses

3.3 Results and Discussion

We begin our analysis assuming zero nonlinear loss in the ring resonator at a 1550 nm operating wavelength. The lowest propagation loss reported in InGaAsP-OI is 4 dB/cm for a nanowire waveguide [191], but more recent

results in AlGaAs-OI ring resonators reached propagation losses as low as 0.2 dB/cm [31], leading us to believe that lower losses are attainable for modified cross-sections. Thus, we shall consider $\alpha_i = 12.9\ \mathrm{m}^{-1}$ (0.6 dB/cm). By performing the detuning sweep at different pump power levels, we identified the threshold for frequency comb generation to be ∼1 µW. Figure 3.4 (a) shows the average output intensity across all modes as a function of normalized detuning, generated at 10 µW pump power. As the detuning increases (approaching the cavity resonance from the blue side), the intracavity energy rises due to resonant buildup. Consequently, the device resonance undergoes a red-shift due to the Kerr effect, which prevents the pump frequency from aligning with the shifted cavity resonance. As a result, the input field passes through the ring and exits via the through port. The transmitted spectrum is predominantly influenced by the pump field, as illustrated in Figure 3.4 (b).

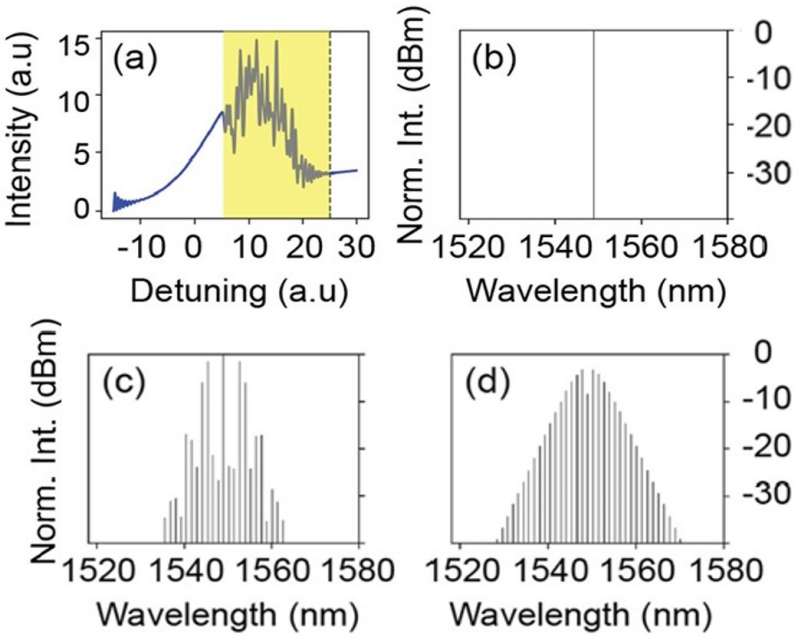


FIGURE 3.4: (a) Intensity as a function of detuning at 10 µW pump power, with the instability region highlighted. Simulated frequency spectra of the device at a detuning (b) before the instability region, (c) within the instability region, and (d) after the instability region.

An additional increase in the normalized detuning raises the intracavity power

beyond the FWM threshold, leading to the creation of comb lines with unstable amplitudes and phases, as shown in Figure 3.4 (c). This unstable region is marked in yellow in Figure 3.4 (a). For larger detuning values, $\delta_0/\alpha > 25$, a balance is established between nonlinear effects, GVD, cavity losses, and detuning, resulting in a frequency comb that remains stable in both amplitude and phase, as illustrated in Figure 3.4 (d). Consequently, a soliton microcomb can be produced with an input power of 10 µW.

Figure 3.5 (a) provides a deeper understanding of how the field changes over time across the three operating regimes. Initially, before reaching the instability region, the field exhibits low intensity. This is followed by irregular and fluctuating patterns within the instability region, indicating the start of nonlinear dynamics. Beyond a detuning of 25, the emergence of well-defined, localized pulses signifies the formation of solitons. Figure 3.5 (b) shows how the spectral content evolves across the three regimes. At low detuning, a single band centred at mode number zero represents the pump mode. As detuning increases, multiple sidebands begin to form around the pump, ultimately resulting in well-defined comb lines that are evenly spaced and maintain steady-state intensity, which points to soliton formation. The parameters used for the simulations in this section are listed in Table 3.1.

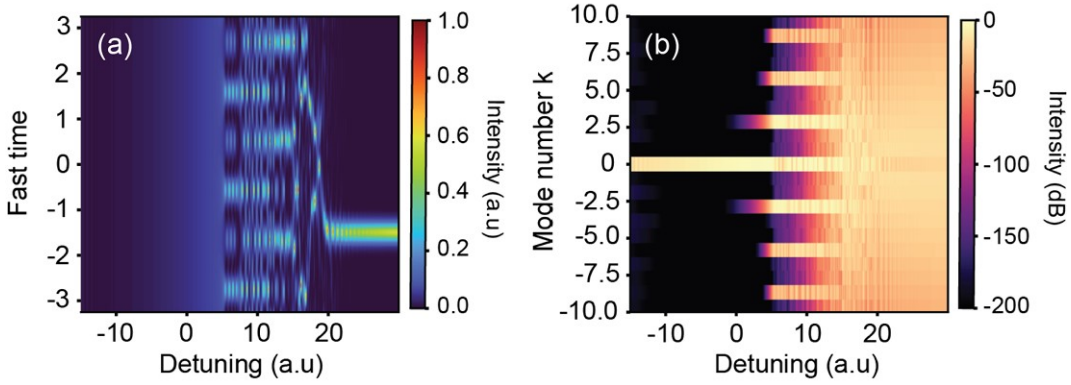


FIGURE 3.5: (a) Temporal evolution of the intracavity field as a function of normalized detuning. (b) Evolution of the frequency comb spectrum with varying normalized detuning.

TABLE 3.1: InGaAsP-OI ring resonator parameters used in numerical modelling. n_2 and β_{TPA} [28], σ and μ [192], and τ [178].

Pump power (μW)	10
Wavelength (nm)	1550
Waveguide area (nm^2)	490×220
Ring radius (μm)	25
α	4×10^{-3}
α_i (m^{-1})	12.9
n_2 (m^2/W)	19×10^{-17}
β_{TPA} (W/cm)	1.9×10^{-12}
σ (m^2)	1.47×10^{-21}
μ	7.5
τ_C (ns)	3 / 0.003 / 0.46

To identify the primary nonlinear mechanism in the ring, we numerically solved the LLE, including the nonlinear loss terms. The transmission frequency spectra of the ring, both excluding and including nonlinear absorption (TPA), are shown in Figure 3.6 (a) and (b), respectively. In the presence of TPA, the broadest frequency comb was observed at a normalized detuning of 15, but the solitonic regime was not reached. Although fewer comb lines are excited—indicating a higher threshold power—TPA alone cannot fully prevent the formation of the comb.

We further included the FCA effect alongside the TPA to examine its influence on the comb generation process. When we set the free-carrier lifetime to 3 ns [178] from the literature and 0.46 ns from the measurement results from Chapter 2, the comb disappears, as shown in Figure 3.6 (c). Frequency comb generation (FCG) was not observed in the presence of TPA and FCA even after increasing the pump power. This result differs from previous reports for silicon [167], where TPA alone was enough to disrupt comb formation, but three-photon absorption without free carriers still allows FCG.

It has also been demonstrated that a key parameter affecting FCA's influence

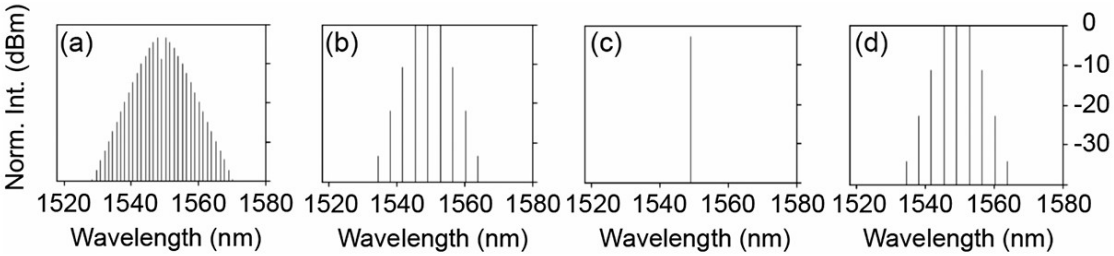


FIGURE 3.6: Simulated frequency spectra of the device collected at the through port of the bus waveguide: (a) in the absence of nonlinear losses, (b) with TPA included, (c) with TPA and FCA (3 ns and 0.46 ns FC lifetime), (d) with TPA and FCA (3 ps FC lifetime).

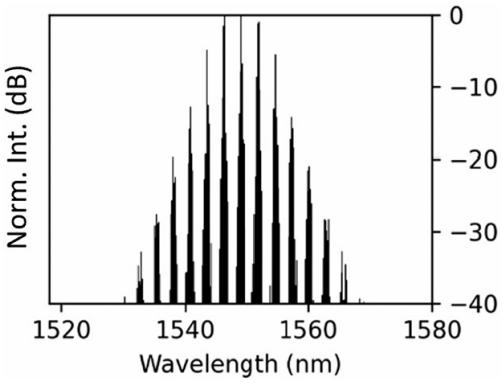


FIGURE 3.7: Simulated frequency spectra of the device with increased propagation loss at input power 2.6 mW.

on comb generation is the free-carrier lifetime. When the FC lifetime is intentionally reduced close to the cavity's round-trip time (e.g., $\tau_c \approx 3$ ps), rapid carrier recombination occurs between successive round trips. This prevents the cumulative buildup of free-carrier density (N_c) over multiple passes, directly suppressing FC effects [167]. As a result, the net intracavity optical loss remains below the parametric threshold, allowing Kerr nonlinear gain to dominate and restoring stable frequency comb generation, as shown in Figure 3.6(d). Introducing defects through ion implantation or using a p-i-n structure can decrease the FC lifetime to just a few picoseconds or less [168]. Previously, it has been shown that tunable control of the free-carrier lifetime down to several picoseconds in Si ring resonators is achievable by integrating a lateral PIN diode with the ring resonator [193]. Additionally, recent efforts to integrate a PIN diode with InGaAsP-OI waveguides have gained

attention for their potential to create efficient, tunable optical attenuation in Variable Optical Attenuators (VOAs) on the InGaAsP-OI platform [26]. The fabrication techniques used show promising prospects for future integration of PIN diodes with ring resonators on this platform [26]. In Appendix 9, we present numerical calculations of the effective FC lifetime as a function of reverse-bias voltage for an InGaAsP-OI waveguide integrated with a p-n junction. An additional simulation was performed using the same core dimensions and material composition as the microring resonators analyzed in this chapter. The results demonstrate that increasing the reverse bias to 5.0 V significantly reduces the carrier extraction time down to the sub-picosecond regime ($\tau_{ext} < 0.2$ ps).

The propagation loss of the device and, consequently, the quality factor, also significantly influence the threshold power, as outlined by Equation (3.1). This was validated by modelling the frequency spectra of the device with a propagation loss of 13 dB/cm reported for the InGaAsP on InP platform in previous research [194]. As demonstrated in Figure 3.7, the simulated result indicates a threshold power of approximately 2.6 mW, which is several orders of magnitude higher than the 10 µW threshold observed in our device. Notably, considerable propagation loss reduction has been achieved in AlGaAs-OI integrated photonic structures. Therefore, it is anticipated that the InGaAsP-OI platform can exhibit lower propagation loss compared to its InGaAsP/InP counterpart. This underscores the vital role of the InGaAsP-OI platform in enabling ring resonators for frequency comb generation.

In conclusion, we examined the nonlinear optical performance of InGaAsP-OI ring resonators considering TPA and FCA effects. We find that FCA is a significant source of loss at the telecom C-band, causing disruption of FCG. We demonstrate that reducing FC lifetime and threshold power can help mitigate the impact of FCA effects and restore FCG in InGaAsP-OI ring resonators. Additionally, we present GVD analysis for different widths, heights, and radii of the device. This study aids in understanding the feasibility of implementing FCG in InGaAsP at the telecom C-band, where this material platform is used for photonic integration to support classical telecommunication systems.

Chapter 4

Development of III-V-on Insulator Photonic Integration Platforms

The results presented in Chapters 2 and 3 established the theoretical feasibility of nonlinear photonic devices based on the InGaAsP-OI platform. In particular, the incorporation of experimentally measured free-carrier lifetime into the analysis demonstrated that InGaAsP-OI remains a promising platform for nonlinear integrated photonics and optical frequency-comb generation despite the presence of TPA and free-carrier effects when free carrier lifetime is reduced to picosecond (ps) range.

Having established the potential of the platform, this chapter turns to its experimental realization. We investigate the fabrication processes required for III–V semiconductor-on-insulator photonic integration, considering two material platforms: InGaAsP-on-insulator (InGaAsP-OI) and aluminum gallium arsenide-on-insulator (AlGaAs-OI). Although these platforms possess different optical properties, they share many common fabrication challenges and process-development steps, including wafer bonding, substrate removal, and thin-film processing. For this reason, they are considered together in this chapter, allowing common fabrication methodologies and platform-specific considerations to be discussed within a unified framework.

The fabrication of these platforms involves several process steps, including epitaxial growth, wafer bonding, substrate thinning, substrate removal, and etch-stop layer removal. However, this chapter focuses specifically on the development and optimization of two key process steps: wafer bonding, which is applied to all III–V–OI platforms and substrate removal, which is

addressed only for the AlGaAs-OI platform. These steps are critical for the realization of III–V–OI platforms.

Within this scope, two direct bonding methods—SiO_2-to-SiO_2 and Al_2O_3-Al_2O_3—as well as an adhesive bonding approach using a positive-tone e-beam resist Medusa, are investigated. In all cases, bonding strength was evaluated using a half-cut dicing test performed with a dicing saw [195]. The cross-sections of the diced samples were then examined using SEM.

Successful bonding was indicated by clean dicing without debonding of the wafers during or after the process, along with the absence of voids at the bonding interface in SEM images. These criteria were used to assess bonding quality and to verify that the bonding strength had reached an optimal level, sufficient to withstand subsequent substrate removal processes such as grinding or lapping [195]. The half-cut dicing test also serves as a practical indicator of the bond's durability under mechanical stresses comparable to those encountered during substrate removal [196].

While wafer bonding techniques such as direct oxide-to-oxide and polymer adhesive bonding are established in the broader literature, their successful implementation is highly sensitive to the specific material stack, surface morphology, and post-processing chemical constraints. In this chapter, the primary novelty lies not in inventing an entirely new bonding mechanism, but in evaluating and adapting established bonding methodologies specifically to the InGaAsP-OI photonic platform. While prior literatures, often focuses on final device performance, the platform-specific microfabrication constrains during bonding and interface stability during substrate removal remain critical areas of investigation [30]. Furthermore, while adhesive bonding methods like Hydrogen Silsesquioxane (HSQ) bonding have been demonstrated for material systems such as silicon carbide (SiC) and gallium nitride GaN-to-silicon transfers, its application to telecom-grade III-V-OI photonic integration represents an unaddressed pairing of process and material system [197], [198]. In this chapter, HSQ-mediated adhesive bonding is systematically evaluated for the InGaAsP-OI platform to elucidate the underlying interface mechanics, identify critical processing limits, and propose actionable mitigation strategies. This work systematically maps the physical limitations, surface requirements, and interface failure modes across direct, PECVD-based,

Al_2O_3, and adhesive bonding approaches to establish a viable fabrication path for integrated III-V-OI photonic platforms.

The experimental work presented in this chapter was carried out in close collaboration with group members and external researchers. My primary contribution included conducting the wafer bonding and substrate removal experiments, dicing, and SEM imaging for interface characterization. The Medusa spin-coating and Al_2O_3 atomic layer deposition (ALD) processes were performed by Dr. Lais Fuji Dos Santos, a postdoctoral researcher in our group, at the University of Waterloo's nanofabrication facility, who also contributed to the Al_2O_3 and HSQ bonding trials. Additionally, development of the GaAs wet-etching recipe benefited from insightful discussions with Dr. Mathieu De Lafontaine, formerly a post doctoral scientist and presently an Assistant Professor at the University of Ottawa.

4.1 SiO_2 to SiO_2 direct bonding



FIGURE 4.1: Schematic illustration of SiO_2-to-SiO_2 direct bonding.

We begin with the investigation of SiO_2-to-SiO_2 direct bonding, which serves as the baseline direct bonding approach in this work. A schematic of the wafers to be bonded is shown in Figure 4.1. Commercially available 2-inch SiO_2-on-silicon wafers were cleaved into four roughly equal pieces, and two

of these pieces were used to optimize the SiO_2-to-SiO_2 direct bonding process. Each sample consisted of a 3 μm SiO_2 top layer deposited via thermal oxidation on a 250 μm silicon substrate. Surface preparation began with standard cleaning: the samples were gently sonicated at 80 kHz and 50% amplitude (equivalent to to 30 W of effective acoustic output) for 5 minutes in acetone, followed by Isopropanol, and finally DI water. After sonication in each solvent, the samples were dried using a N_2 blow. To remove any remaining moisture, the samples were placed on a hot plate at 110°C for 5 minutes. AFM imaging confirmed a surface roughness of 0.32 nm for a cleaned sample. The surfaces were then treated with O_2 plasma in a plasma treatment tool (PE-50) at 39 W RF power, 26 sccm O_2 flow, and 15 mTorr chamber pressure for 45 seconds [98]. This step passivates the surface by increasing the density of hydroxyl (Si-OH) groups, facilitating spontaneous room-temperature bonding and removing residual organic and inorganic contaminants [98], [195], [199]. To assist the escape of gases produced at the bonding interface during the bonding, the samples were briefly dipped in 0.025% HF for 1 minute to introduce mild surface porosity [196]. After a DI water rinse, the samples were immersed in 29% NH_4OH for 10 minutes, which terminated the surface with amine (-NH_2) and hydroxyl (-OH) groups [95]. Upon physical contact, the electron-rich amine groups promote hydrogen bonding and proton transfer, forming Si-O-Si bonds and releasing NH_3 as a byproduct [95]:

$$Si - NH_2 + Si - OH \rightarrow Si - O - Si + NH_3. \tag{4.1}$$

Without NH_4OH treatment, the reaction would instead produce water [200]:

$$Si - OH + HO - Si \rightarrow Si - O - Si + H_2O. \tag{4.2}$$

Water formed at the interface, together with residual water absorbed in the SiO_2 layer, can evaporate during post-bond annealing, causing local debonding or void formation [95]. H_2 gas generated via

$$Si + 2H_2O \rightarrow SiO_2 + 2H_2\,(g) \tag{4.3}$$

can also contribute to voids, which is why the HF-induced porosity is critical [196]. The small H_2 molecules can diffuse through these porous surfaces without being trapped at the bonding interface.

After NH_4OH treatment, the samples were immediately brought into contact manually in air at room temperature on the lower platen of a wafer bonder. The chamber was then pumped down to a vacuum of 6.7×10^{-5} Torr. The platen temperature was ramped at 5 °C/min to 300 °C in vacuum while applying an initial force of 454 N (0.89 MPa), consistent with literature values [200]. Once the platen reached 300 °C, annealing was maintained for 1 hour. The applied force increased to 2228 N from the force applied initially due to thermal expansion of the sample upon annealing, after which the heater was turned off and the platen allowed to cool naturally overnight. All wafer bonding tests were performed using a wafer aligner bonder from Applied Microengineering Ltd. (AML). Half-cut dicing test was then carried out using a dicing saw at a cutting speed of 20 mm/minute. The test revealed localized voids of a few hundred nanometers, indicating partial bonding as shown in Figure 4.2.

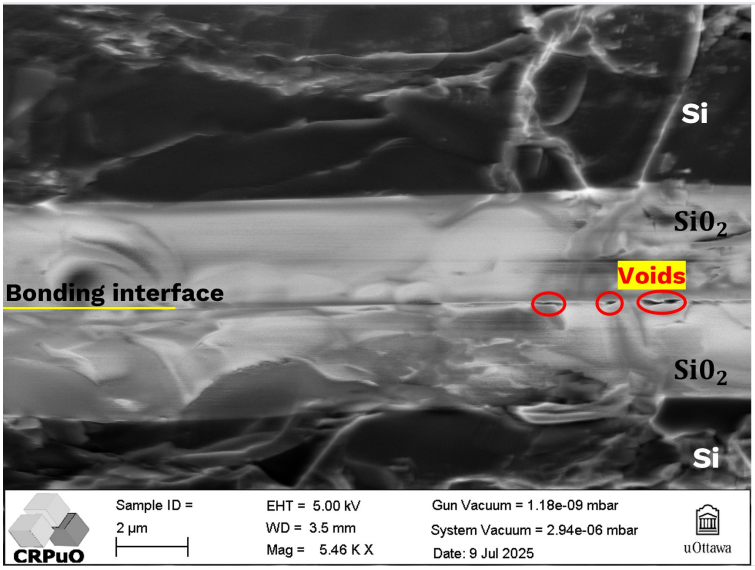


FIGURE 4.2: SEM image of the cross-section of partially successful directly bonded thermally grown SiO_2-to-SiO_2 layers on a silicon substrate, with bonding interface highlighted in yellow and voids indicated in red.

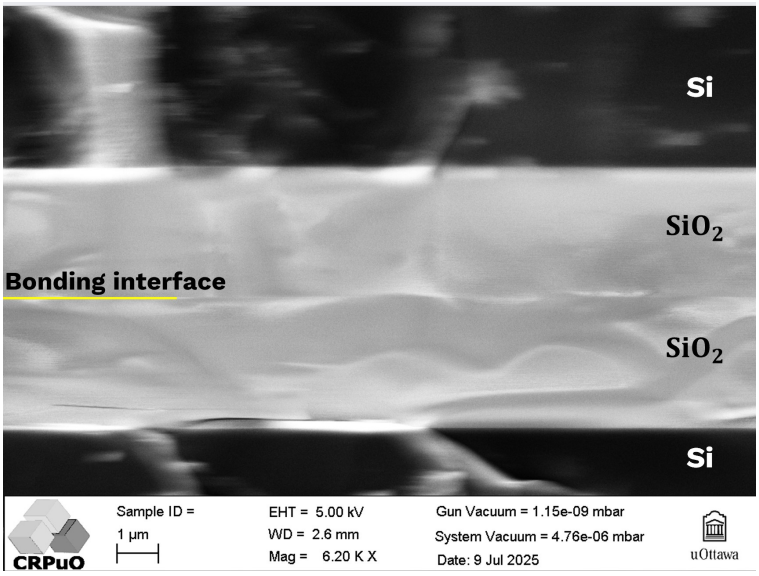


FIGURE 4.3: SEM image of the cross-section of successfully bonded thermally grown SiO_2-to-SiO_2 layers on a silicon substrate, with the bonding interface highlighted in yellow.

To optimize the bonding recipe further, the annealing time was extended to 2 hours and the applied force reduced to 104 N (0.2 MPa) to minimize excessive mechanical stress at elevated temperature. This modification was motivated by the observation that the previous sample felt unusually stiff during handling, possibly indicating the presence of residual stress generated during the bonding process. Rest of the surface preparation steps and parameters were kept unchanged. SEM imaging of the cross section of the samples revealed a completely void-free interface, demonstrating that the optimized procedure achieved full and successful SiO_2-to-SiO_2 bonding, as shown in the Figure 4.3.

In the next step, this bonding recipe was evaluated for SiO_2/InGaAsP/InP to SiO_2/Si wafer bonding. The SiO_2/InGaAsP/InP sample was a 2 cm × 1 cm piece cleaved from a two-inch MOCVD-grown InGaAsP-on-InP wafer, with a PECVD-deposited SiO_2 layer on top. The epitaxial growth of the InP/InGaAsP wafers was performed by the Center for Integrated Nanotechnologies (CINT) and Sandia National Laboratories, while the PECVD SiO_2 deposition was carried out at Carleton University. The SiO_2/Si sample had similar dimensions as the SiO_2/InGaAsP/InP sample and consisted of a 3 μm thick oxide layer on a 250 μm silicon substrate and showed good surface

quality as observed previously. However, after bonding, the samples were found to be debonded upon removal from the bonding machine, indicating bonding failure. This was primarily attributed to the rough PECVD SiO_2 surface on the InGaAsP/InP sample. Microscopic images of the PECVD deposited sample surface after solvent cleaning show foreign particles, tens of nanometers in size, distributed across the surface as shown in Figure 4.4.

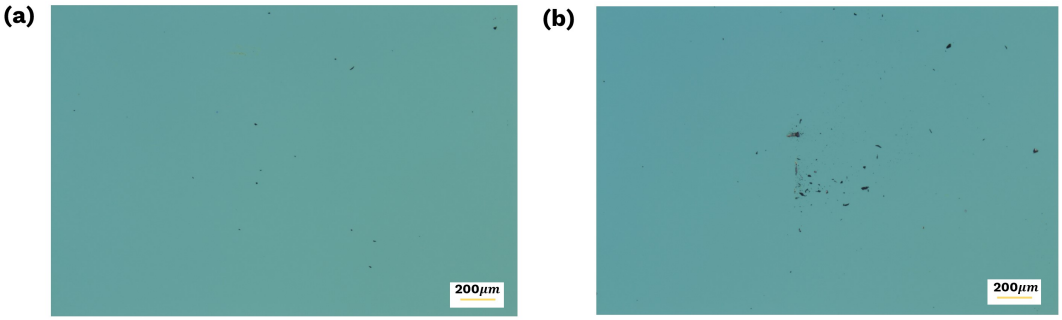


FIGURE 4.4: Optical microscopic images of surface of PECVD-deposited SiO_2 on InGaAsP after standard cleaning.

This may arise from chamber contamination or from the inherent nonhomogeneity of the PECVD process [201]. By nonhomogeneity, we refer to effects such as incomplete reactant molecules becoming trapped within the SiO_2 film, as well as spatial variations in the plasma or in the distribution of reactant species across the wafer surface [202], [203]. The roughness of SiO_2 deposited by PECVD also scales with the thickness of the deposited oxide, unlike thermal oxidation, where the roughness decreases as the SiO_2 thickness increases [195]. Furthermore, O_2 plasma cleaning of the SiO_2 surface prior to bonding may oxidize the underlying III–V layer, leading to increased propagation losses in the resulting devices [204], [205]. Due to these limitations, this approach was not pursued further.

Deposition of SiO_2 by thermal oxidation on III–V layer is also not a viable option, as it typically requires temperatures above 900 °C, which are incompatible with III–V materials [206], [207]. An alternative CVD technique, Low pressure CVD (LPCVD) can deposit high-quality, smooth silica on III–V substrates; however, it generally requires temperatures exceeding 300 °C [208]. Such elevated temperatures can induce thermally driven dislocations in III-V

semiconductors, which may degrade the optoelectronic performance of devices fabricated on this platform [207].

4.2 Al_2O_3 to Al_2O_3 direct bonding

To address the challenges we observed in SiO_2 to SiO_2 direct bonding, we explored the use of an alumina (Al_2O_3) intermediate layer for bonding III–V materials to SiO_2. Direct bonding of Al_2O_3 thin films—commonly deposited using Atomic Layer Deposition (ALD)—has several advantages. ALD enables the growth of sub-nanometer-thick Al_2O_3 films at relatively low temperatures (150–200 °C) while achieving surface roughness as low as 0.3 nm [209]. Moreover, the interface quality between III–V materials and ALD-grown Al_2O_3 is superior to that of III–V/SiO_2 interfaces [87], [210]. Al_2O_3 also exhibits a significantly higher hydroxyl group density (18 OH/nm^2) compared to silicon-based materials, along with electrical resistivity and thermal conductivity comparable to silica [87], [211], [212]. The hydroxyl group density can be further increased by exposing the Al_2O_3 surface to water or water vapor prior to bonding [26], [213]. Another method for enhancing room-temperature bonding strength involves irradiation with an argon fast atom beam, which removes organic contaminants and native oxides, leaving highly reactive surface states that promote stronger bonding [214], [215]. However, this technique has primarily been demonstrated for SiO_2/Si wafer bonding, whereas water-assisted activation has also been successfully applied to III–V semiconductor platforms [26].

During direct Al_2O_3–Al_2O_3 bonding, when both the III–V and SiO_2 surfaces are coated with Al_2O_3, surface hydroxyl groups undergo the following condensation reaction [213]

$$Al{-}OH + Al{-}OH \rightarrow Al{-}O{-}Al + H_2O. \tag{4.4}$$

In contrast, in Al_2O_3–SiO_2 bonding, as demonstrated in AlGaAs-OI, Al_2O_3 is deposited only on the III-V layer and bonded onto SiO_2 [30]. In this case

bonding interface reaction follows [216]

$$Al{-}OH + Si{-}OH \rightarrow Al{-}O{-}Si + H_2O. \tag{4.5}$$

An additional advantage of this approach is presenting a chance to pattern the lower bonding layer (SiO_2) with vertically etched channels several micrometers deep and spaced using lithography [61]. These channels can serve as pathways for hydrogen removal—originating, for example, from ALD-deposited Al_2O_3 (particularly when bonding occurs above the Al_2O_3 deposition temperature) or from residual water vapor—thereby facilitating gas elimination and potentially improving bond quality [58], [61].

We initially evaluated Al_2O_3–Al_2O_3 bonding using standard SiO_2/Si wafers. A 2-inch SiO_2/Si wafer, consisting of a 3 μm thermally grown SiO_2 layer on a 250 μm Si substrate, was cleaned using a standard cleaning procedure as mentioned earlier. Subsequently, a 5 nm Al_2O_3 film was deposited by ALD at 150 °C at the University of Waterloo by our group's postdoctoral researcher, Dr. Lais Fujii dos Santos. After bringing the wafer to the University of Ottawa, AFM measurements were performed to evaluate the surface roughness of the deposited layer. AFM measurements after deposition showed a surface roughness of around 0.3 nm, which is suitable for direct bonding. Following AFM characterization, the wafer was cleaved into 1 cm × 1 cm pieces. These samples were immersed in DI water for one minute, gently dried with nitrogen blow, and then brought into contact in air at room temperature on the lower platen of the wafer bonder. The chamber was evacuated to $\sim 10^{-5}$ Torr, and the platen temperature was ramped at 5 °C/min to 200 °C —lower than literature values—to investigate how the applied force evolves during post-bond annealing [30]. An initial force of 247 N, slightly higher than reported values, was applied [30]. Once the platen reached 200 °C, the samples were annealed for 1 hour. Due to thermal expansion, the applied force increased from 247 N to 701 N. The system was then allowed to cool naturally overnight. The final force of 701 N was relatively low compared to that observed in SiO_2–SiO_2 direct bonding at similar temperatures. To compare, the process was repeated at 300 °C used in literature with an initial force of 298 N [217]. In this case, the final force approximately doubled relative to the previous trial. However, bonding failed in both cases, as confirmed by

inserting a blade at the interface; the samples separated easily.

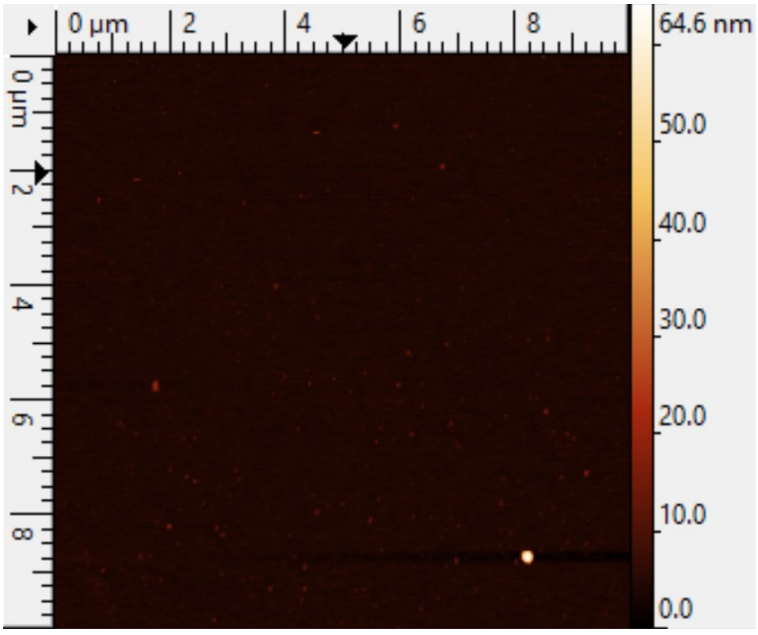


FIGURE 4.5: AFM images of the cleaved sample from a 2-inch SiO_2 /Si wafer after ALD deposition of Al_2O_3. Light red dots visible in the dark background are attributed to the residue generated during the cleaving process.

In a subsequent experiment, the initial force was increased to 900 N, resulting in a final force of 2868 N, which was expected to be sufficient based on prior SiO_2–SiO_2 bonding trials. Despite this, the samples separated upon blade insertion once again. In addition to this method, Dr. Lais Fujii dos Santos and I conducted several bonding experiments comparing samples with and without a pre-bonding DI water dip, but neither approach yielded strong bonding. These failures were attributed to edge roughness introduced during cleaving of the 2-inch wafer after Al_2O_3 deposition which we confirmed through visual inspection.

A comparison between our experimental outcomes and published Al_2O_3-to-Al_2O_3 bonding reports reveals critical process dependencies that are often under-reported in the literature. While certain studies report direct alumina bonding without surface plasma activation, our attempts using non-plasma workflows yielded no adhesion [26], [218]. This discrepancy indicates that non-plasma bonding inherently relies on pristine, full-wafer conditions with minimal surface contamination and negligible surface roughness (RMS < 0.5 nm). In contrast, workflow involving cleaved sample require protective measures—such as spin-coating a photoresist layer prior to cleaving—to prevent the mechanical edge topography and particulate debris that otherwise cause bonding failure in the absence of surface plasma activation.

Conversely, literature sources that advocate for plasma-assisted bonding often cite annealing times and temperature, but frequently omit key plasma parameters—specifically the active gas chemistry, chamber pressure, and RF power setting [30], [44]. Because different plasma species selectively govern either surface chemistry activation (hydrophilicity) or physical ion bombardment (which can adversely increase surface roughness), the absence of specified plasma recipes in prior works presents a significant barrier to process translation. Our results demonstrate that Al_2O_3 direct bonding is highly sensitive to these unstated process variables, confirming that without precisely tuned plasma activation or dedicated surface protection during sample preparation, direct alumina bonding lacks the process window needed for reliable III-V-OI integration.

4.3 Adhesion bonding using Medusa

Another approach we investigated was adhesive bonding using HSQ. First introduced as a negative-tone electron-beam resist by Namatsu et al. in 1998, HSQ develops SiO_2-like properties when exposed to an electron beam or after thermal treatment [219], [220], [221]. It has primarily been studied as an intermediate adhesive layer for bonding GaN to glass or silicon substrates to enhance device functionality and performance [197], [222], [223]. When we chose to pursue this method, HSQ was not available, so we used Medusa-84 as an alternative. Medusa is a variant of HSQ sharing similar

chemical structure as described in Chapter 2, yet has a different casting solvent compared to HSQ [224]. It offers a longer shelf life—approximately six months when stored below 5 °C—and, when used as an electron-beam resist, shows improved resistance to aging, allowing a delay of several weeks between spin coating and exposure [224]. Medusa-84 was sourced from the Quantum-Nano Fabrication and Characterization Facility (QNFCF) of University of Waterloo. Dr. Lais Fujii dos Santos spin-coated Medusa onto several InGaAsP/InP and SiO_2/Si samples, each approximately 1 cm × 1 cm in size, achieving a film thickness of about 200 nm. One batch was cured, while another one was left uncured to compare bonding strengths. The samples were then brought to the University of Ottawa Nanofabrication Facility, where profilometry measurements indicated an edge bead of approximately 150 nm. Bonding was carried out by Dr. Lais Fujii dos Santos and myself using a platen force of 258 N, consistent with literature values, at 300 °C for 2 hours. Three sets of samples were bonded in the same run: one fully cured (150 °C for 1 minute followed by 200 °C on a hotplate, as reported in the literature), one uncured, and one partially cured at 150 °C. This comparison aimed to assess how curing conditions—and thus film softness—affect bonding.

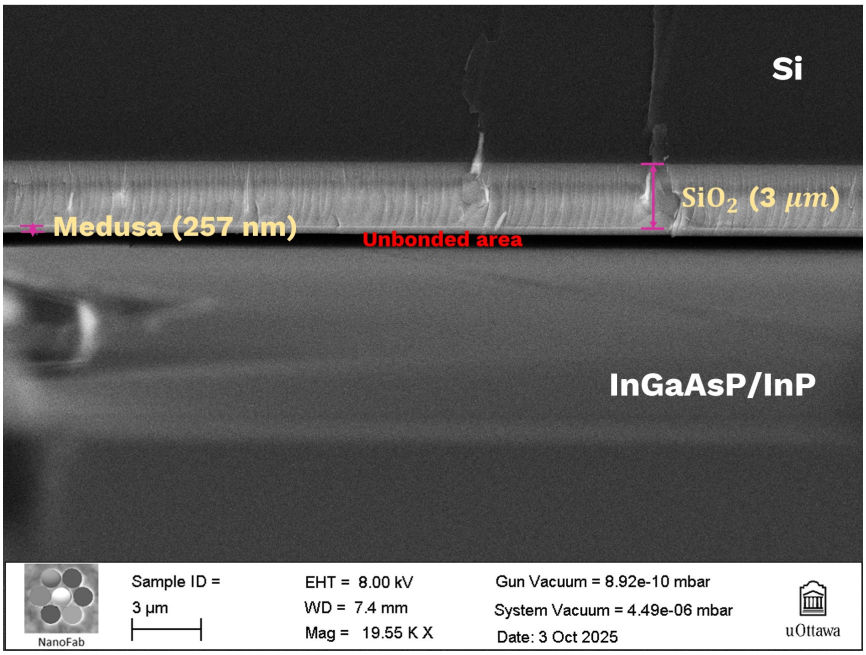


FIGURE 4.6: SEM images of the cross-section of SiO_2 bonded to InGaAsP using a Medusa intermediate adhesive layer, showing detachment of Medusa from the InGaAsP/InP wafer.

We applied the bonding conditions established during the final Al_2O_3-to-Al_2O_3 bonding trials described in the previous section. After bonding, the samples were diced to evaluate adhesion. The uncured and partially cured samples debonded during dicing, whereas the fully cured sample remained intact. However, cross-sectional analysis revealed that the Medusa layer had detached from the InGaAsP, leaving voids at the III–V/Medusa interface, as illustrated in Figure 4.6. In contrast, adhesion between the SiO_2 layers was strong and uniform. Additional bonding trials with increased force did not improve adhesion. Over time, the Medusa resist also exhibited degraded surface quality, likely due to nearing its expiration. Despite these challenges, this method remains promising for two key reasons. First, it requires minimal surface preparation compared to a direct bonding method. Second, upon annealing, Medusa converts into a glass-like SiO_2 layer, effectively forming a III–V–OI structure upon bonding to a III-V wafer. Unlike polymer adhesives such as Benzocyclobutene (BCB), whose thickness must be minimized to preserve optical confinement, a converted HSQ/Medusa layer would not significantly alter the ultimate optical device performance fabricated on III-V

-OI platform.

Rania Mahjoub, a PhD student in our group, and Dr. Shubhendra Kumar Jain, a former postdoctoral researcher in our group, investigated BCB bonding for InGaAsP-OI. During substrate removal using a hydrochloric acid (HCl) and phosphoric acid (H_3PO_4) etchant mixture, we observed delamination of the BCB layer, resulting in bond failure.

Future work should explore bonding immediately after spin coating HSQ or Medusa, as HSQ is known to cross-link upon air exposure and gradually transform into SiO_2, which may impact bonding quality. Building on this study, the following section transitions to the AlGaAs-on-insulator platform, focusing on GaAs substrate removal from pre-bonded samples provided by Sandia National Laboratories.

4.4 Substrate Removal for AlGaAs-OI

Realizing a III–V–OI material platform requires a sequence of fabrication steps, including epitaxial layer growth, wafer bonding, substrate thinning, complete substrate removal, and etch-stop layer removal as discussed in section 1.5.2 in Chapter 1. This section focuses on the substrate removal step, which precedes the final etch-stop layer removal process. Precise substrate removal while preserving the integrity of the III–V guiding layer is extremely important to realize the III-V-OI platforms. After mechanical thinning of the substrate by grinding or lapping to a few tens of micrometers, wet chemical etching—typically based on acid solutions—is used for further removal. This etching is generally performed in two stages: a fast initial etch, with high etch rate, followed by a slower and more controlled etch as the substrate thickness approaches a few hundred nanometers. The choice of the etch-stop layer, which is epitaxially grown on the substrate and positioned between the substrate and the III–V guiding layer, is essential for successful substrate removal. It must have a different composition from the substrate while remaining lattice-matched to enable high-quality epitaxial growth. In addition, it should be chemically resistant to the etchants used during substrate removal. Its thickness must be carefully optimized to ensure both high-quality growth and safe removal of the substrate without compromising the

guiding layer.

Material Stack	Etch-Stop	Thickness (nm)	Wet Etch	Substrate Removed
AlGaAs-OI [225]	$Al_{0.8}Ga_{0.2}As$	500	diluted HF (∼2.5%)	GaAs
[226]	AlAs	∼300	diluted HF	GaAs
[226]	$In_{0.5}Ga_{0.5}P$	∼300	HCl	GaAs
[227]	$Al_{0.3}Ga_{0.7}As$/ $Al_{0.85}Ga_{0.15}As$	100 / 30	H_2SO_4:H_2O_2:H_2O (1:2:160)	GaAs
[228]	AlAs	100	HF:H_2O (1:10)	GaAs
[229]	$Al_{0.5}In_{0.5}P$	500–1000	HF, HI, H_3PO_4, $C_6H_8O_7$	GaAs
InGaAsP-OI [230]	$In_{0.53}Ga_{0.47}As$	—	$FeCl_3$	InP
[26]	$In_{0.53}Ga_{0.47}As$	100	H_2O_2:H_3PO_4:H_2O (1:1:7)	InP

TABLE 4.1: A summary of commonly used etch-stop layers for efficient substrate removal in III–V–OI platforms.

Table 4.1 provides an overview of commonly used etch-stop layers for substrate removal in III–V–OI platforms, including their typical thicknesses, the wet etchants used for their removal, and the associated substrate materials. The next section describes a wet etching process developed for GaAs substrate. This is essential for realizing the AlGaAS -OI material platform that our group is interested in to develop high performance meta-waveguide structures for the nonlinear optics applications. The process was first optimized in terms of etch rate and surface roughness using unbonded AlGaAs/GaAs samples and subsequently applied to AlGaAs/GaAs bonded to SiO_2/Si samples. The results are presented in the following section.

4.5 GaAs slow etch

Wet etching of GaAs was carried out on an AlGaAs/GaAs sample with the layer stack shown in the Figure 4.7 (a). The sample was prepared from a wafer purchased for a previous project within the group. The etching process was optimized for a slow, controlled wet etch of the 100 nm GaAs capping layer in this structure. In addition, the experiments provided a preliminary assessment of selectivity toward the underlying $Al_{0.7}Ga_{0.3}As$ layer, which is one of the possible etch-stop layers in AlGaAs/GaAs heterostructures. A separate fast-etch recipe for GaAs removal was also tested using the thick GaAs substrate in the same stack, with a thickness of several hundred micrometers. Since the target etch rate was on the order of several hundred nanometers per minute, this substrate was the only available sample with sufficient thickness for evaluating such fast etching.

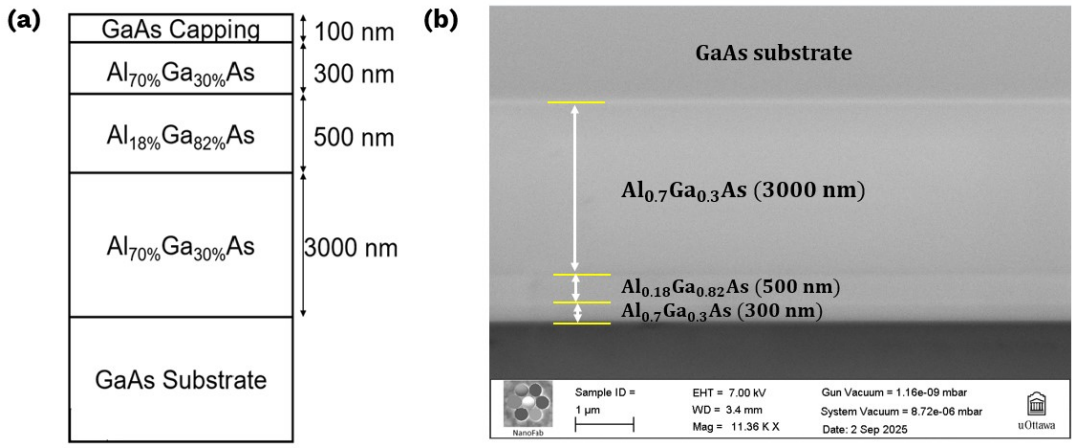


FIGURE 4.7: (a) AlGaAs/GaAs epitaxial stack used to optimize both fast and slow GaAs etching processes (b) Cross-sectional SEM images of the wet-etched sample, showing complete removal of the 100 nm GaAs layer beneath the underlying 300 nm-thick $Al_{0.7}Ga_{0.3}As$ layer.

For the slow-etch experiments, samples approximately 0.5 cm $\times$ 0.5 cm in size were cleaved from the 6-inch AlGaAs/GaAs wafer. The process began with sequential sonication in acetone, isopropanol, and DI water for 5 minutes each to remove organic contaminants, followed by nitrogen drying. The main etchant solution contained $C_6H_8O_7$:H_2O_2 in a 2:1 volume ratio. The

etching mechanism involves an oxidation-reduction reaction at the GaAs surface, where H_2O_2 acts as an oxidizing agent to form Ga–O and As–O bonds, while citric acid facilitates dissolution of the resulting oxide.

To prepare the etchant solution 10 grams of citric acid crystals were dissolved in 10 mL of DI water using magnetic stirring and/or sonication until a clear solution was obtained. Then 5 mL of H_2O_2 was added. Adding H_2O_2 to the citric acid solution helps reduce rapid peroxide decomposition, promotes more uniform heat distribution from the exothermic reaction, and improves safety by minimizing spattering. The solution was gently stirred and left briefly to reach thermal equilibrium. During this time, the samples were simultaneously immersed in a 30% NH_4OH/DI water solution (1:10 volume ratio) for 30 seconds. This step is used to remove native GaAs oxides and surface metal contaminants from the sample surface. After this, the samples were rinsed in DI water and dried with nitrogen.

The sample was then immersed in the etchant without agitation to ensure consistent and reproducible etching results. After each etch duration, some samples were quenched in DI water to stop the etch, then immediately immersed in a 30% NH_4OH/DI water solution (1:10 dilution) for 30–60 seconds, followed by a DI water rinse and nitrogen drying. Other samples were taken directly from the DI water rinse and dried with nitrogen without the additional NH_4OH step. The total etch time was varied between 12 and 30 minutes.

After the final N_2 drying step, the sample was cleaved in half to measure the remaining GaAs cap thickness and extract the etch rate. Cross-sectional SEM confirmed complete removal of the GaAs cap layer after 20 minutes of etching as shown in Figure 4.7 (b). The resulting etch rate was on the same order of magnitude as values reported in literature using a comparable citric acid to DI water chemistry [231]. AFM was used to evaluate surface roughness. The AFM image in Figure 4.8 shows a smooth AlGaAs surface with an RMS roughness of approximately 0.5 nm, with no observable etch residues present.

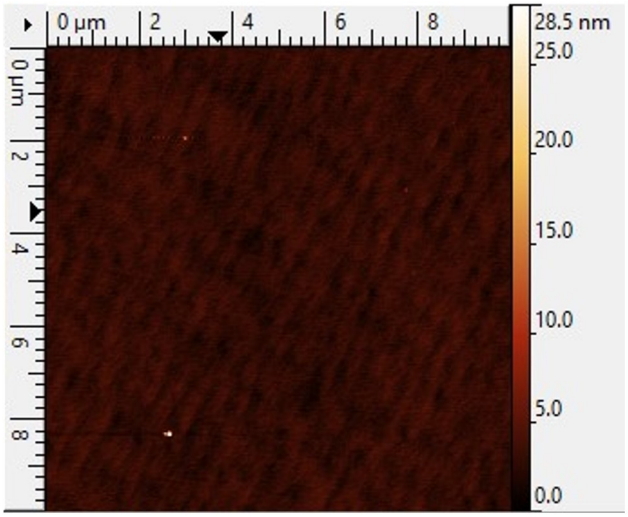


FIGURE 4.8: AFM images of the AlGaAs/GaAs sample following the slow etch and subsequent NH_4OH/DI water cleaning.

From the etch tests conducted under comparable conditions, samples removed directly from the DI water rinse and dried with N_2 —without the additional NH_4OH step—exhibited etch residues on the surface during visual inspection and showed a white, cloudy appearance on the etched surface. The residue could not be removed using standard cleaning with acetone or IPA, indicating that the immediate NH_4OH/DI water soak after a brief DI rinse is a critical step for achieving a smooth surface. For all etch tests, the etchant solution was freshly prepared since H_2O_2 can decompose over time (typically after 1–2 hours of storage), which may alter the etch rate and affect reproducibility of the etch results. NH_4OH/DI water solution was prepared in advance, stored in a glass bottle, and used when required. When the etch duration was increased to approximately 30 minutes, SEM imaging revealed no clear evidence of etching in the underlying AlGaAs layer, regardless of whether the NH_4OH/DI water rinse was applied after etching. This indicates that the process is selective for GaAs over $Al_{0.7}Ga_{0.3}As$.

4.6 GaAs fast etch recipe

Using the same wafer as in the slow etch experiments, the GaAs substrate side was placed upward in the etchant. The etching solution consisted of

$NH_4OH/H_2O_2/H_2O$ in a volume ratio of 5:5:133. After preparation, the solution was stirred with a glass rod for 3 minutes. A 0.5 × 0.5 cm sample with a measured thickness of 0.67 mm (verified using a vernier caliper) was used in etch test. Following standard cleaning, the sample was immersed in the etchant for 80 minutes. The etch was quenched by transferring the sample into DI water, followed by a DI water rinse and nitrogen blow-drying. All experiments were conducted at room temperature. The post-etch thickness was measured using a vernier caliper, yielding an etch rate of 0.33 μm/min. AFM analysis of the etched GaAs surface showed a surface roughness of approximately 10 nm, as shown in the Figure 4.9 (a).

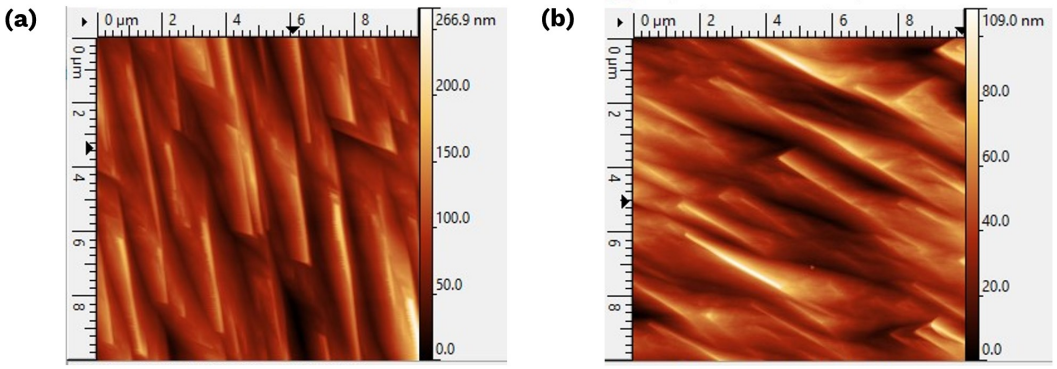


FIGURE 4.9: AFM images of the GaAs surface after the fast etch at (a) room temperature and (b) 32 °C.

When the etching temperature was increased to 32 °C under otherwise similar etch conditions, the etch rate increased to 1.2 μm/min, while the surface roughness increased slightly to 12 nm, as shown in the Figure 4.9 (b). Given the target of reducing the substrate thickness to 50 μm via grinding or lapping, we concluded that the observed etch rate and surface roughness is a good start for a rapid chemical thinning step prior to the slower citric-acid-based GaAs etch process for realizing the AlGaAs-OI platform. Further work could explore the selectivity of this etch recipe toward commonly used etch-stop layers in AlGaAs-OI platforms, such as AlAs, InGaP, and AlInP. In the next section, we discuss the application of this fast etch recipe to AlGaAs–SiO_2 bonded samples, where we explore its applicability to adhesion bonded structures.

4.7 Substrate removal in AlGaAs sample bonded to SiO_2

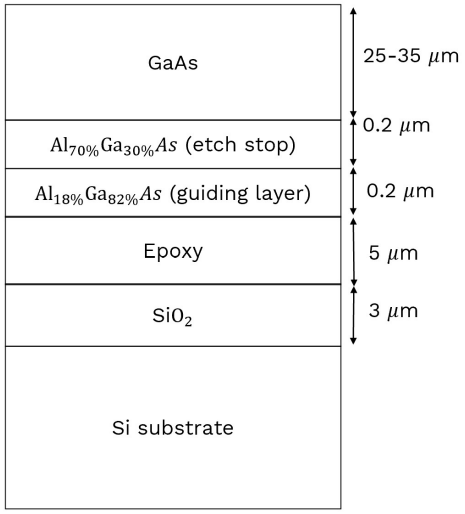


FIGURE 4.10: Illustration of the layer structure and individual layer thicknesses of the sample after substrate thinning.

This test was performed on two bonded samples received from the Center for Integrated Nanotechnologies (CINT) and Sandia National Laboratories. The layer structure of the samples is presented in the Figure 4.10. Epoxy was used as the adhesive to bond MOCVD-grown AlGaAs on a GaAs wafer, with an AlGaAs etch-stop layer, to thermally grown SiO_2 on a Si wafer. Each sample measured approximately 0.5 × 0.5 cm. The GaAs substrate was mechanically thinned by lapping and grinding. SEM images of the first sample cross-section revealed a variation in the remaining GaAs thickness from the edge to the center of the sample as shown in Figure 4.11. Around the edges, the GaAs thickness was approximately 25 µm, as shown in Figure 4.11 (a), while near the center it increased to approximately 35 µm, as shown in Figure 4.11 (b). This edge-dominant material removal during lapping may have resulted from sample, non-uniform pressure transfer from the mounting fixture, or uneven slurry distribution across the sample surface. The second sample exhibited significantly better thickness uniformity with approximately 42 µm of remaining GaAs near the edges and 43 µm near the center. Despite the substrate thickness variation after lapping, we proceeded with fast wet etching because it provided an opportunity to evaluate the chemical stability of the

epoxy used for bonding in the two received samples using the wet etching recipe previously optimized for unbonded samples.

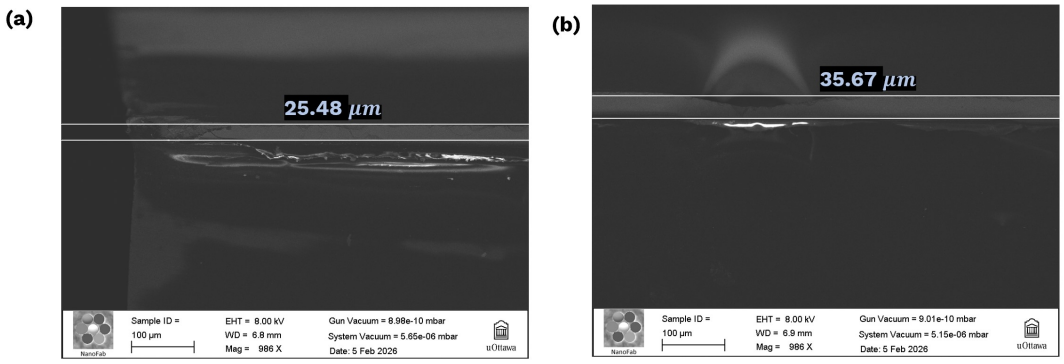


FIGURE 4.11: SEM images of the lapped sample viewed from the side, showing the thickness of the remaining substrate near (a) the edges and (b) the central region of the substrate.

The fast etch recipe was carried out at 32 °C for 15 minutes targeting 18 μm etch depth. Visual inspection after etching revealed epoxy leakage from the bonded interface in both samples. SEM analysis further confirmed slow seepage of epoxy from the bonding interface and epoxy delamination after wet etching, as shown in the Figures 4.12 (a) and (b) respectively. Representative SEM images are shown below. These results confirm that the epoxy is not chemically stable under the fast etching conditions, and bonding strength is weakened during wet etching. The bonding stack is therefore not compatible with the process flow that includes the wet etch step.

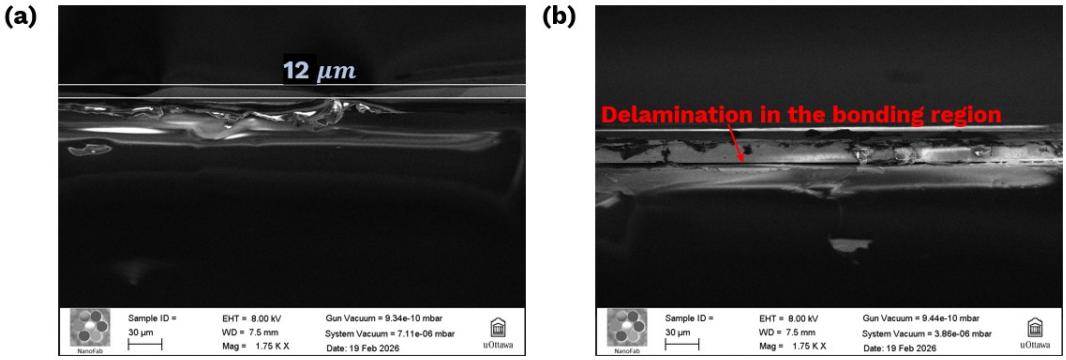


FIGURE 4.12: SEM images of the bonding region after wet etching, showing (a) epoxy seepage from the bonding region with approximately 12 µm of substrate remaining in Sample 1, and (b) epoxy delamination within the bonding region in Sample 2.

This highlights an important finding: bonding and etching cannot be treated as independent steps in the development of III–V–OI platforms. In adhesive bonding approaches, the adhesive becomes an integral part of the layer stack that is exposed to the etching environment. As a result, even if the bond demonstrates sufficient mechanical strength, it may still fail under chemical exposure.

This raises the question of the correct design strategy: should the adhesive be chosen to be compatible with the etching solution, or should the etching chemistry be adapted to the adhesive? The answer is both. However, in practice, the etch process is often constrained by material removal requirements such as selectivity and etch rate, which limits the extent to which the etching solution can be modified. Therefore, the primary constraint must generally be placed on the selection of the adhesive.

In summary, the experimental exploration of bonding methodologies for the InGaAsP platforms highlighted distinct physical and chemical trade-offs inherent to each technique. Standard direct SiO_2-to-SiO_2 bonding provided strong benchmark results on ideal surfaces, but attempting direct bonding with PECVD-deposited SiO_2 failed due to stringent surface roughness constraints. Similarly, Al_2O_3 bonding was hampered by persistent residues from

cleaving, while adhesive Medusa bonding faced processing delays and edge-bead accumulation that degraded interface uniformity. Furthermore, chemical substrate thinning experiments for AlGaAs-OI platform revealed severe epoxy degradation and seepage, proving that standard adhesive interfaces are incompatible with the aggressive chemical environments required for selective GaAs substrate removal. These failure modes establish clear process window for processing III-V-OI chips and provide a strong rationale for future development. In particular, extending HSQ-based adhesive bonding to the InGaAsP or AlGaAs-OI platforms—moving beyond its traditional application in SiC and GaN systems—offers a promising approach to overcome surface roughness limitations and establish a reliable path toward III-V-OI integration.

Chapter 5

Tuning Proximity Effect Correction for Fabrication of Metasurfaces

This chapter presents a study investigating proximity error correction (PEC) in the fabrication of plasmonic metasurfaces using electron-beam lithography (EBL). During EBL exposure, incoming high-energy electrons undergo scattering, resulting in short-range forward scattering within the resist and long-range backscattering from the underlying substrate. In dense nanoscale arrays such as plasmonic metasurfaces, forward scattering causes local beam broadening and corner rounding of antenna, while backscattered electrons deposit an accumulated background dose in inter-antenna gaps. To counteract these localized energy deposition profiles without the computational overhead or high-contrast dose-control demands of pixel-level dose modulation, PEC is achieved in the work presented in this chapter through shape modification of the antenna exposure pattern. Specifically, the local exposure footprint is tuned by adjusting the size of corrective square features added at critical points of the nano-antenna layout. The efficiency of this shape-modification approach is confirmed by the negligible shift in resonance between the calculated and measured optical transmission spectra of the metasurface.

This chapter is largely based on our previously published work, "Tuning proximity effect correction for plasmonic metasurfaces" [232]. I carried out the device fabrication and imaging, specifically executing the spin coating, EBL, metal evaporation, and SEM. The layout generation was a collaborative effort developed by Dr. Lais Fujii dos Santos, Ozan William Oner, and myself.

The numerical simulations and experimental measurements were conducted by Sina Aghili and Mohammadreza Mohammadpour.

5.1 PEC used for metasurface fabrication

The proximity effect correction method used in this work falls under the shape modification category, which is particularly important when patterning shapes with dimensions close to the critical dimension achievable by the EBL system. Shape modification techniques can be implemented through computational algorithms, such as Monte Carlo simulations, as seen in soft ware tools such as BEAMER and PYRAMID [126], [233], [128]. However, our approach adopts a non-computationally intensive shape modification method, making it suitable for any e-beam system, particularly where access to high-performance computing is limited. We follow the same approach of adding or removing squares along the edges, depending on the concavity, as shown in earlier work [234], but extend it further by varying the size of the squares. The decision of the optimum square size is embedded in the dose test routinely performed prior to patterning the final metasurface, and it changes depending on both the geometry and size of the antenna compared to the spot size of the electron beam. This geometry correction method is well suited for simple shapes with few 90° corners that can be manually corrected by the designer, and it is also shown to succeed for edges rotated with respect to the rectangular grid of the writing system. The goal of this work is to improve the fidelity between the designed and fabricated metasurface antennas by tuning this practical and adaptable proximity effect correction method, as demonstrated in this study.

5.2 Metasurface design and fabrication

The metasurface unit cell under study comprises four distinct orientations of the same antenna. Figure 5.1 (a) illustrates the unit cell, while Figure 5.1 (b) illustrates the dimensions of a single antenna. Each unit cell is repeated 280 times in both the vertical and horizontal directions, with a 1 μm pitch. We fabricated the metasurface using a 30 kV EBL system. The fabrication pro cess was carried out on borosilicate glass coated with a 125 nm thick

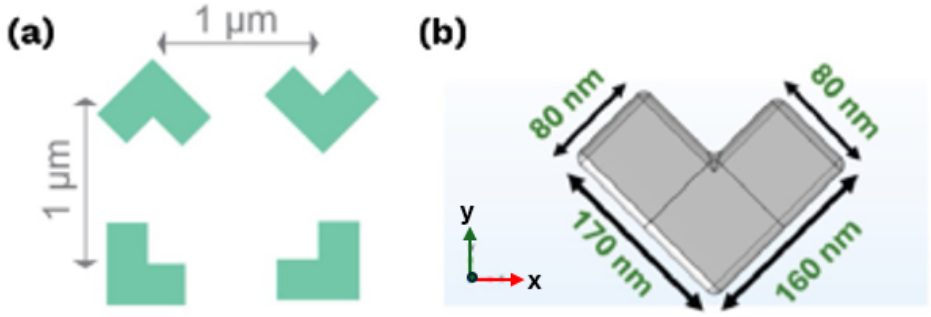


FIGURE 5.1: (a) Metasurface unit cell (not to scale). (b) Dimensions of a single antenna.

layer of PMMA resist. After the e-beam writing process, the sample was developed in tetramethylammonium hydroxide (TMAH). Subsequently, 3 nm of chromium and 30 nm of gold were deposited onto the sample using an evaporator, with chromium serving to enhance the adhesion of gold to the borosilicate glass. The lift-off process was then carried out in acetone for 5 h. A 20 nm layer of SiO_2 is evaporated on top of the gold metasurface. Finally, an additional 7 nm layer of gold was coated on samples destined for imaging to improve charge dissipation during scanning electron microscopy (SEM). Our EBL system performs a raster scan, so the total patterning time for the metasurface is fairly large (about 6 h). With this limitation in mind, a dose test is performed on a much smaller area before writing the complete metasurface. Keeping the base dose fixed, each shape is repeated 20 times with 10 variations of the dose factor, maintaining the pitch of the main pattern. Although the background dose accumulated in the smaller patterned area differs from that of the complete surface, each shape-dose pair is copied twice to detect inter shape proximity effects and account for unevenness in the substrate [235].

For proximity effect correction via shape modification in metasurface fabrication, the first step is to identify the critical regions of the nanoantenna that are subject to underexposure or overexposure. Figure 5.2 (a) shows SEM images of fabricated nanoantennae of different orientations without proximity effect correction. The four shapes shown in the picture were fabricated with the same dose and are the closest in size to the design. The contour of these shapes is approximately reproduced in Figure 5.2 (b), along with the

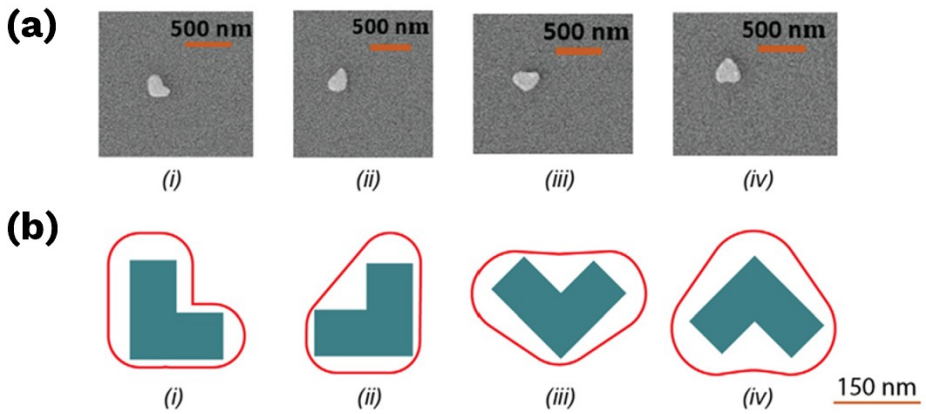


FIGURE 5.2: (a) SEM images of the fabricated nanoantennae without proximity-effect correction: (i) L-shaped, (ii) inverted L, (iii) V-shaped, (iv) inverted V-shaped antennae. (b) Comparison of the fabricated shapes with the intended design. The approximate contour of the shapes in (a) is shown in red, and the solid shapes represent the design.

intended design. Straight edges tend to accumulate more electrons toward the center of the line, while the convex corners are underexposed, resulting in larger and rounder shapes [236]. The triangular shape observed in three of the four shapes results from overexposure of the convex corner. As expected, the fabricated V and inverted V shapes are more distorted than the L and inverted L shapes due to the fracturing of 45° tilted lines in a rectangular grid. Since the distortions can be explained by intra shape proximity effects, the pitch was sufficiently large to avoid distortions caused by the patterning of neighboring shapes [235]. Our observations are consistent with previously reported results in the literature [234]. The six critical points identified in Figure 5.3 (a) are selected to perform proximity-effect correction, regardless of the antenna's orientation.

To correct for the proximity effects, we implemented shape modification, based on techniques reported before, by adding or removing square elements at these critical locations [234]. This approach is particularly well suited for corners aligned with the rectangular grid of the EBL system. We applied rotated square correction to the edges of the V and inverted V shapes to preserve the area in which the correction is applied, despite the additional processing overhead for fracturing them into smaller rectangles or squares [237].

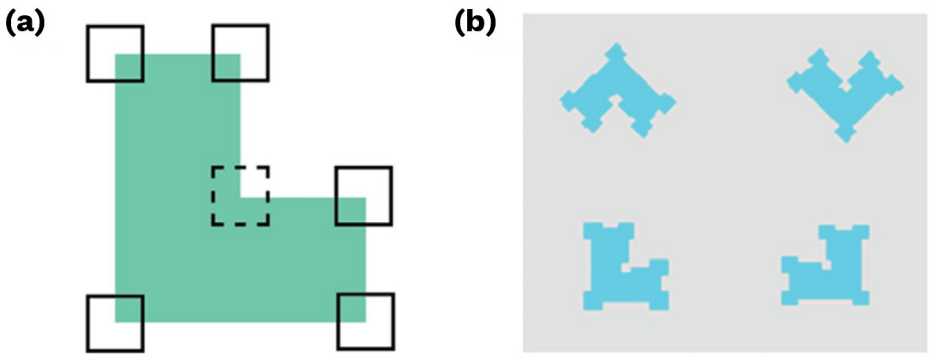


FIGURE 5.3: (a) Critical points of the antennae highlighted by black squares at the edges. Solid lines: enforce exposure. Dashed lines: reduce exposure. (b) A metasurface unit cell with the proximity-effect correction applied.

Figure 5.3 (b) presents an example of the e-beam lithography write pattern programmed for a metasurface unit cell with proximity effect correction applied.

5.3 Proximity effect correction tuning

To investigate the impact of proximity effect correction tuning on achieving antenna dimensions that closely match the design, we varied the size of the proximity-correction squares across a range of exposure doses for each of the shapes. Figure 5.4 shows the SEM image of the antennae for a fixed dose. The side of the squares for proximity effect correction was varied from 5 to 35 nm across the antennae from left to right. It is important to note that the area dose was kept constant for different proximity-effect correction values corresponding to each antenna. The necessity for proximity effect correction tuning is clearly demonstrated by the SEM images. As anticipated, increasing the proximity-effect correction square size helps preserve the sharp edges of the antennae as per the design. However,exceeding the optimal proximity-effect correction values results in overexposure, causing the edges to become rounded again.

We determined the optimal proximity-effect correction square value from the SEM images by measuring the antenna dimensions and comparing them with the design specifications. The chosen value for the side of the proximity

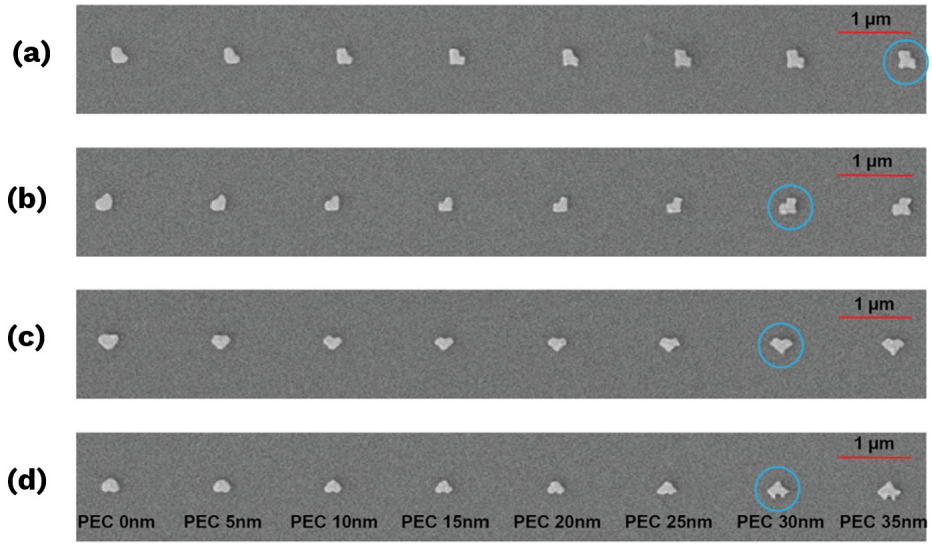


FIGURE 5.4: SEM images of the fabricated nanoantennae: (a) L-shaped, (b) inverted L, (c) V-shaped, (d) inverted V-shaped antennae. The antenna with optimum PEC is highlighted by a blue circle.

effect correction squares was 35 nm for L-shaped antennae, while V, inverted L, and inverted-V-shaped antennae required a 30 nm square size. The difference in the proximity error correction region required for the L-shaped antenna compared to other geometries indicates that the proximity-effect correction is, indeed, orientation-dependent. This arises primarily from the asymmetry between the feature layout and the cartesian writing grid of the electron beam [238].

Figure 5.5 shows the normalized transmission spectrum of the proximity corrected metasurface as a function of wavelength under linearly polarized illumination, obtained from both numerical analysis and experimental measurements carried out by Sina Aghili and Mohammadreza Mohammadpour. The modeling was carried out in COMSOL Multiphysics (version 6.2) [239]. The metasurface unit cell was excited with a y-polarized plane wave propagating along the z-direction; coordinates are defined in Figure 5.1. Periodic boundary conditions were applied along the x and y axes, while perfectly matched layers (PMLs) were introduced along the z-axis to suppress unwanted reflections. The reported spectra were calculated using plane-wave excitation.

Simulation conducted under Gaussian-beam excitation yielded similar results, with no observable differences in spectra across the tested beam parameters.

For the experimental measurements, a broadband super continuum laser was used as the source. The y-polarized incident light was focused onto the sample, and the transmitted light was collected through a fiber coupler. The transmitted light spectrum was analyzed using an OSA. Details of the experimental setup is presented in Appendix 7. The fidelity of the fabricated metasurface is confirmed by the measured resonance at 932 nm, which exhibits only a 1.5% shift compared to the resonance predicted by the numerical modeling. The amplitude differences observed in the normalized transmission originate from the idealized simulation conditions, where a plane wave excites an infinite periodic array, in contrast to the experimental case that employs a Gaussian beam. While the Gaussian profile serves as a good approximation to a plane wave—its peak spanning multiple unit cells—it is not perfectly equivalent. Furthermore, factors such as fiber losses and coupling imperfections also contribute to the measured discrepancies [234], [240].

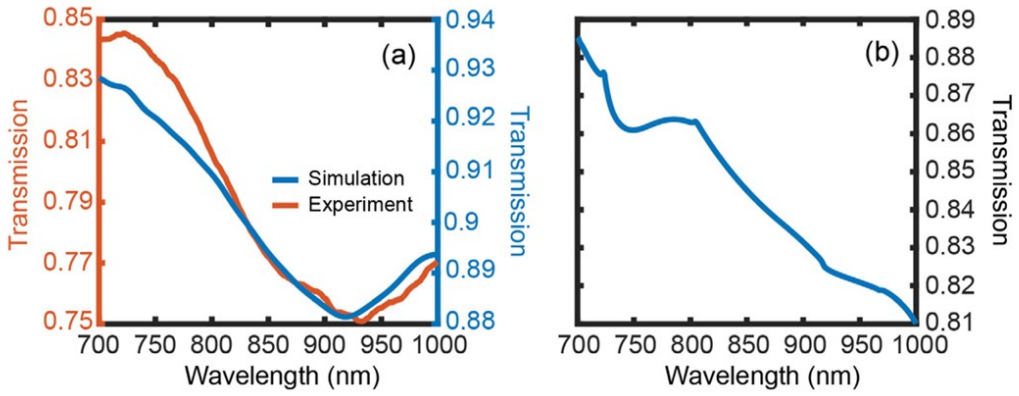


FIGURE 5.5: (a) Transmission response of the corrected fabricated (orange) and designed (blue) metasurface for incident linearly polarized light. (b) Simulated transmission for the uncorrected shapes.

As a measure of the necessity and success of the proximity effect correction for the studied metasurface, Figure 5.5 (b) shows the simulated transmission of the as-fabricated, uncorrected shapes outlined in Figure 5.2 (b). Notice

that, aside from the small dip at 750 nm, no resonances can be found in the same wavelength range as the original simulation presented in Figure 5.5 (a).

In conclusion, this chapter has presented a systematic investigation into the optimization of PEC through shape modification during the EBL nanofabrication of metasurfaces. Unlike the conventional approach that relies solely on dose adjustment, the work presented here demonstrates that tuning the size of the PEC elements is equally critical, alongside dose correction, in ensuring that the fabricated metasurface accurately reproduces the intended design geometry. Both the dose and the dimensions of the PEC elements were systematically tuned, and the corrected write patterns were validated through numerical simulations and experimental transmission measurements, with the close agreement between the two confirming the effectiveness of the correction strategy developed in this work. The findings further highlight that this tuning approach is particularly indispensable for lower kV EBL systems, where proximity effects are inherently more pronounced due to increased forward scattering. Importantly, the methodology presented here is not limited to the specific metasurface geometry investigated, but can be broadly extended to a wide range of metasurface designs, making it a practical and transferable framework for achieving accurate nanofabrication across diverse metasurface geometries and applications.

Chapter 6

Conclusion and Future Work

The development of III-V semiconductor-on-insulator (III–V-OI) platforms has opened new opportunities for nonlinear integrated photonics by combining the nonlinear optical properties of III–V semiconductors with the strong optical confinement achievable in high-refractive-index-contrast waveguides. Among these materials, InGaAsP is of particular interest for nonlinear optical devices operating at telecommunication wavelengths, including microring resonators for optical frequency-comb generation. However, the potential advantages of this material must be considered alongside the limitations imposed by two-photon absorption (TPA) and the associated free-carrier effects. In addition, the practical implementation of III-V-OI photonic platforms remains technologically challenging, requiring the development and optimization of reliable wafer bonding, substrate removal, and nanofabrication processes. These physical and technological challenges have motivated the research presented in this thesis.

The initial focus of this research was the theoretical investigation of optical frequency-comb generation in InGaAsP-on-insulator (InGaAsP-OI) microring resonators, with particular attention to the influence of TPA and free-carrier effects. At the time of this investigation, the free-carrier parameters required for the analysis, including carrier lifetime and free-carrier-induced refractive-index changes, were not sufficiently characterized for the InGaAsP composition under consideration. Consequently, the initial modeling relied on previously reported parameters for InP [162], a related III–V semiconductor material. This approach provided a reasonable starting point for evaluating the nonlinear performance of the proposed platform, but also introduced

uncertainty associated with the differences between the two material systems. The results of this original theoretical investigation were subsequently published in the Journal of the Optical Society of America B [62].

To address this uncertainty, the research was extended to the experimental investigation of free-carrier dynamics in InGaAsP/InP heterostructure waveguides. Although these structures differ from the proposed InGaAsP-OI devices, they provide a closer material representation than InP alone. The experimentally determined carrier lifetimes were subsequently incorporated into the theoretical analysis, leading to a more accurate assessment of frequency-comb generation in InGaAsP-OI microring resonators. The revised modeling indicated that frequency-comb generation may be achievable under the investigated conditions with active carrier extraction. Additional simulations of carrier extraction using reverse-biased p–n junctions demonstrated a possible route toward reducing free-carrier accumulation and improving nonlinear device performance. Thus, an important outcome of this research is the refinement of the initial theoretical predictions through the incorporation of experimentally obtained material parameters, providing a more realistic assessment of the nonlinear potential of InGaAsP-OI.

In parallel with these investigations, this thesis contributed to the ongoing development of InGaAsP-OI and AlGaAs-OI fabrication technologies. Since these platforms share several processing requirements, the experimental work addressed common challenges associated with wafer bonding, substrate removal, and interface integrity. Although a complete III–V-OI device fabrication process was not established, the experiments yielded useful intermediate results and identified processing limitations that can guide further development. A separate component of the thesis investigated proximity-effect correction in electron-beam lithography for the fabrication of plasmonic metasurfaces. This study addressed a broader nanofabrication challenge and resulted in an experimentally validated approach to improving the accuracy of nanoscale patterning. Taken together, the thesis contributions advance the understanding of nonlinear free-carrier effects in InGaAsP devices, provide practical insight into III–V-OI fabrication challenges, and demonstrate an additional nanofabrication methodology relevant to photonic structures.

The experimental free-carrier characterization yielded effective recombination lifetimes of 0.24 ns and 0.46 ns for the fundamental TM and TE modes, respectively, in InGaAsP/InP strip-loaded waveguides at 1550 nm. These measurements provide previously unavailable information about carrier recombination dynamics in an InGaAsP heterostructure closely related to the material system considered in the theoretical investigation.

Further simulations of carrier extraction under reverse bias indicate that reducing the effective carrier lifetime can provide benefits by mitigating free-carrier accumulation. Therefore, this work identifies it as a potential means of further improving device performance and expanding the range of conditions under which frequency-comb generation may be achieved.

While the experimental measurements provided more representative free-carrier lifetimes for the theoretical analysis, the predicted nonlinear performance of InGaAsP-OI microring resonators remains to be experimentally validated. Neither passive InGaAsP-OI microring resonators nor devices incorporating reverse-biased p–n junctions were fabricated and tested in this work. The additional numerical simulations of carrier extraction predicted an extraction time below 0.2 ps at an applied reverse bias of 5.0 V for the modeled junction configuration, but this result also remains to be verified experimentally. In the fabrication studies, several bonding configurations were successfully evaluated to varying degrees, but localized epoxy peeling during wet-etch substrate removal prevented the completion of the III–V-OI layer-transfer process.

Table 6.1 provides a comparative overview of the wafer-bonding approaches investigated in this work, summarizing the experimental outcomes and the principal processing limitations identified. The table also includes the proposed HSQ-based bonding approach as a possible direction for further investigation.

Bonding Method	Material Stack	Key Process / Parameters	Experimental Result	Primary Failure Mode / Bottleneck
Direct Oxide	SiO_2 to SiO_2 (Thermal)	Thermal oxide, direct contact	Successful	None (Strong bond energy on ideal surfaces)
Direct Oxide	SiO_2 to SiO_2 (PECVD)	PECVD oxide, direct contact	Failed	Post-deposition surface roughness
Alumina	Al_2O_3 to Al_2O_3	ALD deposition	Failed	Cleaving residues
Adhesive	InGaAsP (on InP) to SiO_2/Si	Spin-coated Medusa	Failed	Spin-to-bond delay
Adhesive (Proposed)	InGaAsP / AlGaAs to SiO_2	Spin-coated HSQ resist	Proposed	Resist aging constraints

TABLE 6.1: Summary of evaluated and proposed wafer-bonding approaches for III–V-OI platforms, including experimental outcomes and identified or anticipated processing limitations.

The fabrication investigations revealed several practical challenges associated with transferring III–V semiconductor layers onto insulating substrates. While successful direct bonding was demonstrated between thermally grown oxide surfaces, other bonding configurations were limited by surface roughness, contamination, or process-dependent constraints. In addition, the difficulties encountered during substrate removal demonstrated that obtaining a bonded interface does not necessarily ensure its integrity throughout the subsequent fabrication sequence. These observations emphasize the importance of considering surface preparation, bonding conditions, material compatibility, and substrate removal as interconnected stages of the fabrication process. Although the experiments did not culminate in a complete III–V-OI platform, they identified specific processing limitations and provided practical guidance for improving the reproducibility and reliability of future fabrication attempts.

An additional contribution of this thesis concerns the optimization of proximity-effect correction for the fabrication of plasmonic metasurfaces using electron-beam lithography. Building upon an established shape-modification approach, this study investigated how the dimensions of corrective features introduced at critical locations of nanoantenna patterns influence the accuracy of the fabricated structures. The method was experimentally validated by comparing the fabricated geometries and optical transmission response with the original design, demonstrating improved pattern fidelity without the need for computationally intensive proximity-effect simulations. Although this investigation was conducted independently of the III–V-OI platform development, it addresses a broader challenge in photonic nanofabrication: achieving reliable reproduction of nanoscale geometries using accessible electron-beam lithography systems.

Bridging these present findings with practical nonlinear photonic technologies requires a clear, step-by-step development roadmap. In the immediate term, nanofabrication efforts must focus on resolving interfacial bonding yield across III-V platforms. HSQ-based intermediate bonding, adapted from approaches developed for GaN and SiC processing, represents a possible alternative to the investigated adhesive bonding methods and warrants further experimental evaluation. Similarly, additional investigations of ALD Al_2O_3 direct bonding should focus on improving surface preparation and minimizing contamination and residues introduced during sample cleaving and subsequent processing.

Building upon the revised theoretical predictions obtained using experimentally measured carrier lifetimes, an important next step is the fabrication and experimental characterization of p-n junction integrated InGaAsP-OI microring resonators designed for frequency-comb generation. Such experiments would allow direct validation of the predicted nonlinear device behavior and provide further insight into the influence of TPA, free-carrier absorption, and carrier-induced refractive-index changes on resonator performance. Moreover, The benefits of carrier extraction must be evaluated alongside possible increases in linear optical losses resulting from doping and junction integration.

In the longer term, successful development of low-loss InGaAsP-OI photonic

devices could enable a range of nonlinear optical applications, including compact frequency-comb sources for wavelength-division multiplexing and integrated optical signal processing. The results of this thesis suggest that the nonlinear potential of this platform may be more favorable than initially predicted, although realizing these applications will require further progress in material characterization, fabrication, dispersion engineering, and experimental device validation. The continued development of related III–V-OI platforms, including AlGaAs-OI, may also provide opportunities for exploring other nonlinear processes and wavelength ranges.

Overall, this thesis has advanced the understanding of free-carrier effects in InGaAsP nonlinear photonic devices by connecting theoretical predictions with experimentally measured carrier dynamics. An important finding is that replacing estimated material parameters with more representative experimental values can substantially change the predicted feasibility of nonlinear device operation. In parallel, the fabrication studies have identified practical challenges and processing considerations relevant to the development of III–V-OI photonic platforms. While several technological and experimental milestones remain to be achieved, the results presented here provide a foundation for continued research toward practical nonlinear III–V-on-insulator photonic devices.

Chapter 7

Metasurface Optical Transmission Measurement Setup

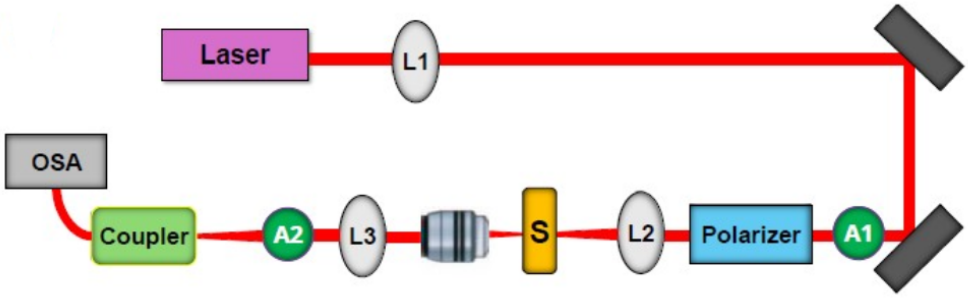


FIGURE 7.1: Schematic of the linear experimental setup.

The schematic of the linear setup used to measure the transmission spectrum of the metasurface is shown in Figure 7.1. A broadband supercontinuum laser source was used to measure the transmission resonances of the sample. The diverging light from the source was first collimated using lens L1, and then directed along the main optical axis using two mirrors. A polarizer was placed after the mirrors to fix the polarization state of the incident light. Two apertures (A1 and A2) were used to ensure that the beam propagated precisely along a straight path. The collimated beam was then focused onto the sample using lens L2 with a focal length of 5 cm, ensuring that the light covered the entire sample area and provided a high signal-to-noise ratio. The transmitted light was subsequently collected and collimated by a microscope objective with a focal length of 1.7 cm. Finally, the collimated

transmitted light was coupled into a fiber coupler and directed to an OSA to record the transmission spectrum. We used a single-mode fiber with a numerical aperture of 0.39 to direct the light to OSA. For coupling light into the fiber, the numerical aperture of the incident beam should not exceed that of the fiber

$$\mathrm{NA}_{\mathrm{beam}} \leq \mathrm{NA}_{\mathrm{fiber}}. \tag{7.1}$$

The beam's numerical aperture is defined as

$$\mathrm{NA}_{\mathrm{beam}} = n \sin\theta, \tag{7.2}$$

where θ is the half-angle of the beam's convergence cone relative to the fiber axis, and n is the refractive index of the surrounding medium. For coupling in air, $n \approx 1$, yielding

$$\theta \leq \sin^{-1}(0.39) \approx 22.95^{\circ}. \tag{7.3}$$

Thus, the convergence half-angle at the fiber entrance should not exceed approximately 23°. Efficient coupling also requires matching the focused beam to the fiber's mode-field size and ensuring proper alignment.

Additional angular limitations can arise from the incidence angle on the metasurface and the optical components along the propagation path. We therefore aligned the beam approximately normal to the sample and to the relevant surfaces of the polarizer and lenses while centering it through the apertures. This alignment was intended to minimize angle-dependent changes in transmission. The beam's angular spread at the sample and the acceptance angle of the collection optics also affect the transmitted light reaching the detector.

Chapter 8

Lugiato-Lefever Equation and Split-Step Fourier Transform

8.1 Maxwell's equation and Nonlinear Wave Equation

Understanding propagation of light in a microring resonator begins with Maxwell's equations in a non-magnetic dielectric medium given by

$$\nabla \times \mathbf{E} = -\frac{\partial \mathbf{B}}{\partial t}, \tag{8.1}$$

$$\nabla \times \mathbf{H} = \frac{\partial \mathbf{D}}{\partial t} + \mathbf{J}_{\text{fc}}, \tag{8.2}$$

$$\nabla \cdot \mathbf{D} = 0, \tag{8.3}$$

$$\nabla \cdot \mathbf{B} = 0, \tag{8.4}$$

where $\mathbf{J}_{\text{fc}}$ is the current density generated by photo-induced free electron-hole pairs [9]. The electric displacement field relates to the electric field via the constitutive relation where total polarization consists of linear and nonlinear contributions given by

$$\mathbf{D} = \epsilon_0 \mathbf{E} + \mathbf{P}, \tag{8.5}$$

$$\mathbf{P} = \mathbf{P}_{\text{L}} + \mathbf{P}_{\text{NL}}. \tag{8.6}$$

Taking the curl of Equation (8.1) and applying vector identities under transverse wave propagation yields [9]

$$\nabla(\nabla \cdot \mathbf{E}) - \nabla^2 \mathbf{E} = -\mu_0 \frac{\partial^2 \mathbf{D}}{\partial t^2} - \mu_0 \frac{\partial \mathbf{J}_{\text{fc}}}{\partial t}, \tag{8.7}$$

$$\nabla^2 \mathbf{E} - \mu_0 \epsilon_0 \epsilon_r \frac{\partial^2 \mathbf{E}}{\partial t^2} = \frac{1}{\epsilon_0 c^2} \frac{\partial^2 \mathbf{P}_{\text{NL}}}{\partial t^2} + \mu_0 \frac{\partial \mathbf{J}_{\text{fc}}}{\partial t}. \tag{8.8}$$

For a centrosymmetric semiconductor medium, second-order nonlinear optical susceptibility vanishes. Considering third-order optical nonlinearity, the nonlinear polarization is governed by the complex susceptibility tensor $\chi^{(3)}$ as [9]

$$\mathbf{P}_{\text{NL}} = \epsilon_0 \chi^{(3)} \mathbf{E}^3, \tag{8.9}$$

where $\chi^{(3)}$ can be written as

$$\chi^{(3)} = \text{Re}\{\chi^{(3)}\} + i\,\text{Im}\{\chi^{(3)}\}. \tag{8.10}$$

To evaluate the nonlinear polarization, we select a real, linearly polarized CW optical field oscillating at a single angular frequency (ω) represented as

$$\mathbf{E}(t) = E_0 \cos(\omega t). \tag{8.11}$$

Substituting this field into Equation (8.9) gives

$$\mathbf{E}^3(t) = E_0^3 \cos^3(\omega t). \tag{8.12}$$

Using the trigonometric power-reduction identity $\cos^3(\theta) = \frac{3}{4}\cos(\theta) + \frac{1}{4}\cos(3\theta)$, the cubic field expansion becomes

$$\mathbf{E}^3(t) = \frac{E_0^3}{4}\left[3\cos(\omega t) + \cos(3\omega t)\right], \tag{8.13}$$

$$\mathbf{P}_{\text{NL}}(t) = \epsilon_0 \chi^{(3)} \frac{E_0^3}{4}\left[3\cos(\omega t) + \cos(3\omega t)\right]. \tag{8.14}$$

Neglecting the non-phase-matched third-harmonic component and retaining only the fundamental frequency component yields

$$\mathbf{P}_{\mathrm{NL}}^{(\omega)}(t) = \frac{3}{4}\epsilon_0 \chi^{(3)} E_0^2 \mathbf{E}(t). \tag{8.15}$$

The optical intensity is defined by the time-averaged Poynting vector magnitude as

$$I = \frac{1}{2}\epsilon_0 c n_0 E_0^2, \tag{8.16}$$

therefore

$$E_0^2 = \frac{2I}{\epsilon_0 c n_0}. \tag{8.17}$$

Substituting Equation (8.17) into Equation (8.15) expresses nonlinear polarization in terms of intensity as

$$\mathbf{P}_{\mathrm{NL}}^{(\omega)} = \frac{3\chi^{(3)} I}{2cn_0}\mathbf{E}. \tag{8.18}$$

Taking the second time derivative of Equation (8.18) and substituting it into the Equation (8.8) gives

$$\frac{1}{\epsilon_0 c^2}\frac{\partial^2 \mathbf{P}_{\mathrm{NL}}^{(\omega)}}{\partial t^2} = -\frac{3\chi^{(3)} I \omega^2}{2\epsilon_0 c^3 n_0}\mathbf{E}. \tag{8.19}$$

Combining linear and nonlinear polarization terms on the left-hand side of Equation (8.8) yields

$$\nabla^2 \mathbf{E} + \mu_0 \epsilon_0 \epsilon_r \omega^2 \mathbf{E} + \frac{3\chi^{(3)} I \omega^2}{2\epsilon_0 c^3 n_0}\mathbf{E} = -\mu_0 \frac{\partial \mathbf{J}_{\mathrm{fc}}}{\partial t}. \tag{8.20}$$

Using $\mu_0 \epsilon_0 = 1/c^2$ and $\epsilon_r = n_0^2(\omega)$, we group the terms under a single intensity-dependent effective permittivity

$$\nabla^2 \mathbf{E} + \frac{\omega^2}{c^2}\left[n_0^2(\omega) + \frac{3\chi^{(3)} I}{2\epsilon_0 c n_0(\omega)}\right]\mathbf{E} = -\mu_0 \frac{\partial \mathbf{J}_{\mathrm{fc}}}{\partial t}. \tag{8.21}$$

Defining the complex intensity-dependent refractive index $n(\omega, I)$ as

$$n^2(\omega, I) = n_0^2(\omega) + \frac{3}{2}\frac{\chi^{(3)} I}{\epsilon_0 c n_0(\omega)}, \tag{8.22}$$

Equation (8.21) becomes

$$\nabla^2\mathbf{E} - \frac{n^2(\omega, I)}{c^2}\frac{\partial^2\mathbf{E}}{\partial t^2} = -\mu_0\frac{\partial\mathbf{J}_{\text{fc}}}{\partial t}. \tag{8.23}$$

8.1.1 Free Carrier Dynamics and Spatial Mode Separation

The motion of photo-generated free carriers induces a macroscopic current density $\mathbf{J}_{\text{fc}} = e\mu_c N_c\mathbf{E}$, consisting of electron-hole pairs ($N_c = \Delta N_e = \Delta N_h$), e is the elementary charge, and μ_c is the carrier mobility.

According to Drude theory, the presence of these free carriers alters both the FCA and the FCD of the semiconductor medium [9]

$$\Delta\tilde{n}_{\text{fc}} = \Delta n_{\text{fc}} + i\frac{\alpha_{\text{fc}}}{2k_0} = -\frac{e^2N_c}{2n_0\epsilon_0\omega_p^2}\left(\frac{1}{m_e^*} + \frac{1}{m_h^*}\right) + i\frac{\sigma}{2k_0}N_c. \tag{8.24}$$

Here, N_c is the volumetric free-carrier density (m^{-3}), σ is the free-carrier absorption cross-section (m^2), which quantifies the optical attenuation per unit length per unit free carrier (often denoted as σ_{fca} in literature such as Lau et al., where $\alpha_{\text{fc}} = \sigma N_c$), and Δn_{fc} is the free-carrier dispersion perturbation ($\Delta n_{\text{fc}} = -k_c N_c = -\left|\frac{dn}{dN_c}\right| N_c$).

The dimensionless plasma dispersion parameter μ can be defined as the ratio of FCD (phase shift) to FCA (loss) as [9]

$$\mu = \frac{2k_0\Delta n_{\text{fc}}}{\alpha_{\text{fc}}} = \frac{2k_0\Delta n_{\text{fc}}}{\sigma N_c} = \frac{2k_0k_c}{\sigma} \tag{8.25}$$

where $k_c = \left|\frac{dn}{dN_c}\right|$ is the FCD coefficient (m^3) used in literature [9]. This allows the total free-carrier contribution to be written compactly as a complex propagation shift

$$\Delta\beta_{\text{fc}} = -\frac{\sigma}{2}(1 + i\mu)N_c. \tag{8.26}$$

Note that factoring out $-\frac{\sigma}{2}N_c$ reveals the two individual physical mechanisms

$$-\frac{\sigma}{2}(1 + i\mu)N_c = -\frac{\sigma}{2}N_c - ik_0k_cN_c = -\frac{\alpha_{\text{fc}}}{2} - ik_0\Delta n_{\text{fc}}$$

. To solve the wave equation in waveguide coordinates, we transform to the frequency domain using a separable modal ansatz

$$\tilde{\mathbf{E}}(x,y,z,\omega) = F(x,y)\tilde{A}(z,\omega-\omega_p)e^{i(\beta_0 z-\omega_p t)}. \tag{8.27}$$

Decomposing the Laplacian operator into transverse and longitudinal components yields

$$\nabla^2\tilde{\mathbf{E}} = \left[\tilde{A}\nabla_\perp^2 F + F\left(2i\beta_0\frac{\partial\tilde{A}}{\partial z} - \beta_0^2\tilde{A} + \frac{\partial^2\tilde{A}}{\partial z^2}\right)\right]e^{i(\beta_0 z-\omega_p t)}. \tag{8.28}$$

Applying the Slowly Varying Envelope Approximation (SVEA) isolates spatial envelope evolution

$$i\frac{\partial\tilde{A}}{\partial z} + (\beta-\beta_0)\tilde{A} = 0 \tag{8.29}$$

Expanding the propagation constant around the carrier frequency including dispersion, Kerr nonlinearity, TPA, and FC effect we write [9]

$$\beta(\omega) = \beta_0 + \sum_{k=1}^{\infty}\frac{\beta_k}{k!}(\omega-\omega_p)^k + \Delta\beta_{\mathrm{NL}} + \Delta\beta_{\mathrm{fc}} \tag{8.30}$$

$$\Delta\beta_{\mathrm{NL}} = \left(\gamma + i\frac{\beta_{\mathrm{TPA}}}{2A_{\mathrm{eff}}}\right)|A|^2 - i\frac{\alpha}{2} \tag{8.31}$$

$$\gamma = \frac{3\omega_p \mathrm{Re}\{\chi^{(3)}\}}{2\epsilon_0 c^2 n_0^2 A_{\mathrm{eff}}} = \frac{n_2\omega_p}{cA_{\mathrm{eff}}} \tag{8.32}$$

$$\beta_{\mathrm{TPA}} = \frac{3\omega_p \mathrm{Im}\{\chi^{(3)}\}}{2\epsilon_0 c^2 n_0^2} \tag{8.33}$$

$$A_{\mathrm{eff}} = \frac{\left(\iint |F|^2\,dxdy\right)^2}{\iint |F|^4\,dxdy} \tag{8.34}$$

Substituting the expanded propagation constant into Equation (8.29) yields

$$i\frac{\partial\tilde{A}}{\partial z} + \left(\sum_{k=1}^{\infty}\frac{\beta_k}{k!}(\omega-\omega_p)^k + \left(\gamma + i\frac{\beta_{\mathrm{TPA}}}{2A_{\mathrm{eff}}}\right)|A|^2 - \frac{\sigma}{2}(1+i\mu)N_c - i\frac{\alpha}{2}\right)\tilde{A} = 0 \tag{8.35}$$

Applying the inverse Fourier transform mapping $(\omega - \omega_p) \longrightarrow i\frac{\partial}{\partial t}$ yields the temporal differential equation in laboratory coordinates

$$i\frac{\partial A}{\partial z} + \beta_1\left(i\frac{\partial A}{\partial t}\right) + \sum_{k=2}^{\infty}\frac{\beta_k}{k!}\left(i\frac{\partial}{\partial t}\right)^k A + \left(\gamma + i\frac{\beta_{\text{TPA}}}{2A_{\text{eff}}}\right)|A|^2 A \\ -\frac{\sigma}{2}(1+i\mu)N_c A - i\frac{\alpha}{2}A = 0 \tag{8.36}$$

Rearranging terms to isolate the spatial derivative we get

$$\frac{\partial A}{\partial z} + \beta_1\frac{\partial A}{\partial t} = -\frac{\alpha}{2}A + i\sum_{k=2}^{\infty}\frac{\beta_k}{k!}\left(i\frac{\partial}{\partial t}\right)^k A + i\gamma|A|^2 A \\ -\frac{\beta_{\text{TPA}}}{2A_{\text{eff}}}|A|^2 A - \frac{\sigma}{2}(1+i\mu)N_c A \tag{8.37}$$

To eliminate linear group delay, we transform coordinates to a co-moving frame at group velocity $v_g = 1/\beta_1$ using fast time T. Fast time coordinate T in a single round trip is defined as

$$T = t - \frac{z}{v_g} = t - \beta_1 z, \tag{8.38}$$

$$\frac{\partial}{\partial t} = \frac{\partial}{\partial T}, \tag{8.39}$$

and

$$\frac{\partial}{\partial z} = \frac{\partial}{\partial z}\bigg|_T - \beta_1\frac{\partial}{\partial T} \tag{8.40}$$

Substituting Equations (8.39) and (8.40) into Equation (8.37) cancels the linear delay term, yielding the internal 1D propagation equation [9]

$$\frac{\partial A}{\partial z}\bigg|_{\text{internal}} = -\frac{\alpha}{2}A + i\sum_{k\geq 2}\frac{\beta_k}{k!}\left(i\frac{\partial}{\partial T}\right)^k A + i\gamma|A|^2 A \\ -\frac{\beta_{\text{TPA}}}{2A_{\text{eff}}}|A|^2 A - \frac{\sigma}{2}(1+i\mu)N_c A \tag{8.41}$$

Equation (8.41) constitutes the generalized nonlinear Schrödinger equation accounting for linear propagation loss (α), group-velocity dispersion (β_k), Kerr nonlinearity (γ), TPA (β_{TPA}), and FC effect mediated by the free-carrier

density N_c. This equation serves as the foundational intracavity propagation model used subsequently to construct the boundary conditions for the Lugiato–Lefever equation.

8.2 Cavity Dynamics & Formulation of the Extended LLE

To describe intra-cavity dynamics in a micro-ring resonator of length $L = 2\pi r$ evanescently coupled to a bus waveguide, we model round-trip circulation using mean-field cavity theory [241], [242], [243].

The boundary condition relating circulating field envelopes across consecutive round trips m is [241]

$$A_2^{(m)} = \sqrt{\theta} A_{\text{in}}^{(m-1)} + \sqrt{1-\theta}\, A_5^{(m-1)} e^{i\phi}. \tag{8.42}$$

$$\phi = \delta_0 = (\omega_p - \omega_{\text{res}}) \frac{L n_g}{c}. \tag{8.43}$$

Under the mean-field approximation, the field envelope evolves gradually over a single round trip, expanded as [242]

$$A_5^{(m-1)} \approx A_2^{(m-1)} + L \left.\frac{\partial A_2}{\partial z}\right|_{\text{internal}}. \tag{8.44}$$

Substituting Equation (8.44) into the boundary condition gives:

$$A_2^{(m)} = \sqrt{\theta} A_{\text{in}}^{(m-1)} + \sqrt{1-\theta}\, e^{i\phi} \left(A_2^{(m-1)} + L \left.\frac{\partial A_2}{\partial z}\right|_{\text{internal}} \right). \tag{8.45}$$

Assuming low losses in the cavity, expanding the coupling transmission and phase factors to first order yields

$$\sqrt{1-\theta}\, e^{i\phi} \approx \left(1 - \frac{\theta}{2}\right)(1 + i\phi) \approx 1 - \frac{\theta}{2} + i\phi, \tag{8.46}$$

$$A_2^{(m)} = \sqrt{\theta} A_{\text{in}}^{(m-1)} + \left(1 - \frac{\theta}{2} + i\phi\right) A_2^{(m-1)} + L \left.\frac{\partial A_2}{\partial z}\right|_{\text{internal}}. \tag{8.47}$$

Dividing the round-trip change by round-trip travel time $t_R = L/v_g$ defines the slow-time derivative [241], [242]

$$t_R \frac{\partial A}{\partial t} = \sqrt{\theta} A_{\text{in}} + \left(-\frac{\theta}{2} + i\delta_0 \right) A + L \left. \frac{\partial A}{\partial z} \right|_{\text{internal}}. \tag{8.48}$$

Here, t denotes the physical slow time tracking the slow envelope dynamics across multiple cavity round trips. Substituting the internal spatial derivative from Equation (8.41) into Equation (8.48) yields

$$t_R \frac{\partial A}{\partial t} = \sqrt{\theta} A_{\text{in}} - \left(\frac{\theta + \alpha L}{2} - i\delta_0 \right) A + L \left[i \sum_{k \geq 2} \frac{\beta_k}{k!} \left(i \frac{\partial}{\partial T} \right)^k A \right.$$
$$\left. + i\gamma |A|^2 A - \frac{\beta_{\text{TPA}}}{2A_{\text{eff}}} |A|^2 A - \frac{\sigma}{2}(1 + i\mu) N_c A \right]. \tag{8.49}$$

Defining total cavity loss as $\alpha' = \frac{\theta + \alpha L}{2}$

$$t_R \frac{\partial A}{\partial t} = \sqrt{\theta} A_{\text{in}} - (\alpha' - i\delta_0) A + L \left[i \sum_{k \geq 2} \frac{\beta_k}{k!} \left(i \frac{\partial}{\partial T} \right)^k A + i\gamma |A|^2 A \right.$$
$$\left. - \frac{\beta_{\text{TPA}}}{2A_{\text{eff}}} |A|^2 A - \frac{\sigma}{2}(1 + i\mu) N_c A \right]. \tag{8.50}$$

Restricting dispersion operators to second-order derivative

$$\left(i \frac{\partial}{\partial T} \right)^2 = -\frac{\partial^2}{\partial T^2}, \tag{8.51}$$

Substituting Equations (8.51) into Equation (8.50) yields

$$t_R \frac{\partial A(t,T)}{\partial t} = \sqrt{\theta} A_{\text{in}} - (\alpha' - i\delta_0) A - i \frac{\beta_2 L}{2} \frac{\partial^2 A}{\partial T^2} + i\gamma L |A|^2 A$$
$$- \frac{\beta_{\text{TPA}} L}{2A_{\text{eff}}} |A|^2 A - \frac{\sigma L}{2}(1 + i\mu) N_c A. \tag{8.52}$$

Simplifying complex factors produces the explicit dimensional Lugiato–Lefever Equation with TPA, FCA, and FCD gives

$$t_R\frac{\partial A}{\partial t} = \sqrt{\theta}A_{\text{in}} + A\Bigg[-\alpha' + i\delta_0 - i\frac{\beta_2 L}{2}\frac{\partial^2}{\partial T^2} + i\gamma L|A|^2 - \frac{\beta_{\text{TPA}}L}{2A_{\text{eff}}}|A|^2 - \frac{\sigma L}{2}(1+i\mu)N_c\Bigg]. \tag{8.53}$$

The free-carrier density N_c is calculated by solving the rate equation in the fast time domain

$$\frac{\partial N_c(t,T)}{\partial T} = \frac{\pi\beta_{TPA}}{2h\omega_p A_{\text{eff}}^2}|A(t,T)|^4 - \frac{N_c(t,T)}{\tau_c}, \tag{8.54}$$

Here τ_c is the FC lifetime [167].

Equation (8.54) must be solved together with the rapid time dependence T of the LLE at each step in the slow time variable t. Since the pump is CW, $A(t,T)$ remains constant for all T, and the solution to Equation (8.54) is

$$N_c = \frac{\pi\beta_{\text{TPA}}|A|^4\tau_c}{2h\omega_p A_{\text{eff}}^2}. \tag{8.55}$$

Therefore, Equation(8.53) can be expressed as

$$t_R\frac{\partial A}{\partial t} = \sqrt{\theta}A_{\text{in}} + A\Bigg[-\alpha + i\delta_0 + \frac{iL\beta_2}{2}\left(\frac{\partial}{\partial T}\right)^2 + iL\gamma|A|^2 - \frac{\beta_{\text{TPA}}}{2A_{\text{eff}}}L|A|^2 - \frac{\sigma L}{2}(1+i\mu)\left(\frac{\pi\beta_{\text{TPA}}}{2h\omega_p A_{\text{eff}}^2}\right)|A|^4\tau_c\Bigg]. \tag{8.56}$$

This represents the LLE equation in diamentional form.

8.3 Normalization of the Lugiato-Lefever Equation

To obtain the normalized LLE used in the numerical simulation from Equation (8.56), the physical field is transformed into the dimensionless field ψ

given by

$$\psi(\tau, \xi) = A(t, T)\sqrt{\frac{2\gamma L}{\alpha}}, \tag{8.57}$$

where ψ is the normalized intracavity field used in the split-step Fourier simulation.

The slow time coordinate is normalized by the cavity loss rate

$$\tau = \frac{\alpha}{t_R} t, \tag{8.58}$$

where one unit of normalized slow time corresponds to the evolution over one photon lifetime of the resonator.

The fast-time coordinate is normalized according to the convention used in the numerical implementation

$$\xi = T\sqrt{\frac{\alpha}{\beta_2 L}}. \tag{8.59}$$

Using these transformations, the dimensional parameters are converted into normalized quantities. The normalized detuning is defined as

$$\Delta = \frac{\delta_0}{\alpha}, \tag{8.60}$$

and the normalized pump amplitude is

$$F = \sqrt{\frac{8\gamma L \xi P_{\text{in}}}{\alpha^3}}. \tag{8.61}$$

The normalized TPA coefficient used in the simulation is

$$S_{\text{TPA}} = \frac{\beta_{\text{TPA}}}{2\gamma A_{\text{eff}}}. \tag{8.62}$$

The contribution of FC effect is incorporated into the normalized LLE through the parameter $FC(\psi)$, which accounts for both FCA and FCD induced by TPA. The normalized FC contribution is expressed as

$$FC(\psi) = C \int_0^{\xi} |\psi(\xi')|^4 d\xi'. \tag{8.63}$$

The strength of this FC contribution is determined by the normalized coefficient C, which is given by

$$C = \frac{\sigma \pi \beta_{\mathrm{TPA}} \tau_c \alpha (1 + i\mu)}{4h A_{\mathrm{eff}}^2 \gamma^2 L_{\mathrm{eff}} \omega_p}. \tag{8.64}$$

The resulting normalized LLE solved numerically is therefore

$$\frac{\partial \psi(\tau, \xi)}{\partial \tau} = \left[-1 - i\Delta + i\eta \frac{\partial^2}{\partial \xi^2} + i|\psi|^2 - S_{\mathrm{TPA}} |\psi|^2 - FC(\psi) \right] \psi + F, \tag{8.65}$$

where η represents the sign of the second-order dispersion.

8.4 Split-Step Fourier Method

The SSFM is used to numerically solve the Equation (8.65) by separating the evolution into linear and nonlinear contributions. Each contribution is independently solved over a small normalized slow-time interval $\delta\tau$, and the resulting operators are sequentially applied to obtain the intracavity field evolution.

Therefore normalized LLE can be expressed as

$$\frac{\partial \psi(\tau, \xi)}{\partial \tau} = [\mathcal{L} + \mathcal{N}] \, \psi(\tau, \xi) + F, \tag{8.66}$$

where the linear operator is

$$\mathcal{L} = -1 - i\Delta + i\eta \frac{\partial^2}{\partial \xi^2}, \tag{8.67}$$

and the nonlinear operator is

$$\mathcal{N} = \left[(i - S_{\mathrm{TPA}})|\psi|^2 - FC(\psi)\right]. \tag{8.68}$$

The linear evolution is first considered independently

$$\frac{\partial \psi}{\partial \tau} = \mathcal{L}\psi. \tag{8.69}$$

Applying the Fourier transform with respect to the fast-time coordinate gives

$$\mathcal{F}\left\{\frac{\partial^2 \psi}{\partial \xi^2}\right\} = -\omega^2 \tilde{\psi}. \tag{8.70}$$

.

Therefore, the field evolution in the frequency domain is

$$\tilde{\psi}(\tau + \delta\tau, \omega) = \tilde{\psi}(\tau, \omega) \exp\left[\left(-1 - i\Delta + i\eta\omega^2\right)\delta\tau\right]. \tag{8.71}$$

After inverse Fourier transformation, the linearly propagated field is

$$\psi_L(\tau + \delta\tau, \xi) = \mathcal{F}^{-1}\left\{\exp\left[\left(-1 - i\Delta + i\eta\omega^2\right)\delta\tau\right]\mathcal{F}\{\psi(\tau, \xi)\}\right\}. \tag{8.72}$$

The nonlinear evolution is then applied in the time domain

$$\frac{\partial \psi}{\partial \tau} = \left[(i - S_{\mathrm{TPA}})|\psi|^2 - FC(\psi)\right]\psi. \tag{8.73}$$

For a sufficiently small slow-time step $\delta\tau$, the nonlinear contribution is integrated analytically

$$\psi_{NL} = \psi_L \exp\left[\left((i - S_{\mathrm{TPA}})|\psi_L|^2 - FC(\psi_L)\right)\delta\tau\right]. \tag{8.74}$$

The external driving field is incorporated separately following the numerical implementation

$$\psi(\tau + \delta\tau, \xi) = \psi_{NL} + F\delta\tau. \tag{8.75}$$

Thus, the nonlinear propagation is treated using the exponential nonlinear operator, while the pump contribution is introduced using a first-order explicit update.

Combining the linear propagation, nonlinear propagation, and pump injection steps gives the SSFM update implemented in the numerical solver is

$$\begin{aligned}\psi(\tau + \delta\tau, \xi) =& \mathcal{F}^{-1}\Bigg\{ \exp\left[\left(-1 - i\Delta + i\eta\omega^2\right)\delta\tau\right] \\ &\times \mathcal{F}\{\psi(\tau, \xi)\}\Bigg\} \\ &\times \exp\left[\left((i - S_{\text{TPA}})|\psi_L|^2 - FC(\psi_L)\right)\delta\tau\right] + F\delta\tau.\end{aligned} \tag{8.76}$$

Equation (8.76) represents the sequence implemented in the numerical code. During each normalized slow-time step, the normalized field ψ first undergoes linear propagation in the frequency domain, followed by Kerr nonlinear phase accumulation, TPA, and FC effects in the time domain. Finally, the external pump field is added to account for continuous energy injection into the resonator.

The SSFM is repeated over the normalized slow-time coordinate to simulate the evolution of frequency comb formation in the InGaAsP-OI ring resonator presented in Chapter 3.

Chapter 9

FC lifetime in p–n junction integrated InGaAsP-OI waveguides

This appendix details the numerical methodology and simulation workflow used to evaluate carrier removal dynamics in a straight, p-n junction-integrated InGaAsP-OI ridge waveguide. Simulations were performed using Ansys Lumerical CHARGE (Version: 2024 R1) to extract the effective carrier extraction time (τ_{ext}) as a function of reverse-bias voltage. The 2D transverse

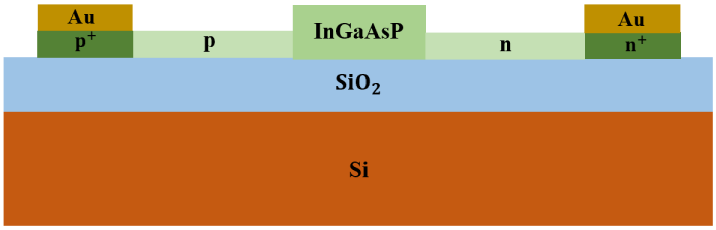


FIGURE 9.1: Schematic cross-section of the device used for simulations, featuring a reverse-biased p-n junction integrated with a InGaAsP-OI waveguide.

cross-section of the waveguide was implemented using Ansys Lumerical CHARGE (Version 2024 R1) with a 6 μm thick silicon substrate, a 3 μm thick SiO_2 buried oxide layer, and a 490 nm $\times$ 220 nm InGaAsP waveguide core, as illustrated in Figure 9.1. The material composition of the InGaAsP core is $In_{0.86}Ga_{0.14}As_{0.3}P_{0.7}$, matching the structural dimensions and material composition used for the microring resonator in Chapter 3 of this thesis. Lateral

p-n junction access was provided by 100 nm high InGaAsP side slabs extending outward from the core: a left inner P-doped slab (1000 nm wide, doped at 1.0×10^{24} m^{-3}) leading to an outer P^+-doped region (500 nm wide, doped at 1.0×10^{25} m^{-3}), and a right inner N-doped slab (1000 nm wide, doped at 1.0×10^{24} m^{-3}) leading to an outer N^+-doped region (500 nm wide, doped at 1.0×10^{25} m^{-3}). Ohmic electrical contacts were established using 500 nm wide gold (Au) pads positioned on top of the outer P^+ and N^+ regions. To avoid artificial density distortions from the heavily doped contact areas, data extractions were performed strictly within the waveguide core.

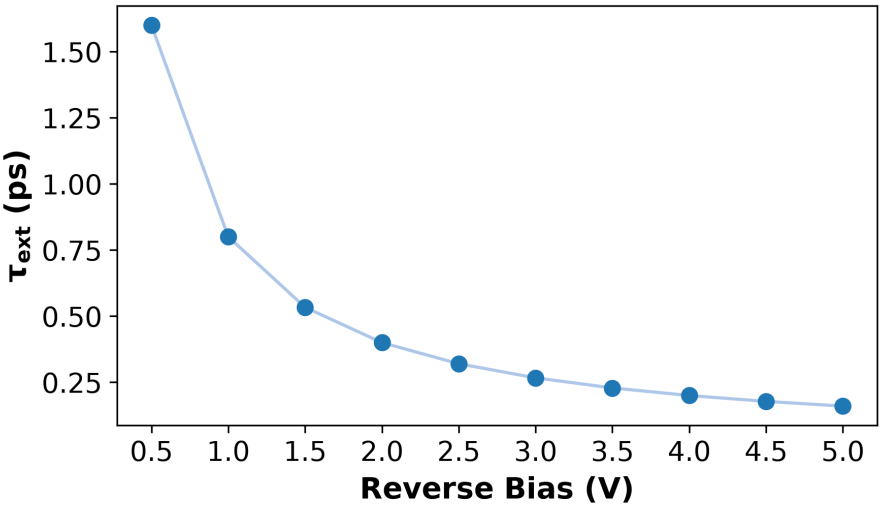


FIGURE 9.2: Extracted effective carrier extraction time constant (τ_{ext} in picoseconds) across the 220 nm $\times$ 490 nm InGaAsP waveguide core as a function of reverse bias voltage.

The net effective carrier lifetime (τ_{eff}) governing steady-state free-carrier density in the core is modeled as a parallel combination of intrinsic material recombination and field-driven carrier extraction:

$$\frac{1}{\tau_{eff}} = \frac{1}{\tau_c} + \frac{1}{\tau_{ext}}$$

where τ_{ext} is the effective extraction time constant quantifying the drift-transit time required to pull free-carriers out of the core volume into adjacent contact regions. We can use extraction time as a reliable proxy for the average carrier lifetime because the strong reverse-bias electric field sweeps carriers

out much faster than they can recombine internally ($\tau_{ext} \ll \tau_c$), making extraction the primary decay mechanism. Consequently, the effective lifetime is dominated by the extraction rate.

The calculated τ_{eff} as a function of applied reverse bias voltage is illustrated in Figure 9.2. At 0.5 V reverse bias, the extraction time constant is approximately 1.6 ps. Increasing the bias voltage to 5.0 V reduces τ_{ext} down to below 0.2 ps. This observation of carrier lifetime reduction with increasing reverse voltage is consistent with published data on SOI waveguides integrated with reverse-biased p-n junction [244].

Achieving sub-picosecond τ_{eff} confirms that free-carrier absorption can be effectively mitigated, serving as an encouraging baseline for future frequency comb generation in the InGaAsP-OI microring platforms explored in Chapter 3.

Bibliography

[1] A. G. Bell, "On the production and reproduction of sound by light," *American Journal of Science*, vol. 3, no. 118, pp. 305–324, 1880.

[2] S. E. Miller, "Integrated optics: An introduction," *Bell System Technical Journal*, vol. 48, no. 7, pp. 2059–2069, 1969.

[3] K. C. Kao and G. A. Hockham, "Dielectric-fibre surface waveguides for optical frequencies," *Proceedings of the Institution of Electrical Engineers*, vol. 113, no. 7, pp. 1151–1158, 1966.

[4] I. Hayashi, M. B. Panish, P. W. Foy, and S. Sumski, "Junction lasers which operate continuously at room temperature," *Applied Physics Letters*, vol. 17, no. 3, pp. 109–111, 1970.

[5] Z. I. Alferov et al., "Investigation of the influence of the parameters of $Al_xGa_{1-x}As$–GaAs heterojunctions on the threshold current density and the realization of continuous emission at room temperature," *Fizika i Tekhnika Poluprovodnikov*, vol. 4, no. 9, pp. 1826–1829, 1970.

[6] Z. Zhou, X. Ou, and Q. Fang, "Photonic integrated circuits for artificial intelligence acceleration," *Nature Photonics*, vol. 17, no. 11, pp. 945–957, 2023.

[7] S. Ning et al., "Photonic-electronic integrated circuits for high-performance computing and ai accelerators," *Journal of Lightwave Technology*, vol. 42, no. 22, pp. 7834–7859, 2024.

[8] R. Soref, "The past, present, and future of silicon photonics," *IEEE Journal of Selected Topics in Quantum Electronics*, vol. 12, no. 6, pp. 1678–1687, 2006.

[9] Q. Lin, O. J. Painter, and G. P. Agrawal, "Nonlinear optical phenomena in silicon waveguides: Modeling and applications," *Optics express*, vol. 15, no. 25, pp. 16 604–16 644, 2007.

[10] D. Liang and J. E. Bowers, "Recent progress in heterogeneous iii-v-on-silicon photonic integration," *Light: Advanced Manufacturing*, vol. 2, no. 1, pp. 59–83, 2021.

[11] T. Komljenovic et al., "Heterogeneous silicon photonic integrated circuits," *Journal of Lightwave Technology*, vol. 34, no. 1, pp. 20–35, 2016.

[12] J. C. Norman, D. Jung, Y. Wan, and J. E. Bowers, "Perspective: The future of quantum dot photonic integrated circuits," *APL photonics*, vol. 3, no. 3, 2018.

[13] J. Norman et al., "Electrically pumped continuous wave quantum dot lasers epitaxially grown on patterned, on-axis (001) si," *Optics Express*, vol. 25, no. 4, pp. 3927–3934, 2017.

[14] J. Zhang et al., "Iii-v-on-si photonic integrated circuits realized using micro-transfer-printing," *APL photonics*, vol. 4, no. 11, 2019.

[15] M. Liao, S. Chen, J.-S. Park, A. Seeds, and H. Liu, "Iii–v quantum-dot lasers monolithically grown on silicon," *Semiconductor Science and Technology*, vol. 33, no. 12, p. 123 002, 2018.

[16] D. Huang et al., "High-power sub-khz linewidth lasers fully integrated on silicon," *Optica*, vol. 6, no. 6, pp. 745–752, 2019.

[17] S. M. Sze and K. K. Ng, *Physics of Semiconductor Devices*, 3rd. Hoboken, NJ: John Wiley & Sons, 2006, ISBN: 978-0-471-14323-0.

[18] L. A. Coldren, S. W. Corzine, and M. L. Mashanovitch, *Diode Lasers and Photonic Integrated Circuits*, 2nd. Hoboken, NJ: John Wiley & Sons, 2012, ISBN: 978-0-470-48412-8.

[19] D. Liang and J. E. Bowers, "Recent progress in heterogeneous III-V on silicon photonics," *Light: Science & Applications*, vol. 1, no. 5, e15, 2012.

[20] K. Vyas et al., "Group III-V semiconductors as promising nonlinear integrated photonic platforms," *Advances in Physics: X*, vol. 7, no. 1, p. 2 097 020, 2022.

[21] L. A. Coldren, S. C. Nicholes, L. A. Johansson, J. W. Raring, and J. Klamkin, "High-density InP-based photonic integrated circuits," *IEEE Journal of Selected Topics in Quantum Electronics*, vol. 17, no. 5, pp. 1420–1438, 2011.

[22] M. K. Smit and J. J. G. M. van der Tol, "Photonic integrated circuits: Monolithic InP integration," *Laser & Photonics Reviews*, vol. 8, no. 2, pp. 189–203, 2014.

[23] S. Adachi, "Optical properties of $in_{1-x}ga_xas_yp_{1-y}$ alloys: Model of dielectric function," *Journal of Applied Physics*, vol. 66, no. 12, pp. 6030–6040, 1989. DOI: 10.1063/1.343580

[24] D. Dai, J. Bauters, and J. E. Bowers, "Passive technologies on silicon/III–V photonic integrated circuits," *IEEE Journal of Selected Topics in Quantum Electronics*, vol. 18, no. 5, pp. 1572–1580, 2012. DOI: 10.1109/JSTQE.2012.2190716

[25] R. Nagarajan et al., "Inp photonic integrated circuits," *IEEE Journal of Selected Topics in Quantum Electronics*, vol. 16, no. 5, pp. 1113–1125, 2010. DOI: 10.1109/JSTQE.2009.2037828

[26] J.-K. Park, J.-H. Han, M. Takenaka, and S. Takagi, "Ingaasp variable optical attenuator with lateral pin junction formed by ni-ingaasp and zn diffusion on iii-v on insulator wafer," *MRS advances*, vol. 1, no. 48, pp. 3295–3300, 2016.

[27] G. Roelkens et al., "Heterogeneous iii-v/silicon photonic integrated circuits," in *Asia Communications and Photonics Conference*, Optica Publishing Group, 2013, ATh3A–5.

[28] P. Saeidi et al., "Demonstration of optical non-reciprocity and nonlinearities in integrated photonic platforms," *Optics Letters*, vol. 43, pp. 2100–2103, 2018.

[29] E. Mobini et al., "C-band nonlinear optical interactions in InGaAsP/InP passive waveguides," *Journal of Physics: Photonics*, vol. 8, no. 1, p. 015 039, 2026. DOI: 10.1088/2515-7647/ae38ac

[30] L. Chang et al., "Ultra-efficient frequency comb generation in algaas-on-insulator microresonators," *Nature Communications*, vol. 11, p. 1331, 2020. DOI: 10.1038/s41467-020-15005-5

[31] W. Xie et al., "Ultrahigh-Q AlGaAs-on-insulator microresonators for integrated nonlinear photonics," en, *Optics Express*, vol. 28, no. 22, p. 32 894, 2020, ISSN: 1094-4087. DOI: 10.1364/OE.405343 Accessed: Oct. 20, 2025. [Online]. Available: https://opg.optica.org/abstract.cfm?URI=oe-28-22-32894

[32] B. E. A. Saleh and M. C. Teich, *Fundamentals of Photonics*, 3rd. Hoboken, NJ: Wiley, 2019, ISBN: 978-1-119-50687-4.

[33] K. Okamoto, *Fundamentals of Optical Waveguides*, 3rd. Academic Press, 2021, ISBN: 9780128160053.

[34] A. Yariv and P. Yeh, *Photonics: Optical Electronics in Modern Communications*, 6th. New York, NY: Oxford University Press, 2007, ISBN: 978-0-19-517946-0.

[35] C. R. Pollock and M. Lipson, *Integrated Photonics*. Boston, MA: Kluwer Academic Publishers, 2003, ISBN: 978-1-4020-7635-0.

[36] V. S and K. K. Varikuntla, "Nano photonics and quantum computing: A path to next generation computing," in *Handbook of Nano-Metamaterials*, B. Choudhury, V. K. Tewary, and V. K. Kanth, Eds., Singapore: Springer Nature Singapore, 2025, pp. 1–40, ISBN: 978-981-13-0261-9. DOI: 10.1007/978-981-13-0261-9_58-1

[37] M. A. Green, "Self-consistent optical parameters of intrinsic silicon at 300 k including temperature coefficients," *Solar Energy Materials and Solar Cells*, vol. 92, no. 11, pp. 1305–1310, 2008.

[38] P. Dumon et al., "Low-loss soi photonic wires and ring resonators fabricated with deep uv lithography," *IEEE Photonics Technology Letters*, vol. 16, no. 5, pp. 1328–1330, 2004.

[39] K. Ikeda, R. E. Saperstein, N. Alic, and Y. Fainman, "Thermal and kerr nonlinear properties of plasma-deposited silicon nitride/silicon dioxide waveguides," *Optics express*, vol. 16, no. 17, pp. 12 987–12 994, 2008.

[40] J. F. Bauters et al., "Ultra-low-loss high-aspect-ratio si3n4 waveguides," *Optics express*, vol. 19, no. 4, pp. 3163–3174, 2011.

[41] M. Zhang, C. Wang, R. Cheng, A. Shams-Ansari, and M. Lončar, "Monolithic ultra-high-q lithium niobate microring resonator," *Optica*, vol. 4, no. 12, pp. 1536–1537, 2017.

[42] G. Poberaj, H. Hu, W. Sohler, and P. Guenter, "Lithium niobate on insulator (lnoi) for micro-photonic devices," *Laser & photonics reviews*, vol. 6, no. 4, pp. 488–503, 2012.

[43] M. K. Smit et al., "An introduction to InP-based generic integration technology," *Semiconductor Science and Technology*, vol. 29, no. 8, p. 083 001, 2014. DOI: 10.1088/0268-1242/29/8/083001

[44] M. Pu, L. Ottaviano, E. Semenova, and K. Yvind, "Efficient frequency comb generation in AlGaAs-on-insulator microresonators," *Optica*, vol. 3, no. 8, pp. 823–826, 2016.

[45] E. Mobini et al., "C-band nonlinear optical interactions in ingaasp/inp passive waveguides," *Journal of Physics: Photonics*, vol. 8, no. 1, p. 015 039, 2026.

[46] B. Jalali and S. Fathpour, "Silicon photonics," *Journal of Lightwave Technology*, vol. 24, no. 12, pp. 4600–4615, 2006. DOI: 10.1109/JLT.2006.885782

[47] T. L. Koch and U. Koren, "Semiconductor photonic integrated circuits," *IEEE Journal of Quantum Electronics*, vol. 27, no. 3, pp. 641–653, 1991.

[48] M. Smit, K. Williams, and J. van der Tol, "Past, present, and future of InP-based photonic integrated circuits," *IEEE Journal of Selected Topics in Quantum Electronics*, vol. 20, no. 4, pp. 1–10, 2014. DOI: 10.1109/JSTQE.2014.2301994

[49] J. Van Campenhout et al., "Electrically pumped InP-based microdisk lasers integrated with a silicon optical circuit," *Optics Express*, vol. 15, no. 10, pp. 6710–6715, 2007.

[50] R. A. Soref, "Silicon-based optoelectronics," *Proceedings of the IEEE*, vol. 81, no. 12, pp. 1687–1706, 1993.

[51] G. Roelkens et al., "III-V-on-silicon photonic devices for optical communication and sensing," *Photonics*, vol. 2, no. 3, pp. 969–1004, 2014. DOI: 10.3390/photonics2030969

[52] G. P. Agrawal, *Lightwave Technology: Components and Devices*. Hoboken, NJ: Wiley-Interscience, 2004, ISBN: 978-0-471-21573-8.

[53] J. Michel, J. Liu, and L. C. Kimerling, "Silicon photonics: Emerging technology for future data communications," *Nature Photonics*, vol. 4, no. 8, pp. 527–534, 2010. DOI: 10.1038/nphoton.2010.135

[54] M. Bohr, "The evolution of scaling from the homogeneous era to the heterogeneous era," in *2011 international electron devices meeting*, IEEE, 2011, pp. 1–1.

[55] D. A. B. Miller, "Device requirements for optical interconnects to silicon chips," *Proceedings of the IEEE*, vol. 97, no. 7, pp. 1166–1185, 2009. DOI: 10.1109/JPROC.2009.2014298

[56] M. Marks, Z. Hassan, and K. Y. Cheong, "Ultrathin wafer pre-assembly and assembly process technologies: A review," *Critical Reviews in Solid*

State and Materials Sciences, vol. 40, no. 3, pp. 1–40, 2015. DOI: 10.1080/10408436.2014.992585

[57] M. Dinu, F. Quochi, and H. Garcia, "Third-order optical nonlinearities in silicon at telecom wavelengths," *Applied Physics Letters*, vol. 82, no. 18, pp. 2954–2956, 2003. DOI: 10.1063/1.1571665

[58] M. Pu, L. Ottaviano, E. Semenova, and K. Yvind, "Efficient frequency comb generation in algaas-on-insulator waveguides," *Optica*, vol. 3, no. 8, pp. 823–826, 2016. DOI: 10.1364/OPTICA.3.000823

[59] H. Salamon et al., "Electrical control of quantum dots in gaas-on-insulator waveguides for coherent single-photon generation," arXiv:2508.04584, 2025. DOI: 10.48550/arXiv.2508.04584

[60] G. Moody, "Nonlinear integrated photonics for quantum communications and computing," in *Quantum Information Science, Sensing, and Computation XV*, E. Donkor, M. Hayduk, M. L. Fanto, and C. M. Torres Jr., Eds., vol. PC12517, SPIE, 2023, PC1251701. DOI: 10.1117/12.2663696

[61] L. Chang, W. Xie, H. Shu, and J. E. Bowers, "Algaas-on-insulator integrated photonics for nonlinear optics," *IEEE Journal of Selected Topics in Quantum Electronics*, vol. 26, no. 2, pp. 1–11, 2020.

[62] A. Thulaseedharan, L Fujii dos Santos, T Moradi, C Kupchak, and K Dolgaleva, "Impact of nonlinear losses on the performance of ingaasp-on-insulator ring resonators," *Journal of the Optical Society of America B*, vol. 43, no. 3, A146–A151, 2026.

[63] S. May et al., "Algaas-on-insulator platform for integrated nonlinear optics," *Journal of Optics*, vol. 23, p. 054 001, 2021.

[64] C. Wang et al., "Integrated lithium niobate electro-optic modulators," *IEEE Photonics Journal*, vol. 8, no. 6, pp. 1–8, 2016.

[65] Z. Wang et al., "Room-temperature inp distributed feedback laser array directly grown on silicon," *Nature Photonics*, vol. 9, no. 12, pp. 837–842, 2015.

[66] C. Xiang, W. Jin, and J. E. Bowers, "Silicon nitride passive and active photonic integrated circuits: Trends and prospects," *Photonics research*, vol. 10, no. 6, A82–A96, 2022.

[67] Z. Wang et al., "High-q microresonators in iii-v platforms," *Optics Letters*, vol. 49, pp. 1120–1123, 2024.

[68] L. Chang et al., "Heterogeneously integrated gaas waveguides on insulator for efficient frequency conversion," *Laser & Photonics Reviews*, vol. 12, no. 10, p. 1 800 149, 2018. DOI: 10.1002/lpor.201800149

[69] G. P. Agrawal, *Nonlinear Fiber Optics*, 6th. San Diego, CA: Academic Press, 2019, ISBN: 978-0-12-817042-7.

[70] A. C. Turner-Foster, C. Manolatou, B. S. Schmidt, M. Lipson, M. A. Garcia, and A. L. Gaeta, "Tailored anomalous group-velocity dispersion in silicon channel waveguides," *Optics Express*, vol. 14, no. 10, pp. 4357–4362, 2006. DOI: 10.1364/OE.14.004357

[71] R. W. Boyd, *Nonlinear Optics*, 4th. London, UK: Academic Press, 2020, ISBN: 978-0-12-811002-7.

[72] T. J. Kippenberg, A. L. Gaeta, M. Lipson, and M. L. Gorodetsky, "Dissipative Kerr solitons in optical microresonators," *Science*, vol. 361, no. 6402, eaan8083, 2018. DOI: 10.1126/science.aan8083

[73] J. M. Dudley, G. Genty, and S. Coen, "Supercontinuum generation in photonic crystal fiber," *Reviews of Modern Physics*, vol. 78, no. 4, pp. 1135–1184, 2006. DOI: 10.1103/RevModPhys.78.1135

[74] V. R. Almeida, C. A. Barrios, R. R. Panepucci, and M. Lipson, "All-optical control of light on a chip," *Nature*, vol. 431, no. 7012, pp. 1081–1084, 2004. DOI: 10.1038/nature02921

[75] D. J. Moss, R. Morandotti, A. L. Gaeta, and M. Lipson, "New CMOS-compatible platforms for integrated high-speed nonlinear optics," *Nature Photonics*, vol. 7, no. 8, pp. 597–607, 2013. DOI: 10.1038/nphoton.2013.183

[76] J. Hansryd, P. A. Andrekson, M. Westlund, J. Li, and P. O. Hedekvist, "Fiber-based optical parametric amplifiers and oscillators," *IEEE Journal of Selected Topics in Quantum Electronics*, vol. 8, no. 3, pp. 506–520, 2002. DOI: 10.1109/JSTQE.2002.1016354

[77] M. Yu et al., "Coherent two-octave-spanning microcomb generation in silicon nitride," *Optics Letters*, vol. 41, pp. 2867–2870, 2016.

[78] Q. Li et al., "Energy transfer dynamics in optical microresonators," *Physical Review A*, vol. 90, p. 033 801, 2014.

[79] T. J. Kippenberg, S. M. Spillane, and K. J. Vahala, "Kerr-nonlinearity optical parametric oscillation in an ultrahigh-q toroid microcavity," *Physical Review Letters*, vol. 93, p. 083 904, 2004.

[80] T. J. Kippenberg, R. Holzwarth, and S. A. Diddams, "Microresonator-based optical frequency combs," *Science*, vol. 332, pp. 555–559, 2011.

[81] P. Del'Haye, A. Schliesser, O. Arcizet, T. Wilken, R. Holzwarth, and T. J. Kippenberg, "Optical frequency comb generation from a monolithic microresonator," *Nature*, vol. 450, pp. 1214–1217, 2007.

[82] J. B. Lasky, "Wafer bonding for silicon-on-insulator technologies," *Applied Physics Letters*, vol. 48, no. 1, pp. 78–80, 1986. DOI: 10.1063/1.96768

[83] M. Alexe and U. Gösele, *Wafer Bonding: Applications and Technology*. Berlin, Heidelberg: Springer, 2004, ISBN: 978-3-642-05915-5. DOI: 10.1007/978-3-662-10827-7

[84] U. Gösele and Q.-Y. Tong, *Semiconductor Wafer Bonding: Science and Technology*. John Wiley & Sons, 2000.

[85] C.-T. Ko and K.-N. Chen, "Wafer-level bonding/stacking technology for 3d integration," *Microelectronics Reliability*, vol. 50, no. 4, pp. 481–488, 2010. DOI: 10.1016/j.microrel.2009.09.015

[86] K. N. Bhat et al., "Wafer bonding - a powerful tool for mems," *Indian Journal of Pure & Applied Physics*, vol. 45, no. 4, pp. 326–341, 2007.

[87] B. Bêche et al., "Integrated optics devices based on polymer and dielectric layers," *Optics Communications*, vol. 315, pp. 325–331, 2014.

[88] M. Homayouni et al., "Adhesive wafer bonding using polymer interlayers," *Microelectronic Engineering*, vol. 128, pp. 237–242, 2014.

[89] X. Yu et al., "Low temperature wafer bonding using thin film interlayers," *Sensors and Actuators A: Physical*, vol. 115, pp. 67–72, 2004.

[90] W. B. Yu, C. M. Tan, J. Wei, S. S. Deng, and S. M. L. Nai, "Influence of applied load on vacuum wafer bonding at low temperature," *Sensors and Actuators A: Physical*, vol. 115, no. 1, pp. 67–72, 2004. DOI: 10.1016/j.sna.2004.03.017

[91] T. Suni et al., "Direct wafer bonding with thin atomic layer deposited oxide films," *Journal of The Electrochemical Society*, vol. 149, G348–G351, 2002.

[92] K. Nagano et al., "Surface activated bonding for heterogeneous integrated photonics," *Applied Surface Science*, vol. 612, p. 155 800, 2023.

[93] M. Takeuchi et al., "Advances in low-temperature dielectric-to-dielectric bonding," *IEEE Transactions on Semiconductor Manufacturing*, vol. 37, pp. 102–108, 2024.

[94] F. Niklaus, G. Stemme, J.-Q. Lu, and R. J. Gutmann, "Adhesive wafer bonding," *Journal of Applied Physics*, vol. 99, p. 031 101, 2006.

[95] C. Chao et al., "Ammonium hydroxide wet etching treatments for surface preparation," *Journal of The Electrochemical Society*, vol. 152, G200–G205, 2005.

[96] B. G. Yacobi, S. Martin, and A. Kalinin, "Adhesive bonding technology for microelectronics and photonics," *Semiconductor Science and Technology*, vol. 17, R91–R102, 2002.

[97] Y. Lin et al., "Adhesive bonding methods for heterogeneous photonic integrated circuits," *Optics Express*, vol. 27, pp. 12 400–12 409, 2019.

[98] P. Sekhar et al., "Wafer bonding protocols for heterogeneous photonic integrated circuits," *IEEE Transactions on Components, Packaging and Manufacturing Technology*, vol. 13, no. 4, pp. 520–528, 2023.

[99] S. Gao et al., "Ultra-precision chemical mechanical grinding and polishing for semiconductor substrates," *Precision Engineering*, vol. 74, pp. 210–220, 2022.

[100] H. Lee et al., "Material processing and surface modification for direct wafer bonding," *ACS Applied Materials & Interfaces*, vol. 9, pp. 14 500–14 508, 2017.

[101] E. Nojonen, "Thinning of gallium arsenide wafers using advanced abrasives and etchants for laser applications," M.S. thesis, Tampere University, 2021.

[102] G. Elssner and G. Petzow, "Interfaces in ceramic-to-metal bonding," *ISIJ International*, vol. 39, pp. 1000–1008, 1999.

[103] F. Klocke et al., "Process mechanisms in high-precision surface finishing of optical materials," *CIRP Annals*, vol. 58, pp. 491–496, 2009.

[104] H. Bu et al., "Etch selectivity and surface roughness during wet chemical processing of iii-v materials," *Applied Surface Science*, vol. 360, pp. 225–230, 2016.

[105] R. P. Feynman, R. B. Leighton, and M. Sands, *The Feynman Lectures on Physics*. Addison-Wesley, 1963.

[106] X. Meng et al., "Novel fabrication strategies for photonic integrated circuits," *Journal of Optics*, vol. 18, p. 044 001, 2016.

[107] M. S. Alias et al., "Review of iii-v semiconductor processing for photonic devices," *Progress in Quantum Electronics*, vol. 58, pp. 1–25, 2018.

[108] V. Van et al., "Optical microring resonators in inp-based platforms," *IEEE Journal of Selected Topics in Quantum Electronics*, vol. 8, pp. 705–713, 2002.

[109] S. Zhuiykov, *Nanostructured Semiconductor Oxides for the Next Generation of Electronics and Photonics*. Woodhead Publishing, 2018.

[110] E. Barrigón et al., "Synthesis and integration of iii-v semiconductors on silicon platforms," *Chemical Reviews*, vol. 119, pp. 8499–8531, 2019.

[111] M. Altissimo, "E-beam lithography for nanofabrication," *Biomicrofluidics*, vol. 4, p. 022 903, 2010.

[112] V.-C. Su et al., "Advances in optical metasurfaces: Fabrication and applications," *Optics Express*, vol. 26, pp. 13 148–13 182, 2018.

[113] R. W. Devenish et al., "Nanolithography and high-resolution electron beam techniques," *Philosophical Magazine B*, vol. 60, pp. 623–633, 1989.

[114] S. N. Mohammad, *Fundamentals of Nanofabrication and Semiconductor Nanotechnology*. Springer, 2011.

[115] S. Cabrini and S. Kawata, *Nanofabrication Handbook*. CRC Press, 2012.

[116] D. Meyerhofer, "Resolution limits of optical and e-beam lithography," *Journal of Vacuum Science & Technology B*, vol. 6, pp. 1900–1904, 1988.

[117] G. Owen and P. Rissman, "Proximity effect correction for electron beam lithography by equalization of background dose," *Journal of Applied Physics*, vol. 54, no. 6, pp. 3573–3581, 1983. DOI: 10.1063/1.332426

[118] M. Parikh, "Corrections to proximity effects in electron beam lithography," *Journal of Applied Physics*, vol. 50, pp. 4371–4387, 1979.

[119] Y. Yamashita, R. Kawazu, K. Koshida, and H. Kawakami, "Proximity effect correction by electron-beam exposure dose modulation using a simple fast algorithm," *Journal of Vacuum Science & Technology B: Microelectronics and Nanometer Structures Processing, Measurement, and Phenomena*, vol. 14, no. 6, pp. 3845–3849, 1996. DOI: 10.1116/1.588752 [Online]. Available: https://doi.org/10.1116/1.588752

[120] G. Owen, "Methods for proximity effect correction in electron beam lithography," *Journal of Vacuum Science & Technology B*, vol. 8, pp. 1889–1892, 1990.

[121] C. A. Mack, "Electron beam lithography simulation and proximity correction," *Proceedings of SPIE*, vol. 4343, pp. 313–321, 2001.

[122] Y. Todokoro, Y. Takasu, and T. Ohkuma, "Multilayer resist systems for optical and e-beam lithography," in *Electron-Beam, X-Ray, and Ion-Beam Techniques for Submicrometer Lithographies IV*, SPIE, vol. 537, 1985, pp. 179–187.

[123] H. Yamashita, M. Amemiya, and K. Kobayashi, "Proximity effect correction methods for electron beam lithography," in *SPIE Proceedings on Electron-Beam Technology for Semiconductor Fabrication*, vol. 3873, 1999, pp. 120–129. DOI: 10.1117/12.947500

[124] L. V. Gregor, "Multilayer resist schemes for high-resolution e-beam patterning," *Solid State Technology*, vol. 31, pp. 105–110, 1988.

[125] K. Yao et al., "Advanced proximity effect correction strategies for dense nanostructures," *Microelectronic Engineering*, vol. 270, p. 105 718, 2023.

[126] J. Zhou and X. Yang, "Monte carlo simulation of process parameters in electron beam lithography for thick resist patterning," *Journal of Vacuum Science & Technology B: Microelectronics and Nanometer Structures Processing, Measurement, and Phenomena*, vol. 24, no. 3, pp. 1202–1209, Apr. 2006, ISSN: 1071-1023. DOI: 10.1116/1.2192543 eprint: https://pubs.aip.org/avs/jvb/article-pdf/24/3/1202/15639364/1202_1_online.pdf. [Online]. Available: https://doi.org/10.1116/1.2192543

[127] GenISys GmbH, *Beamer user manual – advanced pattern processing and proximity effect correction software*, GenISys GmbH, Munich, Germany, 2023. [Online]. Available: https://www.genisys-gmbh.com/beamer.html

[128] S. Lee, J. Jacob, C. Chen, et al., "Proximity effect correction in electron-beam lithography: A hierarchical rule-based scheme—pyramid," *Journal of Vacuum Science & Technology B*, vol. 9, pp. 3048–3053, 1991.

[129] C. Li et al., "Recent advances in plasma etching for micro and nano fabrication of silicon-based materials: A review," *Journal of Materials Chemistry C*, vol. 12, no. 45, pp. 18 211–18 237, 2024.

[130] J. W. Coburn and H. F. Winters, "Ion-and electron-assisted gas-surface chemistry—an important effect in plasma etching," *Journal of Applied physics*, vol. 50, no. 5, pp. 3189–3196, 1979.

[131] V. Vashistha, G. Vaidya, P. Gruszecki, A. E. Serebryannikov, and M. Krawczyk, "Polarization tunable all-dielectric color filter based on cross-shaped Si nanoantennas," *Scientific Reports*, vol. 7, no. 1, p. 8092, 2017. DOI: 10.1038/s41598-017-08083-6

[132] S. Sun et al., "Electromagnetic metasurfaces for light manipulation," *Advances in Optics and Photonics*, vol. 11, pp. 380–479, 2019.

[133] N. Yu and F. Capasso, "Flat optics based on metasurfaces," *Nature Materials*, vol. 13, pp. 139–150, 2014.

[134] G. Lee et al., "Optical metasurfaces for complex light field manipulation," *Nanophotonics*, vol. 10, pp. 785–802, 2021.

[135] Y. Yang et al., "Dual-band operation in all-dielectric metasurfaces," *ACS Photonics*, vol. 5, pp. 1200–1207, 2018.

[136] F. Jahangiri et al., "Beam steering and wavefront shaping with tunable metasurfaces," *Optics Express*, vol. 33, pp. 1020–1032, 2025.

[137] X. Zou et al., "Metasurface design and optimization using deep learning," *PhotoniX*, vol. 4, p. 12, 2023.

[138] M. Sanjari et al., "Reconfigurable plasmonic metasurfaces for phase control," *Nano Letters*, vol. 25, pp. 1200–1208, 2025.

[139] L. Xu et al., "Inverse design of optical metasurfaces using neural networks," *ACS Nano*, vol. 17, pp. 5400–5410, 2023.

[140] L. Pain et al., "Direct write e-beam lithography for advanced technology nodes," *Microelectronic Engineering*, vol. 83, pp. 711–716, 2006.

[141] T. H. P. Chang, "Proximity effect in electron beam lithography," *Journal of Vacuum Science & Technology*, vol. 12, pp. 1271–1275, 1975.

[142] C. I. Youngman and N. D. Wittels, "Proximity effect correction in electron beam lithography," *Proc. SPIE*, vol. 0135, pp. 54–58, 1978.

[143] F. Nikolajeff et al., "Measuring proximity parameters in electron beam lithography," *Applied Optics*, vol. 34, pp. 897–903, 1995.

[144] L.-W. Nien et al., "Proximity effect correction for complex 3d nanostructures," *Nanotechnology*, vol. 28, p. 445 301, 2017.

[145] Z. Li et al., "Review of proximity effect correction techniques in electron beam lithography," *Journal of Micro/Nanolithography, MEMS, and MOEMS*, vol. 14, p. 031 201, 2015.

[146] J. Mao et al., "Proximity effect calibration for deep sub-micron features," *IEEE Transactions on Nanotechnology*, vol. 24, pp. 105–112, 2025.

[147] M. Parikh, "Corrections to proximity effects in electron beam lithography. i. theory," *Journal of Applied Physics*, vol. 50, no. 6, pp. 4371–4377, 1979. DOI: 10.1063/1.326488

[148] J. Linnros, "Carrier lifetime measurements in silicon waveguides," *Journal of Applied Physics*, vol. 84, pp. 275–283, 1998.

[149] R. Butler and A. Caddle, "Integrated photonic platforms for communications," *Journal of Optical Communications*, vol. 44, pp. 120–128, 2023.

[150] L. Hoffmann et al., "Loss mechanisms in optical waveguides," *Optics Express*, vol. 17, pp. 18 900–18 910, 2009.

[151] J. Cabanillas-Gonzalez, G. Grancini, and G. Lanzani, "Pump-probe spectroscopy in organic semiconductors: Monitoring fundamental processes of relevance in optoelectronics," *Advanced Materials*, vol. 23, no. 46, pp. 5468–5485, 2011. DOI: 10.1002/adma.201102015

[152] L. Pavesi et al., "Optical gain in silicon nanocrystals," *Nature*, vol. 408, pp. 440–444, 2000.

[153] J. Revuelta et al., "Nonlinear dynamics in semiconductor microresonators," *Physical Review Letters*, vol. 130, p. 123 801, 2023.

[154] A. J. Sabbah and D. M. Riffe, "Femtosecond pump-probe spectroscopy of semiconductor surfaces," *Physical Review B*, vol. 62, pp. 16 174–16 182, 2000.

[155] A. Trita et al., "Nonlinear absorption and refraction in silicon-on-insulator waveguides," *Applied Physics Letters*, vol. 91, p. 041 112, 2007.

[156] A. Ashoka et al., "Integrated quantum photonics on iii-v platforms," *Advanced Quantum Technologies*, vol. 5, p. 2 100 120, 2022.

[157] S. Kim et al., "Ultrafast plasmonics for all-optical switching," *ACS Nano*, vol. 16, pp. 8500–8512, 2022.

[158] H. Zhao et al., "Demonstration of low-threshold kerr comb generation," *Optics Letters*, vol. 37, pp. 2150–2152, 2012.

[159] S. A. Srinivasan et al., "Extraction of carrier lifetime in ge waveguides using pump probe spectroscopy," *Applied Physics Letters*, vol. 108, no. 21, p. 211 101, 2016. DOI: 10.1063/1.4952432

[160] C. Föhrmann et al., "Free-carrier dispersion and absorption in semiconductor waveguides," *Physical Review B*, vol. 97, p. 195 201, 2018.

[161] J. Leuthold, C. Koos, and W. Freude, "Nonlinear silicon photonics," *Nature Photonics*, vol. 4, no. 8, pp. 535–544, 2010, ISSN: 1749-4893. DOI: 10.1038/nphoton.2010.185 [Online]. Available: https://doi.org/10.1038/nphoton.2010.185

[162] L. P. Gonzalez, J. M. Murray, S. Krishnamurthy, and S. Guha, "Wavelength dependence of two photon and free carrier absorptions in InP," *Optics Express*, vol. 17, no. 11, pp. 8741–8748, 2009. DOI: 10.1364/OE.17.008741

[163] A. Gil-Molina, I. Aldaya, J. L. Pita, L. H. Gabrielli, H. L. Fragnito, and P. Dainese, "Optical free-carrier generation in silicon nano-waveguides at 1550 nm," *Applied Physics Letters*, vol. 112, no. 25, p. 251 104, 2018, ISSN: 0003-6951. DOI: 10.1063/1.5023589 [Online]. Available: https://doi.org/10.1063/1.5023589

[164] M. Novarese, S. Romero-Garcia, J. Bovington, and M. Gioannini, "Dynamics of free carrier absorption and refractive index dispersion in si and si/polysi microrings," *IEEE Photonics Technology Letters*, vol. 35, no. 8, pp. 450–453, 2023.

[165] A. Lefrancois, M. Sorel, and D. C. Hutchings, "Nonlinear optical absorption and refraction in algaas waveguides at sub-bandgap wavelengths," *Journal of Optics*, vol. 17, no. 9, p. 095 501, 2015. DOI: 10.1088/2040-8978/17/9/095501

[166] G. Moille, Q. Li, X. Lu, and K. Srinivasan, "Kerr comb generation in microresonators with tailored dispersion," *Physical Review A*, vol. 99, no. 3, p. 033 848, 2019. DOI: 10.1103/PhysRevA.99.033848

[167] B. Lau, D. Brady, and A. Sarangan, "Optical properties and nonlinear absorption mechanisms in iii-v semiconductors," *Journal of Lightwave Technology*, vol. 33, no. 12, pp. 2450–2458, 2015. DOI: 10.1109/JLT.2015.2410012

[168] A. C. Turner-Foster et al., "Ultrashort free-carrier lifetime in low-loss silicon nanowaveguides," *Opt. Express*, vol. 18, no. 4, pp. 3582–3591,

2010. DOI: 10.1364/OE.18.003582 [Online]. Available: https://opg.optica.org/oe/abstract.cfm?URI=oe-18-4-3582

[169] A. C. Turner, M. A. Foster, A. L. Gaeta, and M. Lipson, "Ultra-low power parametric frequency conversion in a silicon microring resonator," *Opt. Express*, vol. 16, no. 7, pp. 4881–4887, 2008. DOI: 10.1364/OE.16.004881 [Online]. Available: https://opg.optica.org/oe/abstract.cfm?URI=oe-16-7-4881

[170] T. Johnson, "Silicon microdisk resonators for nonlinear optics and dynamics," Order No. 3514460. Available from ProQuest Dissertations & Theses Global; ProQuest Dissertations & Theses Global Closed Collection (1027906888), Ph.D. dissertation, ProQuest Dissertations & Theses Global, 2009. [Online]. Available: https://login.proxy.bib.uottawa.ca/login?url=https://www.proquest.com/dissertations-theses/silicon-microdisk-resonators-nonlinear-optics/docview/1027906888/se-2

[171] Y. Liu and H. K. Tsang, "Time dependent density of free carriers generated by two photon absorption in silicon waveguides," *Applied Physics Letters*, vol. 90, no. 21, p. 211 105, 2007. DOI: 10.1063/1.2741611 [Online]. Available: https://doi.org/10.1063/1.2741611

[172] S. Adachi, *Physical Properties of III-V Semiconductor Compounds*. New York, NY: John Wiley & Sons, 1992, ISBN: 978-0-471-58029-4.

[173] K. Vyas, K. M. Awan, and K. Dolgaleva, "Systematic study of inp/ingaasp heated plasma etching and roughness improvement for integrated optical devices," *Journal of Vacuum Science & Technology B*, vol. 41, no. 1, p. 012 804, 2023. DOI: 10.1116/6.0002167 [Online]. Available: https://doi.org/10.1116/6.0002167

[174] Ansys, Inc., *Lumerical 2024 r1*, https://www.lumerical.com/, Vancouver, Canada, 2024.

[175] O. Krochin, N. Fahrenkopf, and D. Coolbaugh, "Cmos-compatible photonic integration of iii-v and silicon platforms," *IEEE Journal of Quantum Electronics*, vol. 56, no. 4, pp. 1–9, 2020. DOI: 10.1109/JQE.2020.2985123

[176] J. J. G. M. van der Tol and M. K. Smit, "Inp-based photonic integrated circuits for advanced optical networks," *IET Optoelectronics*, vol. 4, no. 6, pp. 235–245, 2010. DOI: 10.1049/iet-opt.2009.0080

[177] D. Dimitropoulos, R. Joulcache, R. Zhou, and B. Jalali, "Lifetime measurements of free carriers generated by two-photon absorption in silicon waveguides," *Optics Express*, vol. 13, no. 10, pp. 3676–3682, 2005. DOI: 10.1364/OPEX.13.003676

[178] L. P. Gonzalez, J. M. Murray, S. Krishnamurthy, and S. Guha, "Wavelength dependence of two photon and free carrier absorptions in inp," *Optics express*, vol. 17, no. 11, pp. 8741–8748, 2009.

[179] K. L. Hall, G. Lenz, and E. P. Ippen, "Novel heterodyne pump–probe measurement of femtosecond nonlinearities in waveguides," in *Conference on Lasers and Electro-Optics*, Optica Publishing Group, 1992, JThF4. [Online]. Available: https://opg.optica.org/abstract.cfm?URI=CLEO-1992-JThF4

[180] S. L. Chuang, N. Peyghambarian, and S. Koch, *Physics of optoelectronic devices*, 1996.

[181] F. De Bellis et al., "Simultaneous electronic and thermal signatures in pump–probe spectroscopy of semiconductor nanocrystal films," *Nano Letters*, vol. 25, no. 18, pp. 7317–7325, 2025. DOI: 10.1021/acs.nanolett.5c00326 [Online]. Available: https://doi.org/10.1021/acs.nanolett.5c00326

[182] H. Carslaw and J. Jaeger, *Conduction of heat in solids 2nd edt oxford university*, 1959.

[183] F. G. Della Corte, G. Cocorullo, M. Iodice, and I. Rendina, "Temperature dependence of the thermo-optic coefficient of inp, gaas, and sic from room temperature to 600 k at the wavelength of 1.5 μm," *Applied Physics Letters*, vol. 77, no. 11, pp. 1614–1616, 2000.

[184] J. Dziewior and W. Schmid, "Auger coefficients for highly doped and highly excited silicon," *Applied Physics Letters*, vol. 31, no. 5, pp. 346–348, 1977. DOI: 10.1063/1.89694 [Online]. Available: https://doi.org/10.1063/1.89694

[185] V. I. Klimov, A. A. Mikhailovsky, D. W. McBranch, C. A. Leatherdale, and M. G. Bawendi, "Quantization of multiparticle auger rates in semiconductor quantum dots," *Science*, vol. 287, no. 5455, pp. 1011–1013, 2000. DOI: 10.1126/science.287.5455.1011 [Online]. Available: https://doi.org/10.1126/science.287.5455.1011

[186] T. Herr, M. L. Gorodetsky, and T. J. Kippenberg, "Universal formation dynamics and deterministic high-yield states of kerr optical frequency combs," *Nature Photonics*, vol. 6, no. 7, pp. 480–487, 2012. DOI: 10.1038/nphoton.2012.127

[187] W. Bogaerts et al., "Silicon microring resonators," *Laser & photonics reviews*, vol. 6, no. 1, pp. 47–73, 2012.

[188] S. Coen, H. G. Randle, T. Sylvestre, and M. Erkintalo, "Modeling of octave-spanning Kerr frequency combs using a generalized mean-field Lugiato-Lefever model," *Optics Letters*, vol. 38, no. 1, pp. 37–39, 2013. DOI: 10.1364/OL.38.000037 [Online]. Available: https://opg.optica.org/ol/abstract.cfm?uri=ol-38-1-37

[189] T. Hansson, D. Modotto, and S. Wabnitz, "On the numerical simulation of kerr frequency combs using coupled mode equations," *Optics Communications*, vol. 312, pp. 134–136, 2014, ISSN: 0030-4018. DOI: https://doi.org/10.1016/j.optcom.2013.09.017 [Online]. Available: https://www.sciencedirect.com/science/article/pii/S0030401813008389

[190] I. Agha, Y. Okawachi, and A. L. Gaeta, "Theoretical and experimental study of parametric frequency conversion in silicon waveguides," *Optics Express*, vol. 17, no. 18, pp. 16 201–16 207, 2009. DOI: 10.1364/OE.17.016201

[191] Y. Ikku, M. Yokoyama, O. Ichikawa, M. Hata, M. Takenaka, and S. Takagi, "Low-driving-current InGaAsP photonic-wire optical switches using III-V CMOS photonics platform," *Optics Express*, vol. 20, no. 26, B357–B364, 2012. DOI: 10.1364/OE.20.00B357 [Online]. Available: https://opg.optica.org/oe/abstract.cfm?URI=oe-20-26-B357

[192] X. Li, Z. Wang, and H. Liu, "The coupled nonlinear schrödinger equation," *Journal of Applied Mathematics*, vol. 2014, p. 621 751, 2014, ISSN: 1110-757X. DOI: 10.1155/2014/621751

[193] H. Shu, L. Chang, X. Wang, and J. E. Bowers, "Sub-milliwatt-level kerr comb generation in high-q algaas-on-insulator microresonators," *Physical Review Applied*, vol. 14, no. 2, p. 024 073, 2020. DOI: 10.1103/PhysRevApplied.14.024073

[194] E. Mobini, K. Vyas, and K. Dolgaleva, "Nonlinear optical response and pulse propagation in iii-v semiconductor waveguides," *Optics*

Communications, vol. 508, p. 127 780, 2022. DOI: 10.1016/j.optcom.2021.127780

[195] J. Wang et al., "Low-loss optical waveguides fabricated by surface modification techniques," *Journal of Lightwave Technology*, vol. 34, no. 12, pp. 2900–2908, 2016.

[196] D. Liang and J. E. Bowers, "Low-temperature direct bonding techniques for iii-v-on-silicon photonic integration," *Journal of Vacuum Science & Technology A*, vol. 26, no. 6, pp. 1560–1568, 2008.

[197] T. Palacios, J. W. Chung, O. Saadat, and F. Mieville, "GaN and digital electronics: A way out of Moore's law?" *physica status solidi (c)*, vol. 6, no. 6, pp. 1361–1364, 2009. DOI: 10.1002/pssc.200881534

[198] L. Lin et al., "An adhesive bonding approach by hydrogen silsesquioxane for silicon carbide-based led applications," *Materials Science in Semiconductor Processing*, vol. 91, pp. 9–12, 2019.

[199] B. Olbrechts, G. Solge, and J.-P. Raskin, "Effect of etching parameters on surface roughness in semiconductor processing," *Journal of the Electrochemical Society*, vol. 153, no. 4, pp. C255–C260, 2006. DOI: 10.1149/1.2168408

[200] D. Liang and J. E. Bowers, "Recent progress in iii-v-on-silicon photonic integration," *Journal of Lightwave Technology*, vol. 28, no. 4, pp. 1523–1533, 2010. DOI: 10.1109/JLT.2009.2035824

[201] M. R. Amirzada et al., "Prediction and modeling of fabrication parameters in nanofabrication," *Microelectronic Engineering*, vol. 255, p. 111 700, 2022.

[202] N. Daldosso and L. Pavesi, "Nanosized silicon systems for photonics," *Laser & Photonics Reviews*, vol. 1, no. 1, pp. 48–56, 2007.

[203] R. Charavel and J.-P. Raskin, "Stress engineering in thin dielectric films for micro-machining," *Electrochemical and Solid-State Letters*, vol. 6, G120–G122, 2003.

[204] Y. Ikku, M. Yokoyama, O. Ichikawa, M. Hata, M. Takenaka, and S. Takagi, "High performance ingaasp optical waveguide devices on iii-v-on-insulator platform," *Optics Express*, vol. 20, no. 26, B357–B362, 2012.

[205] P. Laukkanen et al., "Surface passivation mechanisms in iii-v semiconductor interfaces," *Applied Surface Science*, vol. 540, p. 148 300, 2021.

[206] Z. Lin et al., "Geometry optimization for integrated optical waveguides," *IEEE Photonics Journal*, vol. 8, no. 3, pp. 1–9, 2016.

[207] M. Wright et al., "Thermal stability of thin dielectric films for optical coatings," *Thin Solid Films*, vol. 615, pp. 112–118, 2016.

[208] E. A. Patterson et al., "Low temperature oxide deposition processes," *Journal of Electronic Materials*, vol. 21, pp. 1005–1010, 1992.

[209] M. Broas, P. Sippola, H. Jiang, H. Lipsanen, and M. Paulasto-Kröckel, "Atomic layer deposited al2o3 films for surface passivation and wafer bonding," *Journal of Vacuum Science & Technology A*, vol. 35, no. 1, 01B105, 2017.

[210] J. Song et al., "Cmos mobility enhancement using advanced dielectric interfaces," *IEEE Transactions on Electron Devices*, vol. 58, no. 7, pp. 2100–2107, 2011.

[211] A. A. Tsyganenko and P. P. Mardilovich, "Infrared spectra of surface hydroxyl groups on alumina modifications," *Journal of the Chemical Society, Faraday Transactions*, vol. 92, no. 23, pp. 4843–4852, 1996.

[212] M. Digne, P. Sautet, P. Raybaud, P. Euzen, and H. Toulhoat, "Use of dft to achieve a synchronized description of gamma-alumina surfaces and hydroxyl coverage," *Journal of Catalysis*, vol. 211, no. 1, pp. 1–5, 2002.

[213] H. K. Sahoo, L. Ottaviano, Y. Zheng, O. Hansen, and K. Yvind, "Low temperature bonding of heterogeneous materials using al2o3 as an intermediate layer," *Journal of Vacuum Science & Technology B*, vol. 36, no. 2, p. 020 601, 2018. DOI: 10.1116/1.5005591

[214] K. Takakura et al., "Al2o3-assisted direct wafer bonding for heterogeneous integration," *Applied Surface Science*, vol. 610, p. 155 410, 2023.

[215] T. Suga, Y. Takahashi, H. Takagi, and B. Gibbosch, "Structure of al2o3/al2o3 interfaces bonded at room temperature by surface activation," *Acta Metallurgica et Materialia*, vol. 40, S133–S137, 1992.

[216] P. Asadollahi et al., "Characterization of bonding surface and electrical insulation properties of inter layer dielectrics for 3d monolithic integration," *ECS Transactions*, vol. 64, no. 5, pp. 121–128, 2014.

[217] H. K. Sahoo, L. Ottaviano, Y. Zheng, O. Hansen, and K. Yvind, "Low temperature bonding of heterogeneous materials using al2o3 as an

intermediate layer," *Journal of Vacuum Science & Technology B*, vol. 36, no. 2, p. 020 601, 2018. DOI: 10.1116/1.5005591

[218] R. Takakura, S. Murakami, K. Watanabe, and R. Takigawa, "Room-temperature bonding of al2o3 thin films deposited using atomic layer deposition," *Scientific reports*, vol. 13, no. 1, p. 3581, 2023.

[219] T. Nakasu et al., "High-k mos optical modulators using al2o3/hfo2 bonding," *SSDM Extended Abstracts*, PS–7–22, 2015.

[220] A. B. Smith, "Glasslike thin film properties for optical coatings," *Applied Optics*, vol. 45, pp. 1200–1208, 2006.

[221] C. D. Johnson, "Amorphous glass dielectric interfaces for photonic integration," *Thin Solid Films*, vol. 518, pp. 3000–3005, 2010.

[222] S. Chung et al., "Wafer bonding and layer transfer for integrated photonics," *Journal of Lightwave Technology*, vol. 28, no. 4, pp. 450–458, 2010.

[223] S. S. Chung et al., "Seamless on-wafer integration of si(100) mosfets and gan hemts," *IEEE Electron Device Letters*, vol. 30, no. 10, pp. 1015–1017, 2009. DOI: 10.1109/LED.2009.2027914

[224] O. R. Opaluch, S. Westrich, N. Oshnik, and E. Neu-Ruffing, "Medusa 84 sih – a novel high selectivity electron beam resist for diamond quantum technologies," *MRS Communications*, 2025, In press / Preprint.

[225] L. Chang et al., "Ultra-efficient frequency comb generation in AlGaAs-on-insulator microresonators," *Nature Communications*, vol. 11, no. 1, p. 1331, 2020.

[226] L. Ottaviano, M. Pu, E. Semenova, and K. Yvind, "Low-loss high-index-contrast AlGaAs-on-insulator waveguides for nonlinear photonics," *Optics Letters*, vol. 41, no. 17, pp. 3996–3999, 2016.

[227] T. Paulauskas et al., "Epitaxial lift-off method for gaas solar cells with high al content algaas window layer," *Semiconductor Science and Technology*, vol. 38, no. 3, p. 035 009, 2023.

[228] J. Villa, I Ramiro, J. M. Ripalda, E. Antolín, I. García, and A Marti, "A substrate removal processing method for iii–v solar cells compatible with low-temperature characterization," *Materials Science in Semiconductor Processing*, vol. 63, pp. 58–63, 2017.

[229] J. W. Lee, S. J. Pearton, C. R. Abernathy, W. S. Hobson, F. Ren, and C. S. Wu, "Wet chemical etching of $Al_{0.5}In_{0.5}P$," *Journal of The Electrochemical Society*, vol. 142, no. 6, pp. L100–L102, 1995. DOI: 10.1149/1.2044249

[230] J. Arokiaraj, S. Vicknesh, and A. Ramam, "Integration of indium phosphide thin film structures on silicon substrates by direct wafer bonding," *Journal of Physics: Conference Series*, vol. 34, pp. 404–409, 2006. DOI: 10.1088/1742-6596/34/1/066

[231] G. C. DeSalvo, W. F. Tseng, and J. Comas, "Etch rates and selectivities of citric acid/hydrogen peroxide on gaas, al0. 3ga0. 7as, in0. 2ga0. 8as, in0. 53ga0. 47as, in0. 52al0. 48as, and inp," *Journal of The Electrochemical Society*, vol. 139, no. 3, pp. 831–835, 1992.

[232] A. Thulaseedharan, L. F. dos Santos, S. Aghili, M. R. Mohammadpour, O. W. Oner, and K. Dolgaleva, "Tuning proximity effect correction for plasmonic metasurfaces," *J. Opt. Soc. Am. B*, vol. 43, no. 3, A132–A136, 2026. DOI: 10.1364/JOSAB.581059 [Online]. Available: https://opg.optica.org/josab/abstract.cfm?URI=josab-43-3-A132

[233] GenISys GmbH, *Beamer: Electron beam lithography layout software*, https://genisys-gmbh.com/beamer.html, Taufkirchen, Germany, 2023.

[234] S. A. Schulz, L. O'Faolain, D. M. Beggs, T. P. White, and T. F. Krauss, "Quantifying the loss in photonic crystal waveguides due to backscattering," *Physical Review B*, vol. 91, no. 8, p. 085 404, 2015. DOI: 10.1103/PhysRevB.91.085404

[235] L. Ren, S. H. Lee, and J. C. Jacob, "Proximity effect correction for nanoscale electron beam lithography," *Journal of Vacuum Science & Technology B*, vol. 22, no. 6, pp. 3200–3205, 2004. DOI: 10.1116/1.1813450

[236] K. Yao, Z. Liu, and Y. Chen, "Fast proximity effect correction algorithm for high-density nanostructures," *Microelectronic Engineering*, vol. 268, p. 111 900, 2023. DOI: 10.1016/j.mee.2022.111900

[237] Y. Yu, X. Zhang, L. Liu, and Y. Wang, "L-shaped nanostructures for polarization-sensitive light manipulation," *Optics Express*, vol. 21, no. 14, pp. 16 700–16 708, 2013. DOI: 10.1364/OE.21.016700

[238] M. J. Rooks and M. McCord, "Electron beam lithography," *Handbook of microlithography, micromachining, and microfabrication*, vol. 1, no. 2.5, p. 139, 1997.

[239] COMSOL AB, *Comsol multiphysics reference manual, version 6.2*, https://www.comsol.com, Stockholm, Sweden, 2023.

[240] M. A. Haque and B. M. A. Rahman, "Coupling optimization and mode analysis in integrated photonic structures," *IEEE Photonics Journal*, vol. 15, no. 2, pp. 1–8, 2023. DOI: 10.1109/JPHOT.2023.3241000

[241] M. Haelterman, S. Trillo, and S. Wabnitz, "Additive-modulation-instability ring laser in the normal dispersion regime of a fiber," *Optics letters*, vol. 17, no. 10, pp. 745–747, 1992.

[242] L. A. Lugiato and R. Lefever, "Spatial dissipative structures in passive optical systems," *Physical review letters*, vol. 58, no. 21, p. 2209, 1987.

[243] Q. Lin, T. J. Johnson, R Perahia, C. Michael, and O. Painter, "A proposal for highly tunable optical parametric oscillation in silicon microresonators," *Optics Express*, vol. 16, no. 14, pp. 10 596–10 610, 2008.

[244] R. Hamerly, M. Namdari, L. Mirzoyan, D. Gray, C. Rogers, and K. Jamshidi, "Conditions for parametric and free-carrier oscillation in soi ring cavities with active carrier removal," in *2017 International Topical Meeting on Microwave Photonics (MWP)*, IEEE, 2017, pp. 1–4.